THE UNIVERSITY OF
WARWICK

Library Declaration and Deposit Agreement

1. **STUDENT DETAILS**

Please complete the following:
Full name: **CHING-HSIEN CHEN**
University ID number: **0752293**

2. **THESIS DEPOSIT**

2.1 I understand that under my registration at the University, I am required to deposit my thesis with the University in BOTH hard copy and in digital format. The digital version should normally be saved as a single pdf file.

2.2 The hard copy will be housed in the University Library. The digital version will be deposited in the University's Institutional Repository (WRAP). Unless otherwise indicated (see 2.3 below) this will be made openly accessible on the Internet and will be supplied to the British Library to be made available online via its Electronic Theses Online Service (EThOS) service.
[At present, theses submitted for a Master's degree by Research (MA, MSc, LLM, MS or MMedSci) are not being deposited in WRAP and not being made available via EthOS. This may change in future.]

2.3 In exceptional circumstances, the Chair of the Board of Graduate Studies may grant permission for an embargo to be placed on public access to the hard copy thesis for a limited period. It is also possible to apply separately for an embargo on the digital version. (Further information is available in the *Guide to Examinations for Higher Degrees by Research*.)

2.4 *If you are depositing a thesis for a Master's degree by Research, please complete section (a) below. For all other research degrees, please complete both sections (a) and (b) below:*

(a) Hard Copy

I hereby deposit a hard copy of my thesis in the University Library to be made publicly available to readers after an embargo period of **two years** as agreed by the Chair of the Board of Graduate Studies.

I agree that my thesis may be photocopied. **YES**

(b) Digital Copy

I hereby deposit a digital copy of my thesis to be held in WRAP and made available via EThOS.

My thesis cannot be made publicly available online. **YES**

3. **GRANTING OF NON-EXCLUSIVE RIGHTS**

Whether I deposit my Work personally or through an assistant or other agent, I agree to the following:

Rights granted to the University of Warwick and the British Library and the user of the thesis through this agreement are non-exclusive. I retain all rights in the thesis in its present version or future versions. I agree that the institutional repository

administrators and the British Library or their agents may, without changing content, digitise and migrate the thesis to any medium or format for the purpose of future preservation and accessibility.

4. DECLARATIONS

(a) I DECLARE THAT:

I am the author and owner of the copyright in the thesis and/or I have the authority of the authors and owners of the copyright in the thesis to make this agreement. Reproduction of any part of this thesis for teaching or in academic or other forms of publication is subject to the normal limitations on the use of copyrighted materials and to the proper and full acknowledgement of its source.

The digital version of the thesis I am supplying is the same version as the final, hard-bound copy submitted in completion of my degree, once any minor corrections have been completed.

I have exercised reasonable care to ensure that the thesis is original, and does not to the best of my knowledge break any UK law or other Intellectual Property Right, or contain any confidential material.
I understand that, through the medium of the Internet, files will be available to automated agents, and may be searched and copied by, for example, text mining and plagiarism detection software.

(b) IF I HAVE AGREED (in Section 2 above) TO MAKE MY THESIS PUBLICLY AVAILABLE DIGITALLY, I ALSO DECLARE THAT:

I grant the University of Warwick and the British Library a licence to make available on the Internet the thesis in digitised format through the Institutional Repository and through the British Library via the EThOS service.

If my thesis does include any substantial subsidiary material owned by third-party copyright holders, I have sought and obtained permission to include it in any version of my thesis available in digital format and that this permission encompasses the rights that I have granted to the University of Warwick and to the British Library.

5. LEGAL INFRINGEMENTS

I understand that neither the University of Warwick nor the British Library have any obligation to take legal action on behalf of myself, or other rights holders, in the event of infringement of intellectual property rights, breach of contract or of any other right, in the thesis.

Please sign this agreement and return it to the Graduate School Office when you submit your thesis.

Student's signature: .....……

Date: .....

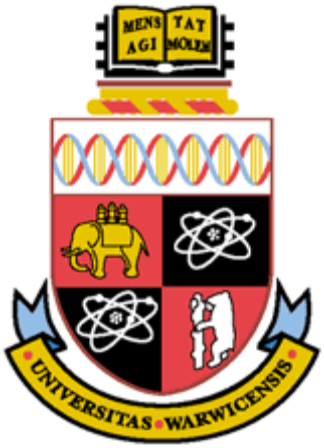

Tools for Developing Continuous-flow Micro-mixer

Numerical Simulation of Transitional Flow in Micro Geometries and a Quantitative Technique for Extracting Dynamic Information from Micro-bubble Images

by

Ching-Hsien Chen

A Thesis Submitted to the University of Warwick for the Degree of Doctor of Philosophy

University of Warwick, School of Engineering

July 2013

Contents

List of Figures

Acknowledgements

I cannot find words to express my gratitude to the following people. Without them this work would not have been possible. First and foremost, I would like to thank my supervisor, Prof. Shengcai Li, for the enduring guidance and persistent help throughout my entire PhD period. It is an honour for me to learn from him being as a researcher. With his support and encouragement, I have gained tremendous amount of knowledge and inspiration during this period. I would like to thank Mr. R. H. Edwards for his technical support. My special thanks goes to the financial support from EPSRC WIMRC PhD studentship and EPSRC engineering instrument loan pool and the manager, Mr. Adrian Walker, for their assistance on the instruments loan.

I owe my deepest gratitude to my parents, Sian-Wu Chen and Jhih-Yu Jhang, my parents-in-law, Cheng-Wen Hsu and Chin-Yen Ko, and especially my wife, I-Ying Hsu, for their unlimited love, care, and support throughout the years. With their encouragement and unwavering understanding, I could possibly make all this happen.

Declarations

I hereby declare that this thesis is my own work and effort and that no part of the work in this thesis was previously submitted for a degree at the University of Warwick or any other universities. All the sources of information used have been fully referenced and acknowledged.

Name :

Signature :

Date :

Abstract

Recent advance in the microfluidics including its fabrication technologies has led to many novel applications in micro-scale flows. Among them is the continuous-flow micromixer that utilizes the advantages associated with turbulent flows for rapid mixing, achieving the detection of fast kinetic reaction as short as tens of microseconds. However, for developing a high performance continuous-flow micromixer there are certain fundamental issues need to be solved. One of them is an universal simulation approach capable of calculating the flow field across entire passage for entire regime from very low Reynolds number laminar flow through transition to fully turbulent flow. Though the direct numerical simulation is potentially possible solution but its extremely high computing time stops itself from practical applications. The second major issue is the inevitable occurrence of cavitation bubbles in this rapid flow apparatus. This phenomenon has opposite effects: (a) deteriorating performance and damaging the micromixer; (b) playing a catalyst role in enhancing mixing. A fully understanding of these micro bubbles will provide a sound theoretical base for guiding the

design of micromixer in order to explore the advantage to maximum while minimizing its disadvantages. Therefore, the objectives of this PhD programme is to study the tools that will effectively advance our fundamental understandings on these key issues while in short term fulfil the requires from the joint experimental PhD programme held in the life science faculty for designing a prototype experimental device. During this PhD study, an existing numerical approach suitable for predicting the possibly entire flow regime including the turbulence transition is proposed for simulating the microscale flows in the microchannel and micromixer. The simulation results are validated against the transitional micro-channel experiments and this numerical method is then further applied for the micromixer simulation. This provides the researcher a realistic and feasible CFD tool to establish guidelines for designing high-efficiency and cost-effective micromixers by utilizing various possible measures which may cause very different flows simultaneously in micromixer. In order to study microscale cavitation bubbles and their effects on micromixers, an innovative experimental setup is purposely designed and constructed that can generate laser-induced micro-bubbles at desired position and size for testing. Experiments with

various micro-scale bubbles have been performed successfully by using an ultra high-speed camera up to 1 million frame rate per second. A novel technique for tracking the contours of micro-scale cavitation bubble dynamically has been developed by using active contour method. By using this technique, for the first time, various geometric and dynamic data of cavitation bubble have been obtained to quantitatively analyze the global behaviours of bubbles thoroughly. This powerful tool will greatly benefit the study of bubble dynamics and similar demands in other fields for fast and accurate image treatments as well.

Key words: microfluidics, micromixer, transition-turbulence model, laser-induced micro-scale cavitation bubble, high speed photography, active contour method.

Chapter 1

Introduction

1.1 Micromixer by Turbulent Mixing

In the fields such as life-science and chemistry etc., microfluidics is of significant importance, becoming a rapidly developing and interdisciplinary subject (Ho 2010). The miniaturization of fluidic system benefited from the technology of microelectromechanical system (MEMS) can reduce the size of laboratory setup by several orders of magnitude. The dramatic reduction in the amounts of samples and reagents is one of the main advantages of using microfluidics. Therefore, developing good micromixers of high performance to make good use of these advantages is fully justified by comparing the efficiency and the costs with the conventional mixers. A good micromixer can be judged by following three criteria: less time consumed for good mixing, less sample usage, and high throughput of resulting product. Rapid mixing is essential for achieving a spatially homogeneous mixing of samples.

Therefore, it is important to thoroughly investigate the core mechanism of turbulent mixing as well as the micromixer itself against various mixing strategies. Micromixers generally can be divided as two different categories: passive micromixer and active micromixer. The passive micromixer is preferred since the active micromixer requires the external field to maintain the mixing process. The requirement of external field also greatly increases the difficulty in the fabrication process of integrating the flow channel with the external field generator while still maintaining the same length scale of miniaturized system. The passive micromixer can be further divided into three sub-categories according to their mixing mechanisms: the laminar mixing using molecular diffusion, the chaotic mixing using chaotic advection, and the turbulent mixing using turbulent eddy diffusion. All these types of micromixers are required to increase mixing efficiency and to achieve homogenous mixing in a short time. The essential key to facilitate fast mixing is to increase the interfacial contact area between two fluids, e.g. by mixing the material across the whole cross section of fluids as much as possible (Sturman, Ottino et al. 2006). The design of laminar type of micromixers is mainly to maximize the combination of multiple flow channels either in

serial or parallel sequence for increasing the contact area between the fluids. The chaotic type of micromixers is mainly focused on the modification of the flow channel shapes to stretch and fold the fluids for obtaining the transverse advection across the cross section of channel as much as possible. A systematic review of laminar and chaotic micromixers is given in (Nguyen and Wu 2005) and (Hessel, Lowe et al. 2005). The studies of passive micromixers mainly focus on laminar mixing or chaotic mixing since turbulent mixing requires high flow velocity resulting in a high-pressure drop across the flow channel. This high pressure imposes difficulties on fabricating the micromixers in particular on the sealing of the flow channel. This is why turbulent mixing is often employed in conventional mixers but rarely seen in micromixers. However, turbulent mixing is very attractive because of its superior mixing efficiency in term of mixing quality and mixing time. G. I Taylor (Taylor 1921) showed that the coefficient of turbulent diffusion in the Lagrangian description is proportional to the mean square velocity of fluid particles and the time scale of turbulent eddy, which is significantly higher than that of the molecular diffusion where the diffusion coefficient relies only on the material property and temperature. Therefore,

micromixers utilizing turbulent mixing can generate much more throughput of product in much shorter time than those micromixers utilizing laminar mixing and chaotic mixing. The detail discussion on the Lagrangian correlation for turbulent diffusion can be found from the book by Bakunin (Bakunin 2008). As for the theory of molecular diffusivity readers are referred to the books by Bird et al. (Bird, Stewart et al. 2007) and by Cussler (Cussler 2009).

1.2 Continuous-flow Micromixer Used for Protein Folding

Rapid mixing of solutions is essential for elucidating chemical reactions and biological processes. For protein folding, the time scales of folding and unfolding spread in a wide range. Here, we only focus on the fast folding that the proteins fold within sub-millisecond. The method to observe the kinetics of protein folding can generally be divided as two broad categories, i.e. the transient and the equilibrium methods. The transient method requires a rapid change in the equilibrium between the native and denatured state of protein to perturb the system, and then follow the response of change by using optical

method as the change evolves towards a new equilibrium. The equilibrium method is to observe protein in the equilibrium without any physical or chemical perturbation to the system by using the techniques such as nuclear magnetic resonance (NMR) or electron paramagnetic resonance (EPR). For more detail of comparison and discussion on different methods please refer to the review (Myers and Oas 2002). In the transient method the sample mixing is one of the most popular and straightforward methods for the protein folding, which mixes two different fluid samples into one fluid solution along with the rapid change in the concentration of fluids. There are two different methods involved in sample mixing. One is the stopped-flow and the other is the continuous flow. For the stopped-flow method, the measurement of reaction commences after the flow is suddenly stopped (Britton 1940, Chance 1940, Gibson and Milnes 1964). This method is more economic and much easier to be integrated with variety of optical and spectroscopic instruments for monitoring the reaction. However, the intrinsic nature of stopped-flow method has hindered its mixing capability limited within the millisecond time resolution of protein folding. As for the continuous-flow method, the recording of the reaction is taken immediately after the mixing starts

(Hartridge and Roughton 1923a). This method was firstly adapted in the experiment at 1923 with a capability to resolve the millisecond time scale (Hartridge and Roughton 1923b) and then replaced by the stopped-flow method which is capable of the same time resolution. In the last 20 years, the continuous-flow method regains its importance because of the advance achieved in detection instruments and fabrications of mixers. The continuous-flow method can achieve the time resolution of protein folding down to microsecond time scale, extending the limit of stopped flow. Regenfuss et al. (Regenfuss, Clegg et al. 1985) developed a turbulent mixer by combining the idea of capillary mixer (Moskowitz and Bowman 1966) with the Berger-type ball mixer (Berger, Balko et al. 1968), achieving the dead time measured between 60 and 80 microseconds. Shastry et al. (Shastry, Luck et al. 1998) further improve the dead time down to 45 ± 5 microseconds by improving mixer fabrication, detection method and data analysis, which is 30 folds of time resolution compared with the commercial stopped-flow instrument then. The idea of using a ball right before the mixing channel to generate turbulent flow is a great success for reducing the mixing dead time down to the sub-millisecond time scale, below 100 microseconds.

However, the complexity of geometric construction introduces difficulties and problems, such as more time-consumption in the fabrication and frequent blocking of the channels, etc. Therefore, researchers are now seeking for simple geometry with efficient mixing approaches for this type of micromixers. Tackahashi et al. (Takahashi, Yeh et al. 1997) have developed a T-junction mixer for the turbulent mixing that achieves the dead time of 100 ± 50 microseconds. Bokenkamp et al. (Bokenkamp, Desai et al. 1998) by connecting two T junction mixers together achieve a mixing as short as 110 microseconds. Bilsel et al. (Bilsel, Kayatekin et al. 2005) adapt an arrow-shape mixer similar to the T micromixer with the two inlet channels connected at the right angle achieving a mixing time within 25 to 50 microseconds subject to the input-flow rate. A T-junction micromixer developed by Majumdar et al. (Majumdar, Sutin et al. 2005) has a similar performance as those by Bilsel et al. but it can operate sustainably at very high inflow velocity of approximately 79 m/s. By inserting a stainless steel wire throughout the cross-section area of inlet channel into the T mixer Masca et al. (Masca, Rodriguez-Mendieta et al. 2006) can reduce the mixing volume of fluids and increase the flow velocity in the inlet channels,

achieving a mixing time as short as 20 microseconds.

Since the pioneering work by Regenfuss et al., micromixers as mentioned above have been designed by adapting turbulent flow for acquiring a rapid mixing. Their strategy is to create the required turbulent flow as early as possible once the two fluids meet and pass along the outlet channel. A new strategy adapted by Matsumoto et al. (Matsumoto, Yane et al. 2007) is to create the turbulent flow which is generated through passing a narrow gap before the collision of two fluids. His design thus reduces the dimension of inlet channel. This mixing strategy facilitates the micromixer to achieve the mixing time of 11 microseconds compared with the tens of microseconds achieved by mixers using the aforementioned strategy. The advance in design and fabrication of micromixers makes the observation of rapid mixing in the tens of microseconds possible that is comparable to the phenomena to be observed with significantly reduced expensive samples compared with conventional mixers. Though, the novel design of laminar micromixer (Hertzog, Michalet et al. 2004) can achieve a mixing time of 8 microseconds with a highly economic samples consumption of nanoliter per second scale.

Its design strategy has some disadvantages. Their design is to diminish the cross-section of fluid channels in order to obtain much thinner fluids in the mixing chamber, i.e. much smaller mixing volume that achieves rapid mixing through molecular diffusion. However, this makes the fabrication of micromixers extremely difficult owing to the high tech required for silicon micro-fabrication and the trouble free operation impossible owing to the tiny size of channel dimension (around a few micrometers) presenting a real risk of clogging in the mixing chamber. Therefore, a most advanced design of micromixer for rapid mixing requires the satisfactions on (1) easy fabricating, unclogging, and reassembling; (2) minimizing consumption of samples; and (3) rapidly mixing within microseconds (Bilsel, Kayatekin et al. 2005, Majumdar, Sutin et al. 2005, Masca, Rodriguez-Mendieta et al. 2006).

1.3 Computational Fluid Dynamics in Microfluidics

The rapid growing of digital computer hardware in the recent decades has created a new developing subject called Computational Fluid Dynamics, CFD. This subject was, in the past, only studied by a few researchers who

have the access to those high-performance computing facilities. Nowadays it has been a popular approach throughout the engineering applications, especially for aerospace and automotive engineering. Computational fluid dynamics has become a new third approach to offer a cost-effective alternative solution for the research in fluid dynamics (Anderson 1995). It complimented the other two approaches of experimental fluid dynamics and theoretical fluid dynamics to form a harmonic balance of tripod, each approach is equally important and irreplaceable to others, as shown in the Fig. 1.1.

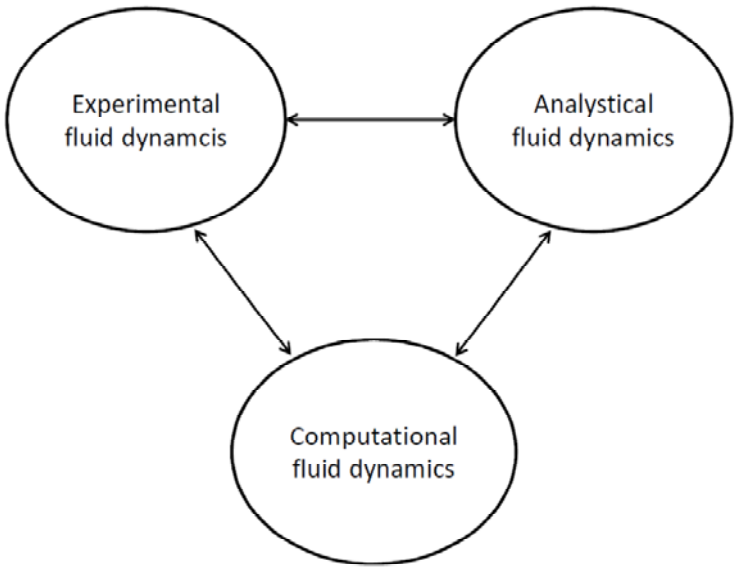

Fig. 1.1 The three aspect of fluid dynamics adopted from (Anderson 1995)

Computational fluid dynamics is an interdisciplinary subject that involves the integration of mathematics, fluid dynamics, and computer science. The use of CFD requires a basic understanding of these three aspects. Without such understanding, novice users might potentially have wrong interpretations and judgements on their numerical results, even the result seems good in the graphics. Recent years with the high demand of acquiring CFD results in a very short time frame from industries and academia the commercial CFD software has been gradually gaining a wide acceptance since the writing and testing of CFD code have been thoroughly verified by developers from the respective companies such ANSYS and STAR-CCM (Tu, Yeoh et al. 2008). These commercially available softwares not only offer a wide range of physical models and numerical modelling but also have the capacity to be customised as user-defined physical and numerical models for the application of academic researches. It relieves users of the burden of spending a huge amount of time in the development and verification of in-house CFD code instead of fully dedicating on the applications they are interested. Although these commercial CFD codes are usually treated as black boxes in the simulation, a fully understanding of the physical representation of these black

boxes that are based on the fundamental govern equations of CFD is essential for applying them correctly and successfully. The fundamental governing equations in CFD, which are the mathematical equations describing the physical characteristics of flow behaviours, are based on the conservation laws of physics and the hypothesis of continuum. The conservation laws of physics are as followed: the conservation of mass, momentum, and energy. The momentum and energy conservation are directly derived from Newton's second law and first law of thermodynamics, respectively. By applying these physical principles to an infinitesimal fluid volume together with the use of the physics law stated by Isaac Newton, which the viscous stresses are proportional to the rate of strain, the well-known Navier-Stokes equations can be obtained, which is a coupled system of nonlinear partial differential equations for solving the velocity fields of fluid. There is still no general analytical solution to these equations up to date, though some simple idealized flows can be solved analytically. It is one of the main reasons that the computational fluid dynamics becomes such an important subject for obtaining the solution of complex fluid behaviour. All the physics of flow modelling in the CFD start from this milestone. For details of the numerical

schemes in CFD, readers are referred to the books (Anderson 1995, Versteeg and Malalasekera 2007, Chung 2010). Generally, when we discuss flow behaviours based on Navier-Stokes equation, the macroscopic scales of flow properties such as velocity, pressure, density, and temperature and so on are meant. Although in numerical simulations of microchannels and micromixers the prefix word, 'micro' seems to challenge the validation of hypothesis of continuum, the size scale of these micro-devices in the application of microfluidics is still large enough to comply with the continuum of fluids. The length scale of averaged intermolecular distances and mean free path between the constituent molecules for gas and liquid are generally around a few micrometers and submicrometers, respectively. While for microfluidic devices the length scale is typically in the order of 10 micrometers or even more. Therefore, the fluid volume is large enough for containing a sufficiently large amount of molecules for obtaining steady and reproducible measurements of flow properties (Bruus 2008). In Fig. 1.2 the effect of size of fluid volume on the flow properties measured by an instrument is illustrated by Batchelor (Batchelor 2000). Consequently, we can apply the Navier-Stokes equations comfortably as the fundamental governing equations,

which are based on the hypothesis of continuum, to the numerical simulation of microfluidic devices. In contrast, for the nanofluidics where the hypothesis of continuum is no longer valid, the molecular dynamics and quantum mechanics are required for numerical simulations.

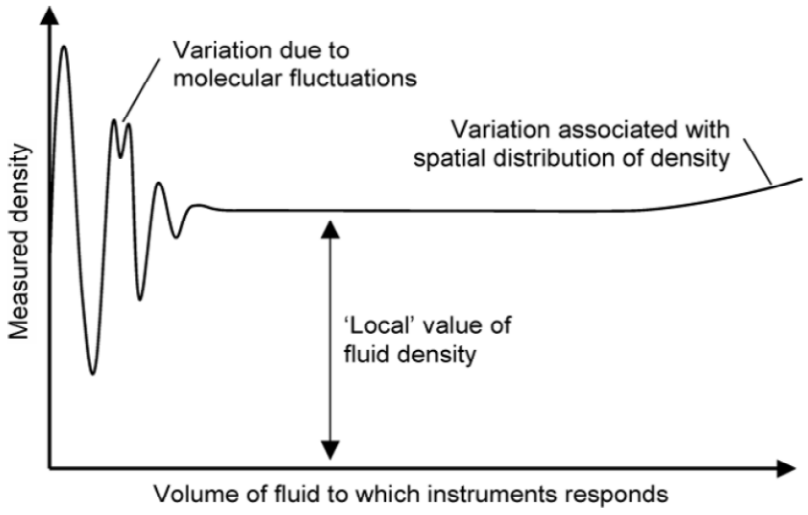

Fig. 1.2 Effect of fluid volume on the density measured by an instrument (Batchelor 2000)

Through the analysis of dynamic similarities (Kundu and Cohen 2008), by using the non-dimensional scaling in the Navier-stokes equations, the flow behaviours can be characteristized by Reynolds number, which is the ratio of inertia force to viscous force. As the Reynolds number exceeds 2300, the internal channel flow undergoes the transition from laminar flow to turbulent flow. The flow field generally can be categorized into three different regimes

based on the Reynolds number: laminar, transitional turbulent, and fully turbulent regimes. In computational fluid dynamics, the flow field can be resolved by discretizing the Navier-Stokes equations into a set of discrete algebraic equations according to the various numerical schemes such as finite difference method, finite volume method, and spectral method. This numerical method is the so-called Direct Numerical Simulation (DNS), which can be applied for all the regimes. Especially for turbulent flows, DNS can provide not only full details of instantaneous turbulent flow variables and turbulence statistics for assessing turbulent structures and transports that cannot be easily obtained in the laboratory but also a research tool in turbulent modelling (Moin and Mahesh 1998). All scales of the turbulent flow are resolved by DNS down to Kolmogorov scale without any turbulent modelling. Nevertheless, due to the intrinsic nature of turbulent flow in the extreme wide range of length and time scales of turbulent eddies, the computational cost for resolving the turbulent flow entirely by DNS is prohibitively high, which can roughly be estimated by using the Kolmogorov theory (Pope 2000). Therefore, turbulent models are required and developed as alternatives for the simulation of turbulent flows, especially those for

industrial applications. Often the time-averaged properties of flow variables are sufficient for most engineering problems. Therefore, the majority of researches on turbulent modelling focus on the Reynolds-averaged Navier-Stokes (RANS) equations derived from the concept of Reynolds decomposition, which separates the turbulent flow properties into its mean and time-varying fluctuating components. Applying the time-averaging operation to the Navier-Stokes equations yield six additional unknowns in RANS equations, the Reynolds stresses. This leads to the turbulent closure problems where the additional equations in predicting the turbulent Reynolds stresses are modelled to close the RANS equations. Generally, the classification of RANS turbulent models can be based on the additional equations that need to be solved. For the detail of various RANS turbulent models the reader is referred to the books (Pope 2000, Durbin and Reif 2001, Versteeg and Malalasekera 2007). Though the success of RANS turbulent models in resolving the mean values of turbulent flow variables, all the detail of instantaneous fluctuations of turbulent flow are lost due to the modelling of turbulent Reynolds stresses. As a result, the RANS turbulent models lack the generality as a general-purpose model and rely on the parametric

calibrations to fit the specific flow problems. One approach for overcoming this deficiency of RANS turbulent model is to use Large Eddy Simulation (LES). The idea of LES is based on the small turbulent eddies are more isotropic and universal, which is easier to be modelled, whereas the large turbulent eddies are anisotropic and specific for the geometric domain of turbulent flow, which is more difficult to be modelled. Instead of applying the temporal filter to obtain RANS equations, one applies a spatial filter to cut off the small eddy to yield LES momentum equations where the large eddy is directly resolved. The size of resolved eddies depends on the cut-off width of the spatial filter which is often taken as the same order of mesh size in the numerical simulation. The small eddy, i.e. sub-grid-scale eddies, is then modelled by a sub-grid-scale stresses model (SGS model). In this approach, one can use coarser meshes in the large eddy simulation to reduce the computational cost. As to the numerical techniques for DNS and LES, details can be found in the book (Jiang and Lai 2009). The demand for the computational resource in using various turbulent modellings and the corresponding resolved physics can be classified and illustrated as Fig. 1.3. The properties of turbulent flow are fully modelled in RANS turbulent

models while it is partially modelled in large eddy simulation depending on the grid sizes used in the simulation. If the grid size is refined smaller enough, the solution of large eddy simulation becomes similar to the solution of direct numerical simulation.

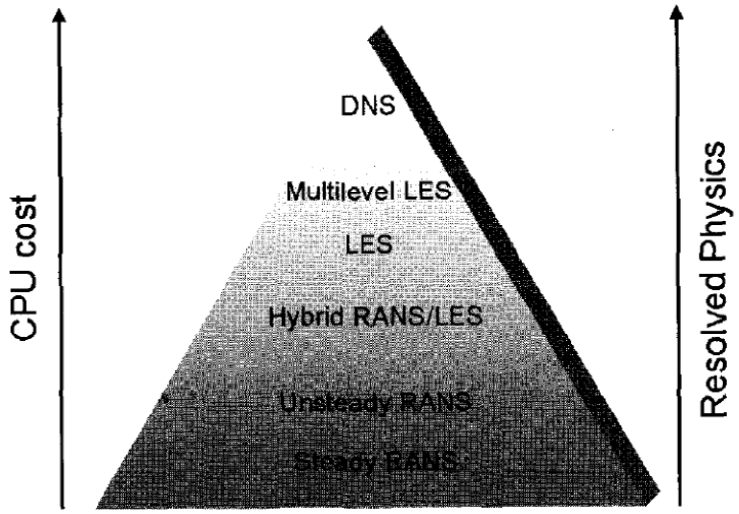

Fig. 1.3 the classification of turbulence modellings on the computation cost and resolved physics (Sagaut, Deck et al. 2006)

For rapid mixing in micromixers, it is required to make the flow operate in the regime of turbulent flow, often in the transitional turbulent regime. Therefore, in order to achieve the optimized mixing in micromixer, it is essential to investigate the numerical approaches suitable for simulating transitional turbulent and fully turbulent flows simultaneously in the micromixer systems as a tool for providing design guidelines. To simplify the

problem at hand, one often uses microtubes or microchannels as the first step for investigating the turbulent flows in microscale. In microchannel experiments, one fundamental question has attracted intensive researches in recent years: Whether the turbulent flow in the microchannel has the same characteristics as it has in the conventional channel. With the newly developed microscopic Particle Image Velocimetry (micro-PIV) technique the statistical and structural similarities of turbulence between microscale and macroscale channels are showed by Natrajan et al. and Li and Olsen. (Li and Olsen 2006, Natrajan, Yamaguchi et al. 2007). One of main reasons of early transition is attributed to the relatively high surface roughness in the microchannel (Natrajan and Christensen 2010). As the result, those turbulent models developed for the macroscale flow could be directly[1] applied to the turbulent simulation in the microscale flow. However, to the best of this author's knowledge, it is very rare[2] to find the CFD researches of turbulent flow modelling in microchannel, even if not to mention the micromixer. The current majority of CFD researches are focusing on the regime of laminar

[1] They might need some calibration

[2] None in the author's search from currently published world literatures until the date of writing this thesis (i.e. July 2012)

flow for the design of laminar and chaotic micromixer. Whereas the recent development of continuous flow micromixer and the collaboration with Bioscience Department at the University of Warwick, it is essential to search for and verify a reliable CFD approach for the simulation from transition throughout to fully turbulence in microscale wall-bounded flow. As a result, this PhD programme is thus initiated through the collaboration on the WIMRC joint project: Development of a Microsecond Mixing Instrument for the Detection of Folding Intermediates. The goal of this WIMRC joint project is to develop a highly efficient continuous-flow mixing devices capable of initiating and detecting reactions an order of magnitude faster than those of currently commercial stopped-flow device supplied by the industrial partner, TgK Scientific. Throughout the design, implementation, and evaluation of this continuous-flow micromixer, this joint project has brought together the micro-fabrication technologies, CFD simulation and analysis, the rapid CCD technologies and biological reactions knowledge. Herein, one of the main objectives of this PhD study is to investigate a CFD approach for evaluating the efficiency and guiding the design of continuous-flow mixer.

1.4 Experiment of Laser-Induced Microscale Cavitation Bubbles

Just like the natural enemy of all the hydro-machinery, the cavitation is also unavoidably encountered in this type of rapid flow apparatuses. With the increase of fluid velocity and the pressure drop inside the mixing chamber, the hydro-dynamically induced bubble formation has been observed across the mixing channel during our test run by using the proposed continuous flow micro-mixer. This cavitation bubble cloud could potentially obscure the transmission of fluorescent light emitted from the fast kinetic reaction and thus deteriorate the photoelectric measurement, which had previously been observed in the conventional mixer and considered as a transient turbidity in the flow stream reported by Chance (Chance 1940). Here, the effect of cavitation bubble toward the apparatuses is treated as a unwanted artefact and has been evaluated in the stopped flow experiments (Wong and Schelly 1973). In addition, the cavitation bubble formation could also cause erosion in the mixing channel that might further deteriorate the mixing efficiency, leading to substantial damage on the micromixer itself. As suggested by Chance (Chance 1964), there are numerous ways to avoid or minimize the occurrence

of cavitation bubble. However, some strategies may mitigate cavitation bubble formation but also sacrifice the mixing efficiency of mixer. To resolve this dilemma compromises often have to be made in the design of mixer. Recent advance in the micro-fabrication as aforementioned has provided the possibility of designing continuous-flow micromixers that can sustain enormous pressure, often over 100 bars. For such type of mixers accompanying high flow velocity and pressure drop, cavitation bubbles could be much more easily triggered in the micromixer and their erosion effect could be enormous under such an adverse environment. Recently, the presence of hydrodynamic cavitation such as travelling bubble and super-cavity flow has all been identified in the micro-Venturis (Mishra and Peles 2006). The inception of cavitation bubble is observed downstream across the microchannel at various locations including in the throat of micro-Venturis, inside the bulk fluid of diffuser, and at the boundaries of micro-device. As for the studies of cavitation erosion in the microchannel, initial attempts on investigating the hydro-dynamically induced cavitation on microscale have been made either through the numerical simulation (Skoda, Iben et al. 2011) or through the experimental observation with a newly

developed flow measurement technique (Iben, Morozov et al. 2011). However, there are still many unknown effects of such micro-scale cavitation bubble, some of which are fundamental in the microfluidics. Without a full understanding of these microscale cavitation bubbles and their effects, developing next generation of such high performance mixers is impossible. To facilitate the design of continuous-flow micromixer, new approaches for investigating the dynamics of these micro bubbles have been proposed by this PhD programme.

Since 1970s, the laser-induced cavitation bubble has provided a precisely controllable way to generate a desirable size of cavitation bubble at a demanding location and become an essential tool for studying the behaviour of cavitation bubble qualitatively. In last a few years along with the development of microfluidics, great attention has also been paid to the possible micro-scale cavitation bubbles and their dynamics. Novel techniques that utilize laser-induced cavitation bubble in the microfluidic devices has been developed and introduced to research including this PhD programme, as presented in the chapter 4. Therefore, for the continuous-flow micromixer to

be developed by this joint project, it is essential and worthwhile for this PhD programme to initiate such an investigation on this type of micro-scale cavitation bubbles. According to the delegated task from this joint project, during my PhD programme, an experimental setup for investigating laser-induced cavitation bubble in the microscale is purposely designed and constructed. This facility can perform all the experiments planned for studying micro-scale cavitation bubbles. This versatile facility is now also being used for another PhD programme on the dynamics of micro-bubble in bio-environment. It can thus serve well as a platform for studying the dynamics of micro-scale cavitation bubble in various circumstances including erosion effects etc. in microfluidics. In order to tackle the difficult task of quantitatively analysing bubble images obtained from the ultra-high speed photography, an image segmentation method has been developed from this PhD programme such that more detail and accurate information can be extracted to advance our knowledge about the dynamics of these micro-bubbles.

1.5 Outline of Present Work

Based on the delegated tasks from the joint WIMRC project, as depicted above, my PhD thesis is structured as follows. In chapter two, a RANS turbulent transition model, 'local correlation transitional model (LCTM),' originally developed for simulating the external flow encountered in aerodynamics by Menter et al. (Menter, Langtry et al. 2006a) is successfully implemented and validated for the numerical simulation in the microchannel flow. This transition model provides a framework for constructing a numerical approach on simulating various flow behaviours through the adjustment of empirical constants. The numerical results are compared with the experimental results of microchannel flow obtained from micro-particle image velocimetry as well as the moody chart. Apart from the capability of predicting turbulent transition, this transition model can also account for the flow field in the laminar and fully turbulent regime as a general-purpose RANS turbulent model. This provides a CFD tool for evaluating the mixing efficiency and guidelines for designing the continuous-flow micromixer of the joint WIMRC project, owing to its superior ability in predicting flow velocity and pressure properly across the entire three flow regimes. In chapter

three, based on the validation above, we further apply this numerical method to micromixer simulations for analysing the mixing efficiency and the required time to complete mixing, which are essential for micromixers used for bio-medical and chemical experiments. The convection-diffusion equation for accounting the mass transfer is integrated with the LCTM to serve this purpose. This provides a viable CFD approach for the design of the most advanced continuous flow micromixer that serves the final objective of the whole WIMRC project. In chapter four, we conduct experiments of laser induced micro-scale cavitation bubbles for studying the behaviours of cavitation in the microscale and its interaction with the wall-boundaries made of materials often used in the fabrication of micromixer. By utilizing ultra high-speed photography and shadowgraph technique, the motions of microscale cavitation bubbles can be recorded in various environments such as the spherical cavitation bubbles in free space and the non-spherical ones either close to rigid-wall boundaries or to soft-wall boundaries. Then, these bubble images are further processed by a highly automatic and self-adjusting image segmentation program partially developed from this PhD study for bubble contour delineation. The complete geometric data of bubble contours

can be extracted for quantitatively characterizing the dynamic behaviour of bubbles. Detail of this approach is introduced in chapter five with demonstration examples. By using this new approach, the information gained from experiments will greatly enhance our understanding of these micro-bubbles. Currently, this experimental setup enables us to study the behaviour of microscale cavitation inside microchannel and micromixer that is a phenomenon already observed during the experiments of continuous flow micromixers but we have little knowledge yet. In the chapter six, we conclude the present work and discuss on the follow-up work in the near future.

Chapter 2

Searching For Numerical Approach Suitable for Microchannel Flows

2.1 Introduction

The rapid development of microfluidics has intrigued the desire for a fuller understanding of the flow behaviour in micro scale. With the aid of microelectro-mechanic system (MEMS) researchers are now able to fabricate very complex geometry of microfluidic devices used in various interdisciplinary areas. Yet there are still many challenges remaining on fundamental fluid dynamics where the foundation of microfluidics lies. Among them, the behaviour of turbulent flow and turbulence transition in the micro scale is fundamentally of most important. Nowadays, the experimental methods are often the only approach for studying the flow behaviours, especially for turbulence transition. The flow characteristics in the microchannel are of significant importance for the design of microfluidic

devices and are essential for further advancing microfluidic devices. Currently, the turbulent and transitional flows in the microchannel are a hot area of research owing to the discrepancies of experimental data between the conventional macroscale and microscale channels, which might be contributed to the unknown microscale effects involved. For example, some researchers have reported the deviations of friction factor observed in the microchannel indicating an earlier turbulence transition than it should be. Peng et al. (Peng, Peterson et al. 1994) observed an earlier turbulence transition occurring approximately at Reynolds numbers in the range of 200-700 and a fully turbulent flow at Reynolds numbers of 400-1500 in a rectangular microchannel[3]. Mala and Li (Mala and Li 1999) reported an earlier turbulent transition of water flowing through microtubes made of fused silica and stainless steel with size ranging from 50 to 245 um. The transitional and fully turbulent Reynolds numbers are, subject to materials used, ranging from 300-900 and fully developed turbulence of 1000-1500, respectively. In these reports, they concluded that the higher experimental

[3] This device has a hydraulic diameter of 133-367 micrometers and aspect ratio from 0.333 to 1, respectively

friction factors may be attributed to the early transition or the surface roughness. Similar result is also obtained in trapezoidal silicon microchannel through a follow up study by Qu et al. (Qu, Mala et al. 2000). These results seem to invalidate the applicability of friction factor theory based on the conventional macroscale channel to the microchannel; And the discrepancy found from these data are now interpreted as new effects of microchannel flow. However, on the contrary, some researchers reported good agreements consistent with the theory valid in conventional macroscale channel, indicating no evidence of earlier turbulence transition. For example, Judy et al. (Judy, Maynes et al. 2002) investigated the liquid flows of distilled water, methanol, and isopropanol in round and square microchannels made of the fused silica and stainless steel with the channel diameter ranging from 15 to 150 um. Their result showed no evidence of deviation from the laminar friction factors in macroscale up to the Reynolds number of 2000. Kohl et al. (Kohl, Abdel-Khalik et al. 2005) measured the internal pressure of microchannel flow using pressure sensors integrated to the microchannel of hydraulic diameter ranging from 25 to 100 um. Their results showed agreement with the laminar incompressible flow predictions, indicating no

evidence of earlier transition up to Reynolds number 2067. Rand et al. (Rands, Webb et al. 2006) reported the laminar-turbulent transition for water flow in round microtubes with the diameters ranging from 16.6-32.2 um. In their experiments, the turbulence transition occurs in Reynolds number of 2100-2500. Although the possible reasons for this deviation have been cited from previous works mentioned above, their conclusion is still remaining disputable. Hetsroni et al. (Hetsroni, Mosyak et al. 2005) reviewed the experimental data of laminar incompressible flows of gas and liquid in microchannels published in the literature and concluded that those experiments producing data that consistent with the conventional theory all have the actual experiment conditions identical with those conditions used in the theoretical model. It is also concluded that the determination of critical Reynolds number based on the analysis of pressure gradient dependency on the Reynolds number leads to the inconsistency in turbulence transition. For more detail on the relative discussion readers are referred to the book written by Yarin et al. (Yarin, Mosyak et al. 2009). Hetsroni et al. (Hetsroni, Mosyak et al. 2011) further reviewed wall roughness effect in the laminar duct flow by comparing the available experimental and numerical data with the

analytical estimation obtained from dimensional analysis and concluded no differences between conventional and microscale channels. Steinke and Kandikar (Steinke and Kandlikar 2006) reviewed over 150 papers from available literature that directly deal with the pressure drop measurement in microchannel. Based on approximately 40 papers that reported the detailed experimental data, they established a database with the total number of datum points over 5000 and concluded that the significant deviation from conventional theory are those papers not accounting for the entrance and exit losses or the frictional losses resulting from developing flow in the microchannel. With the correction of these component losses their experimental data show good agreements with the theory for the laminar flow. In addition to the above-mentioned reasons, the measurement accuracy that can contribute a large uncertainty in the experimental data (Judy, Maynes et al. 2002, Guo and Li 2003) is identified as another crucial factor causing the discrepancy.

Apart from the pressure measurement method which measures the pressure drop as a function of flow rate, the flow visualization is a direct method for

understanding the dynamics of fluid flow. Various methods for microscale flow visualization have been developed for microchannel experiments since the late 1990s. The microscale flow visualization generally can be classified into two methods: Scalar-based and particle-based flow visualization methods. The particle-based flow visualization methods is to observe the velocity of marker particles inferred with the motion of the bulk flow (Adrian 1991); the scale-based flow visualisation method is to observe the velocity of a conserved scale inferred with the motion of the bulk fluid (Sinton 2004). For more information on visualization methods of microscale flow please see the review by (Sinton 2004). The selection of suitable visualization-method depends on the application one interested. Of these methods micro particle image velocimetry (micro-PIV) is well developed and mature with the capability of acquiring high spatial and temporal resolutions of flow field. Another important capability of micro-PIV method is capable of measuring the vorticity and strain-rate fields. Comparing with micro-PIV, the main advantage of scalar-based method is the readiness of interpreting the velocity field obtained from the measurement, which is suitable for measuring the scalar transport such as the evaluation of mixing efficiency in the

micromixer.

Micro-PIV was firstly conducted by Santiago et al. (Santiago, Wereley et al. 1998) with the continuous-illumination mercury arc lamp. Follow up work (Meinhart, Wereley et al. 1999) impose Nd-Yag laser to illuminate sub-micron diameter fluorescent polystyrene particles, improving the spatial resolution and the limit of the measured bulk velocity. Since then, Micro-PIV is often used for directly observing the instantaneous fluid velocity and vorticity fields in the microchannel as an alternative measurement method. Owing to its non-invasive nature, micro-PIV has been widely adapted for the study of microscale flows, especially for the turbulent transition flow. By using this relative new experimental technique, turbulence transition in the microchannel has been studied by many researchers reporting that the onset of transition has no deviation from the traditional prediction in the macroscale channel. Sharp and Adrian (Sharp and Adrian 2004) performed a set of pressure drop and micro-PIV experiments on the turbulence transitional flow in microtubes sizing from 50 um to 247 um. They showed a consistency with the macroscopic Poiseuille flow on the laminar friction factor by using

over 1500 measurements of pressure drop versus the flow rate. In addition, in their micro-PIV result, they use the abrupt increasing fluctuation of centreline velocity to indicate the transitional flow showing that the transitional turbulence occurs at the same Reynolds number of 1800-2300 as the macroscale flow does. The first micro-PIV measurements of transition-turbulent and turbulent flow fields were reported by Li et al. and Li and Olsen (Li, Ewoldt et al. 2005, Li and Olsen 2006b). The data of ensemble-averaged streamwise velocity profiles, velocity fluctuations, and Reynolds shear stresses in rectangular microchannels with the hydraulic diameters varying from 200 um to 640 um were collected for the comparison with empirical formula of the macroscale flow. Based on a jump in the measured centreline velocity fluctuation, the transition to turbulence was observed at Reynolds numbers ranging from 1718 to 1885, showing good agreement with the experiment of Sharp and Adrian (Sharp and Adrian 2004). The fully turbulent flow was observed at Reynolds numbers ranging from 2600 to 2900 based on that both streamwise and transverse root mean square velocity fluctuations no longer increase with increasing Reynolds numbers as well as the normalised mean velocity profiles approach to the logarithmic

velocity profiles of macroscale fully turbulent channel flow. Micro-PIV measurement of transition to turbulence flow in microscale round tube were reported by Natrajan and Christensen (Natrajan and Christensen 2007) , and Hao et al. (Hao, Zhang et al. 2007). Hao et al. concluded that the transition occurred at Reynolds number from 1700 to 1900 and fully developed flow was achieved as the Reynolds number exceeding 2500 by studying the transition flow in a glass microtube with a diameter of 230 um; Natrajan and Christensen also observed the similar result that a transition became noticeable from Reynolds number at 1900 in a fused silica capillary with a diameter of 536 um. The fully turbulent flow was attained at Reynolds of 3400. Both concluded the good consistency with the results of macroscale flow. Furthermore, Natrajan and Christensen (Natrajan and Christensen 2010) studied, in detail, the correlation of momentum transport against wall roughness in the smooth and rough rectangular microchannels with a hydraulic diameter of 600 um by using micro-PIV. The early turbulence transition was observed in the rough micro-channel while the flow behaviours in the smooth microchannel have no evidence of early transition which is consistent with the macroscale flow. This same tendency of early

transition in the rough silicon rectangular microchannel was also observed by Hao et al. (Hao, Yao et al. 2006). Through micro-PIV the structural similarities between macroscale and microscale wall turbulences were observed in both rectangular (Li and Olsen 2006b) and round (Natrajan, Yamaguchi et al. 2007) microchannels. The large turbulent eddies were observed directly in the instantaneous velocity fields showing the consistency with the large-scale turbulent structure often observed in the macroscale. In addition, the single-point velocity statistics including the mean velocity profile, the root-mean-square streamwise and wall-normal velocities, and the Reynolds stress profile can be computed from the instantaneous, statistically independent velocity fields acquired by micro-PIV, which also shows quite good statistical similarities with the results from direct numerical simulation. In conclusion, all the above results show that micro-PIV is a truly suitable tool for the investigation of microscale flow.

Except for micro-PIV, another non-invasive time-resolved measurement method is micro molecular tagging velocimetry (micro-MTV) which belongs to the category of scalar-based method. A water-soluble phosphorescent dye

is used instead of the seed particles. The first micro-MTV experiment was performed by Maynes and Webb (Maynes and Webb 2002) in a fused-silica microtube with a diameter of 705 um. By comparing the mean velocity profiles of various Reynolds numbers ranging from 500 to 2390 with laminar flow velocity profile they concluded that the deviation from the laminar flow profile started as Reynolds number exceeds 2100 showing a good agreement with laminar flow theory. By using micro-MTV, Elsnab et al. (Elsnab, Maynes et al. 2010) further investigated the water flow in the high aspect ratio rectangular microchannel over Reynolds numbers ranging from 173 to 4800 through the laminar, transitional, and fully turbulent flow regimes. In addition, the inner scaling of transitional and turbulent velocity profiles was obtained by this experimental method for the first time in the microchannel. Comparing with the macroscale experimental and DNS data they concluded that the microscale flow is statistically similar to the macroscale flow based on the experimental trend of micro-PIV result including the mean velocity profiles and the inner normalized mean velocity as well as the derived Reynolds stress and production of kinetic energy. The main advantage of micro-MTV, in contrast to micro-PIV, is its capability to resolve the flow

field in the near-wall region well, which greatly extends the attractiveness of micro-MTV and opens a new way to study the mean dynamics of transitional channel flow (Elsnab, Klewicki et al. 2011).

In contrast to the rapid progress in the experimental techniques for the study of microscale flow, the corresponding CFD simulation was only limited to the application in the laminar flow simulation. Although turbulence flow simulation in CFD has been extensively studied and widely applied in the conventional macro scale across the various disciplines, it is surprisingly to find that this great success has not been widely extended to microfluidics. This situation might be attributed to the lack of detailed experimental data of flow fields for numerical validation. The deficiency in both the experimental methods and the high precision instruments for accurately measuring such a narrow flow field of microfluidics has greatly hindered the development of turbulent flow simulation in the microfluidics. Therefore, the research of microfluidics had been mainly focusing on the laminar and chaotic flows owing to the lack of application where the high shear flow is generally required in the microfluidics as well as to the great difficulty in achieving the

required turbulent flow at extremely high velocity while avoiding the leakage of microfluidics caused by the high pressure. The recent renaissance in the continuous flow micromixer has thus shown a desire for searching and developing a valid CFD approach for simulating turbulent flow including its transition in the microscale flow.

The velocity profiles obtained from micro-PIV or micro-MTV are usually compared to either the theoretical result of laminar flow or the empirical result of fully turbulent flow for the indications of the onset and the end of turbulence transition. Although both the laminar flow and the fully turbulent flow can be resolved separately by numerical modellings, the lack of numerical modelling for the prediction of the turbulence transition has been a longstanding gap for the computational fluid dynamics. Recent progress in the modelling of the Reynolds-averaged equations for turbulent transition in external flows, mainly for aerodynamics, has inspired great interest in applying this approach to internal flows. This modelling is generally termed as a local correlation-based transition model (LCTM) (Menter, Langtry et al. 2006b) which consists of two transport equations that forms a framework for

implementing LCTM with the experimental correlation into the general-purpose CFD code.

Recently this turbulence transition model has been firstly applied to the internal flow in the circular pipe by Abraham et al. (Abraham, Sparrow et al. 2008). The modelling is validated by comparing the friction factor with theoretical and empirical friction factors in the laminar and fully turbulent regimes, respectively. It offers a numerical approach to explore the turbulence transition for internal flows. Following this success, this model has been applied to the simulation of heat transfer. The heat transfer coefficient predicted by this transition model has been verified (Abraham, Sparrow et al. 2009) and the simulation for Nusselt numbers in low and intermittent Reynolds numbers has been achieved very recently (Abraham, Sparrow et al. 2011). This model has also been applied to various geometric channels such as the parallel-plate channel (Minkowycz, Abraham et al. 2009) and the diverging conical duct (Sparrow, Abraham et al. 2009). It has been further applied to the flow relaminarization where the flow is turbulent in the beginning and regains laminarization downstream (Abraham, Sparrow et al.

2010). All these successes demonstrate the great potential of this transition turbulence model.

In this chapter, we applied this transition turbulence model to the simulation of circular micro-tube as well as rectangular micro-channel where the parallel-plate channel is a limiting case. The purpose of our study as mentioned before is to search for numerical approaches suitable for simulating the flow regimes in microfluidics that have not been simulated yet (i.e. the transitional to fully turbulent flows). Now through an intensive search as briefed above, the recently developed LCTM modelling seems to fit all the criteria for our search and we would like to further validate this numerical approach for internal flow in more general cases and, then, in the microscale cases. Here, the numerical friction factors and the velocity profiles obtained from simulation are to be further analysed against micro-PIV results obtained from the literature. The goal of this study is to offer a numerical approach of Reynolds averaged Navier-Stokes equations suitable for microchannels across the whole regimes of flow including the laminar, transitional turbulent and turbulent flows.

2.2 Simulation Model

There are two models with different geometrics employed in our simulations. Case 1 is a rectangular micro-channel and case 2 is a circular micro-tube. The model geometries are such selected because they can be compared with available micro-PIV data in the literature (Li, Ewoldt et al. 2005, Li and Olsen 2006b, Natrajan, Yamaguchi et al. 2007). For case 1, it is a three-dimensional rectangular micro-channel with a width 320 μm and a height 330 μm. Its aspect ratio is 0.97 and hydraulic diameter is 325 μm. The length of micro-channel is 50,000 μm. The measured surface roughness of the microchannel from the experiment is approximately 24 nm in arithmetic average, which corresponds to 0.000074 of the relative roughness (Li and Olsen 2006b). This relative roughness has little effect on the flow investigated where the Reynolds number is below 10^4 such that the flow behaves much like in a smooth pipe. For case 2, it is a circular micro-tube with a hydraulic diameter of 536 μm. The length of micro-tube is 120,000 μm. The maximum peak-to-valley inner surface roughness of micro-tube is measured within a few nanometres (Natrajan and Christensen 2007). The micro-tube can also be seen as a smooth pipe for our simulation.

2.2.1 Governing Equations of LCTM

The numerical model employed here was devised by Menter et al. (Menter, Langtry et al. 2006a). The governing equation of LCTM is comprised of three sets of equations (Abraham, Sparrow et al. 2008). The first set represents the continuity equation and the Reynolds-averaged Navier-Stokes (RANS) equation.

$$\frac{\partial u_i}{\partial x_i} = 0 \tag{2.1}$$

$$\rho\left(u_i \frac{\partial u_j}{\partial x_i}\right) = -\frac{\partial p}{\partial x_i} + \frac{\partial}{\partial x_i}\left((\mu + \mu_{turb})\frac{\partial u_j}{\partial x_i}\right) \tag{2.2}$$

where $j = 1,2,3$

Where ρ is the density and p is the pressure. u_1, u_2, u_3 denote the x_1, x_2, x_3 (i.e. x,y,z) components of mean flow velocity, respectively. μ and μ_{turb} denote the viscosity and turbulent viscosity, respectively. The second pair represents the Shear Stress Transport (SST) turbulence model for kinetic energy and dissipation rate, which was also formulated by Menter (Menter 1994). The SST model yields the prediction of turbulent viscosity μ_{turb} for eq. (2.2).

$$\frac{\partial\left(\rho u_i k\right)}{\partial x_i} = \gamma P_k - \beta_1 \rho k \omega + \frac{\partial}{\partial x_i}\left[\left(\mu + \frac{\mu_{turb}}{\sigma_k}\right)\frac{\partial k}{\partial x_i}\right] \tag{2.3}$$

$$\frac{\partial(\rho u_i \omega)}{\partial x_i} = \alpha\rho S^2 - \beta_2 \rho\omega^2 + \frac{\partial}{\partial x_i}\left[\left(\mu + \frac{\mu_{turb}}{\sigma_\omega}\right)\frac{\partial \omega}{\partial x_i}\right] + 2(1-F_1)\rho\frac{1}{\sigma_{\omega 2}\omega}\frac{\partial k}{\partial x_i}\frac{\partial \omega}{\partial x_i} \tag{2.4}$$

Where P_k is the production rate of turbulent kinetic energy k and ω denotes the specific rate of turbulence destruction. σ terms denote the prandtl numbers for the transport of k and ω. S denotes the absolute rate of shear strain rate. F_1 and F_2 denotes the blending function of SST model. α, β_1 and β_2 denote the SST model constants. Solving eq. (2.3) and (2.4), one can obtain the turbulence viscosity μ_{turb} in terms of k and ω.

$$\mu_{turb} = \frac{\alpha\rho\kappa}{\max(\alpha\omega, SF_2)} \tag{2.5}$$

To couple the turbulence model with the transition model, the SST model has been modified with the intermittency γ in production term P_k, which will dampen the production term in the regions of laminar flow and turbulence intermittency. The last set of equations is the transport equations for the transition, i.e. the intermittency transport equation and transition momentum-thickness transport equation.

$$\frac{\partial \rho\gamma}{\partial t} + \frac{\partial \rho u_i \gamma}{\partial x_i} = P_{\gamma,1} - E_{\gamma,1} + P_{\gamma,2} - E_{\gamma,2} + \frac{\partial}{\partial x_i}\left[\left(\mu + \frac{\mu_{turb}}{\sigma_\gamma}\right)\frac{\partial \gamma}{\partial x_i}\right] \tag{2.6}$$

$$\frac{\partial \rho \, \mathrm{Re}_{\theta t}}{\partial t} + \frac{\partial \rho u_i \, \mathrm{Re}_{\theta t}}{\partial x_i} = P_{\theta t} + \frac{\partial}{\partial x_i}\left[\sigma_{\theta t} (\mu + \mu_{turb}) \frac{\partial \mathrm{Re}_{\theta t}}{\partial x_i} \right] \tag{2.7}$$

where $\mathrm{Re}_{\theta t}$ is transition momentum thickness Reynolds number. $P_{\gamma,1}$ and $P_{\gamma,2}$ are the source terms of intermittency equation. $E_{\gamma,1}$ and $E_{\gamma,2}$ are the destruction term of intermittency transport equation. $P_{\theta t}$ is the source term of transition momentum-thickness transport equation. The intermittency equation in eq. (2.6) is used for triggering the turbulence transition and turning on the production term in eq. (2.3) and the momentum-thickness transport equation in eq. (2.7) is used for connecting the transition onset criteria of the intermittency equation with the empirical correlation that is based on the relation between transition momentum thickness and strain-rate Reynolds number.

This Reynolds-averaged turbulence model can be used for predicting the mean fields of transitional turbulence flow as well as the laminar flow and fully turbulent flow to form a complete description of the Navier-Stokes equations. The model devised by Menter et al. was specifically for the external flow, which was based on the experimental correlation to calibrate the empirical constants for the applicability of this transition model. For

application to internal flow, the calibration of the empirical constants has to be done. Here, we have adapted the empirical constants from Abraham et al. (Abraham, Sparrow et al. 2008) , which are determined by systematic evaluation. The modifications of the model are an increase of constant $C_{\gamma,2}$, appearing as a multiplier of $E_{\gamma 2}$ in the intermittency equations, from 50 to 70 and a reduction of constant $C_{\theta,t}$, appearing in the production term of the transport equation, from 0.03 to 0.015. Although the empirical correlation and the transition model are originally devised in the conventional macroscale system, there are some statistical and structural similarities between microscale and macroscale in wall turbulence (Li and Olsen 2006a, Natrajan, Yamaguchi et al. 2007, Elsnab, Maynes et al. 2010). As the result, the empirical correlation method developed under the conventional system should offer the same capabilities for exploring the microscale system. For further details on the transitional model readers are referred to (Langtry, Menter et al. 2006, Menter, Langtry et al. 2006a, Menter, Langtry et al. 2006b).

2.2.2 Numerical Implementation

The numerical simulation has been performed by using the ANSYS CFX

13.0 and 14.0 softwares. CFX uses a coupled solver to solve the hydrodynamic equations simultaneously as a single system. A fully implicitly, false transient, and time-stepping algorithm is used for approaching the steady state solution which reduces the number of iterations for achieving convergence. For reducing the source of solution errors a high resolution advection scheme has been adapted for all equations including hydrodynamic equations, turbulent equations and transitional equations. It gives a dynamic adjustment and better trade-off between the order of accuracy and the robustness. The method developed by Rhie and Chow (Rhie and Chow 1983) and modified by Majumdar (Majumdar 1988) has been adapted by CFX for avoiding the velocity-pressure decoupling, which imposes the velocity-pressure coupling equation onto the non-staggered grid layout and removes the dependence of the steady-state solution on time step. A high resolution scheme is also adapted for the Rhie Chow pressure dissipation algorithm.

The solution domain has been selected as the same length as the geometrical model, which extends from the inlet of channel to a location around 153 and

224 hydraulic diameters downstream for the rectangular microchannel and micro-tube, respectively. The channel is long enough to achieve a fully developed flow to avoid the entrance effect and to allow the flow to develop through various transition processes. Assuming a symmetric of flow, only one quarter of cross section of rectangular micro-channel is simulated, that is, the solution domain is a cross section of 160 μm in width and 165 μm in height. It thus reduces the simulation time significantly. The simulation of micro-tube can also be simplified as a two dimensional axisymmetric pipe flow, which will further reduce the computational cost. As for the boundary condition, no-slip and impermeability conditions have been imposed on all wall boundaries. The inlet velocity and outlet pressure are specified. In particular, the inlet velocity profile is uniform and normal to the cross section of the inlet. The specification of the inlet velocity is equivalent to the corresponding Reynolds numbers. Turbulence intensity *Tu* is sufficient for the specification of the other turbulent quantities of turbulence model. Here, the selected value of *Tu* was 5 percent. Although the intermittency γ is set as 1 in the model as the default, it drops quickly to its natural value as the flow is developed along the channel. To validate the model, the friction factor in

the fully developed region is used for comparing with those obtained from the literature. The criterion of convergence has been set for residual values of 10^{-6} except for the intermittency residual value of 10^{-5}.

2.2.3 Mesh Independence Study

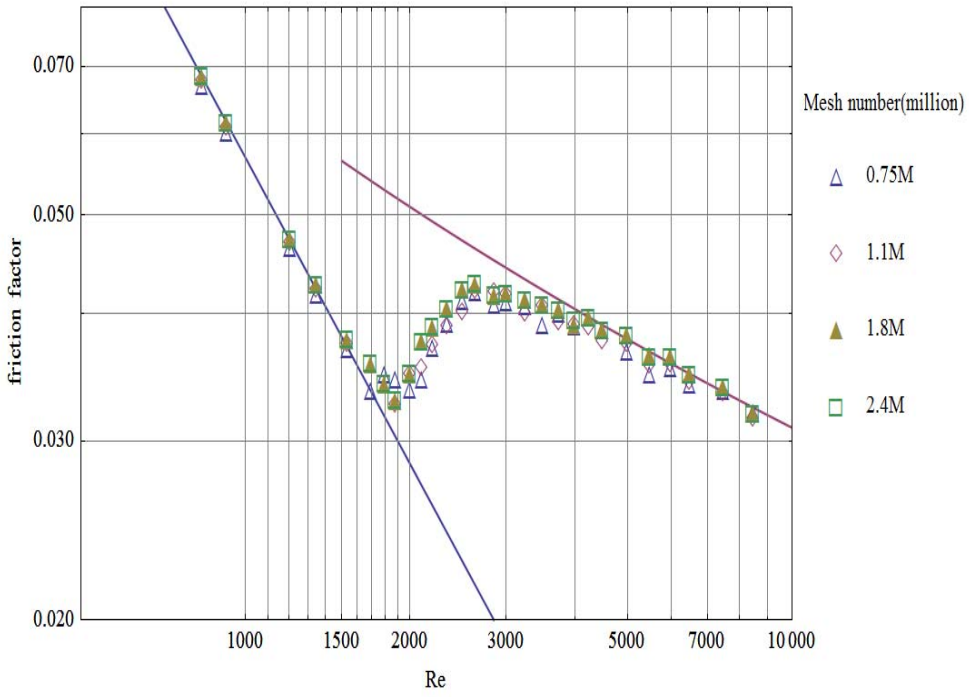

Fig. 2.1 The mesh independency for rectangular channel case.

The study of mesh independency has been done for the discretization of solution. Approximately 1,946,000 nodes are deployed with 1,828,000 elements for the simulation of rectangular microchannel. Extra care has been taken to fulfil the criterion $y^+ < 1$ along stream-wise locations for all

Reynolds numbers investigated such that all the near-wall elements are resolved properly. The mesh independency study is shown in Fig. 2.1 for the rectangular micro-channel case. The mesh independency has been achieved when the mesh number increase to 1.8 millions.

2.3 Result and Discussion for the Simulation of Rectangular Microchannel

The results obtained from the simulation are compared with those from the literature. In particular, the friction factor is used for the validation of our simulation. Through numerical simulation, one can obtain enormous and complete fluid dynamics data to be used for the elucidation of the flow behaviours both quantitatively and qualitatively. Furthermore, we use the velocity profile obtained from the simulation for the analysis against the results obtained from micro PIV in the literature.

2.3.1 Friction Factor of Fully Developed Flows

The simulation data have been obtained by varying the inlet velocity corresponding to the Reynolds number ranging from 833 to 8500. Here, Re is

defined as the Reynolds number based on the inlet velocity and the hydraulic diameter. The friction factor calculated from fully developed flow region covering laminar, transitional turbulent and fully turbulent regimes as plotted in Fig. 2.2. The dots represent the friction factor obtained from our simulation. The result is compared with the data from White (White 2008) where laminar friction factor based on the analytical solution is used for the comparison in laminar flow regime; and, for fully turbulent regime, turbulent friction factor based on an empirical equation developed by Haaland (Haaland 1983) is used, which is an explicit and simplified form of Colebrook-White formula. Figure 2.2 indicates that the model has accurately simulated the friction factor in both the laminar and fully turbulent regimes, for which the model is validated. In the transitional turbulent regime, the simulation data can be fitted as a polynomial equation as shown in eq. (2.8).

$$f_{tr} = -0.186+2.51\times10^{-4}\mathrm{Re}-10^{-7}\mathrm{Re}^2+1.72\times10^{-11}\mathrm{Re}^3-1.08\times10^{-15}\mathrm{Re}^4 \quad (2.8)$$

The corresponding Reynolds number for fitting the transitional turbulent regime ranges from 1885 to 4250 that follows closely the traditional

prediction of turbulence transition. The solid line in transitional turbulent regime represents the fitting equation which predicts the friction factor of turbulence transition in the rectangular micro-channel.

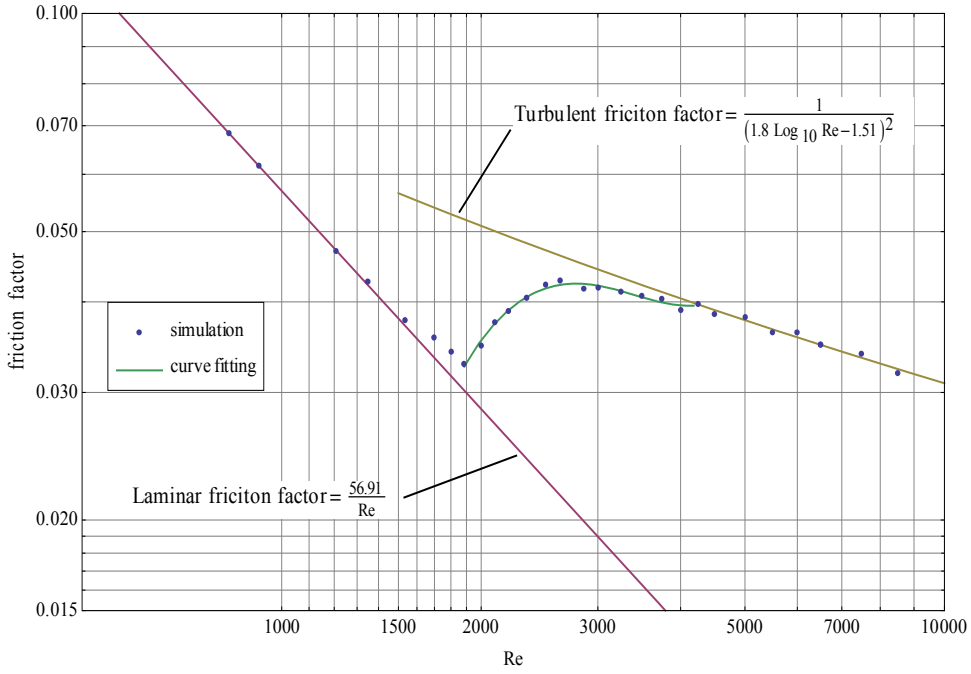

Fig. 2.2 Rectangular case: the computed friction factor compared with the moody chart

2.3.2 Velocity Profile

Since there is no well-defined and accurate theory for predicting the friction factor in the transitional turbulent regime that could be used for comparison, instead we have employed the maximum velocity and corresponding velocity profile obtained from micro-PIV studies for comparison. Figure 2.3 shows the comparison of maximum velocities. The experimental data are obtained

from Li et al. (Li, Ewoldt et al. 2005) and Li and Olsen (Li and Olsen 2006b).

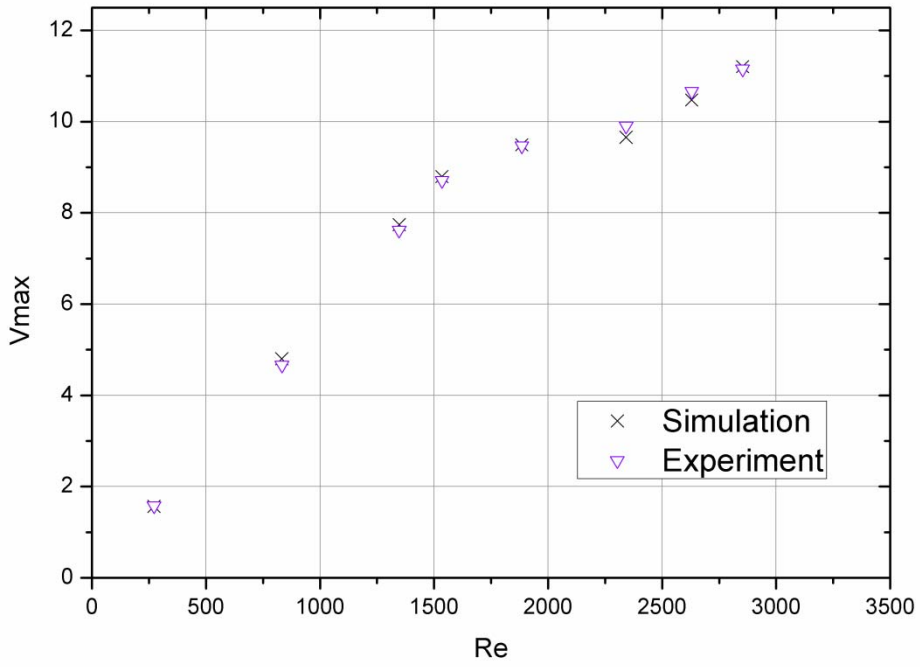

Fig. 2.3 The maximum velocity of fully developed flow

Their data are within the laminar and transitional turbulent regimes where the maximum velocity is obtained on the centreline of channel in fully developed region. The maximum error among the compared maximum velocities, occurring at Reynolds number 2342, is less than 2.5 percent which is within the order of uncertainty of micro-PIV. This comparison of maximum velocity demonstrates at least an acceptable simulation result. Much more confidence on the simulation results can be achieved by comparing the velocity profile as

shown below.

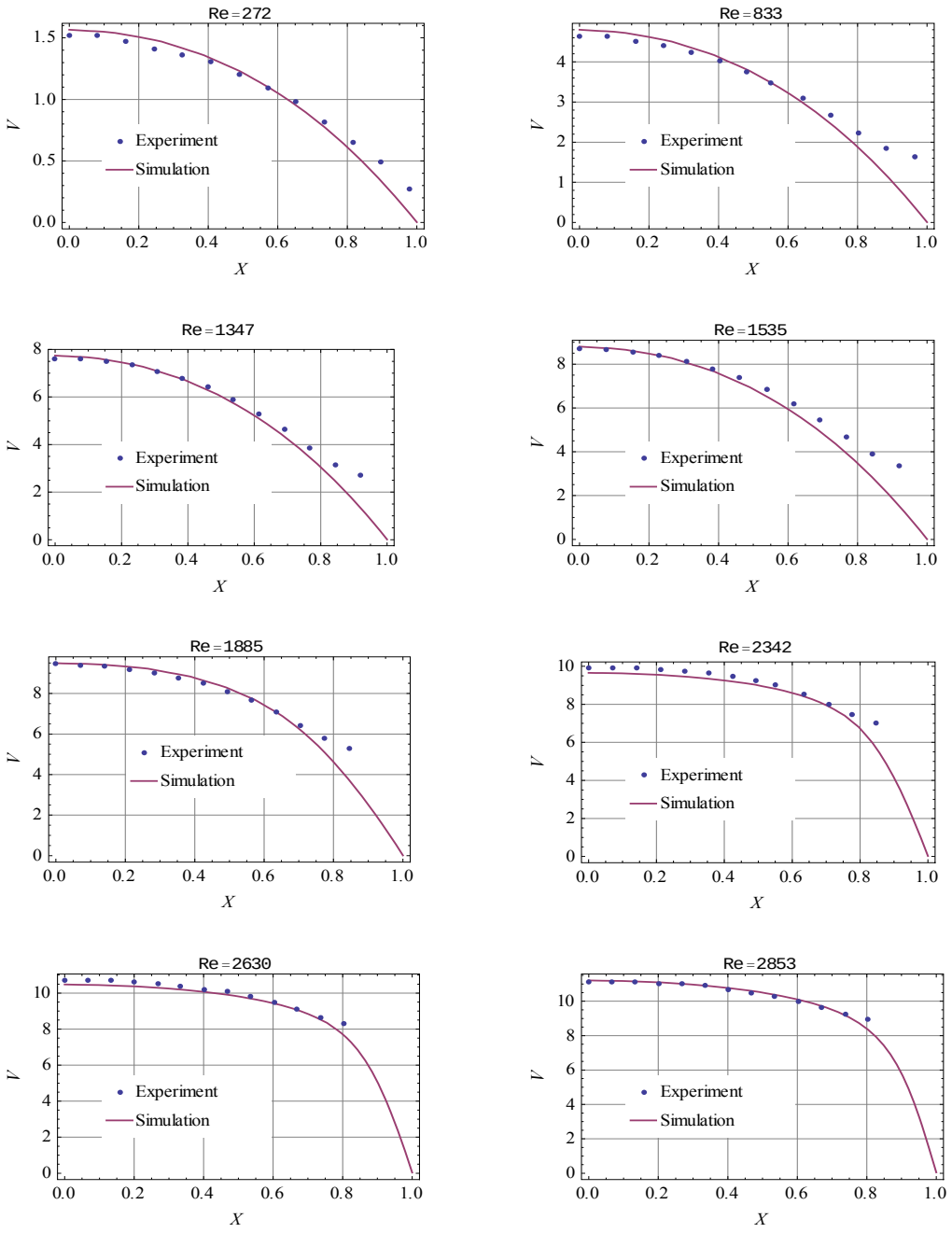

Fig. 2.4 various velocity profiles of fully developed flow against the normalized width of channel

The further comparison of velocity profiles between the experiment and the simulation is shown in Fig. 2.4. The abscissa represents the normalized width

of channel from the centre of channel where the abscissa is designated as 0 to the wall of channel where the abscissa is designated as 1; whereas, the ordinate represents the velocity of flow in the fully developed region. The maximum velocity of flow occurs at the centre of channel; the minimum velocity occurs at the wall of channel.

Figure 2.5 shows all the velocity profiles against Reynolds number. The dots are experimental data and the solid lines are simulation results. The simulation data accurately predict the velocity profile for both flow regimes within the normalized width between 0 and 0.7. The range between 0.7 and 1 is the near-wall region where the micro-PIV is hardly to resolve accurately as shown by the shapes of the curves which are obviously deviating from normalities in the near wall region. Whereas, the shape of the calculated velocity profiles varies against the Reynolds number properly, rendering a parabolic law for laminar regime; a logarithmic law for fully turbulent regime; and a shape variation from parabola to logarithm for transitional regime. This reflects very well the characteristics of the transition from the laminar flow throughout transition regime to the fully turbulent flow.

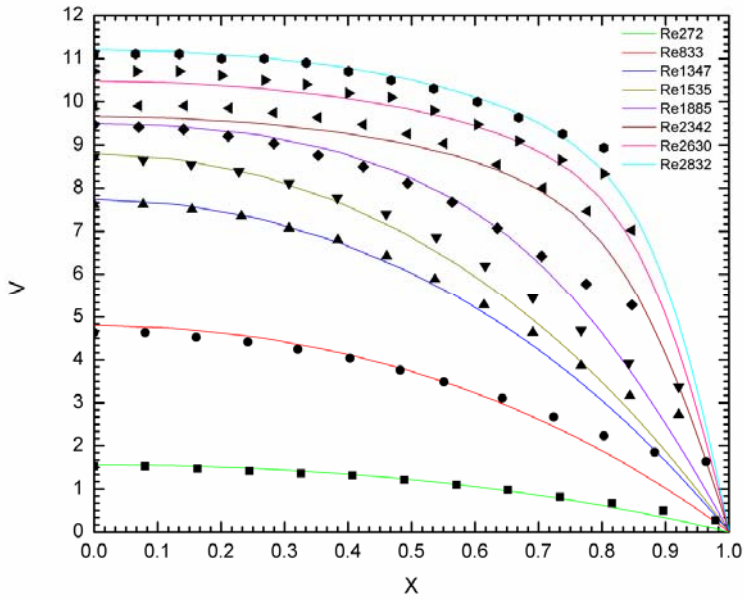

Fig. 2.5 Velocity profiles ranging from Reynolds number 272 to 2853

Normalized velocity profiles show more clearly the shape variation of velocity profile against Reynolds number as shown by Fig. 2.6. The abscissa represents the normalized width of channel and the ordinate represents the normalized velocity. The normalized velocity profile and its variation against Reynolds number obtained from our simulation have again convinced the accuracy of our prediction as explained before. Figure 2.7 groups the normalized velocity profiles for various Reynolds numbers into three groups. As the Reynolds number is low, the normalized velocity profiles are grouped closely to the laminar flow which is a parabolic shape.

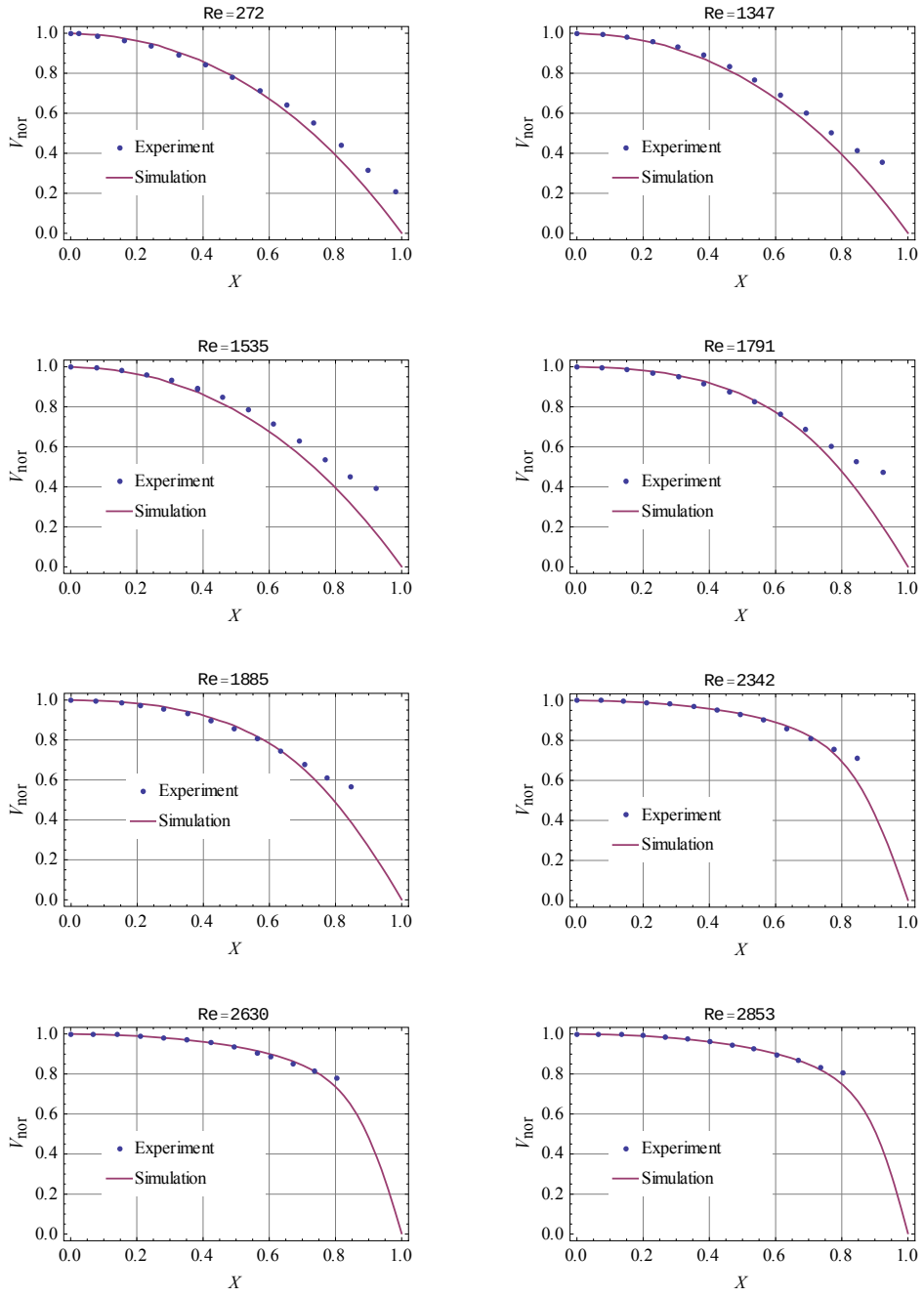

Fig. 2.6 Various normalized velocity profile against the normalized width of channel

While the Reynolds number increases, the profiles start deviating from the laminar parabolic solution towards the turbulent logarithmic solution, i.e. the third group. This deviation happens from Reynolds number 1885 which

indicates the beginning of turbulence transition. This value of Reynolds number is also indicated from the graph of friction factor, referring to Fig.2.3. Though the shape deviation can be identified for the Reynolds number between 1700 and 1885, they still maintain a quasi-parabolic shape, as also indicated in the graph of friction factor. Immediately after Reynolds number reaches 1885, the burst of the turbulence transition starts corresponding to a sudden jump of the friction factor.

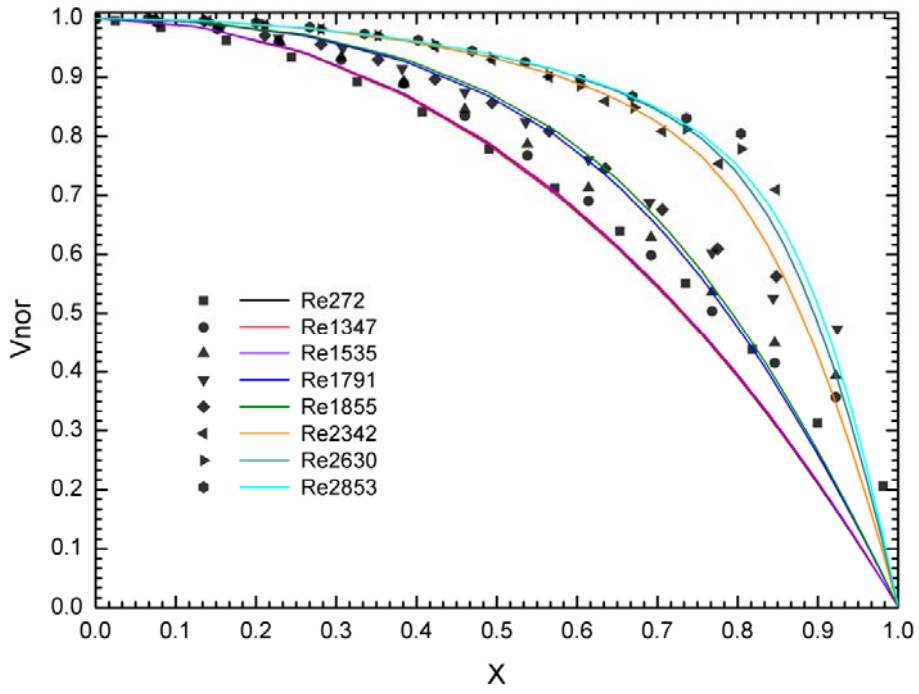

Fig. 2.7 Normalized velocity profiles ranging from Reynolds number 272 to 2853

From Fig. 2.8 it is clearly demonstrated that the transition process is reflected by a continuous variation of velocity profile, which is almost synchronised

with the variation of friction factor. That is if the friction factor varies fast, the shape of velocity profile will also changes fast such as for the Reynolds number between 1885 and 2630. On contrast, the shape variation slows down after the Reynolds number of 2630 where the corresponding friction factor also changes slowly. In the fully turbulent regime where the Reynolds number exceeds 4250, as indicated by Fig. 2.2, the variation of shape against Reynolds number becomes much slower and even negligible.

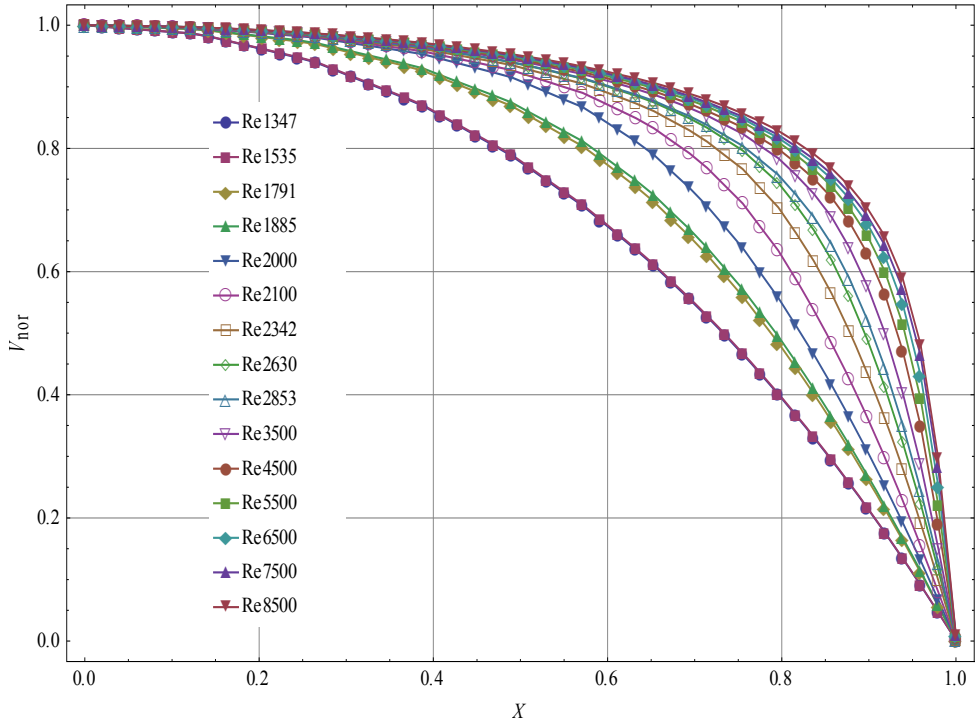

Fig. 2.8 Normalized velocity profiles ranging from Reynolds number 1347 to 8500

These comparisons indicate that our approach established based on the local

correlation-based transition model is suitable for the simulation of transitional turbulence flow in the micro-channel, in particular with the rectangular cross-section. This approach has thus filled up the gap of simulation between the laminar and fully turbulent flows.

2.3.3 Flow Development along Streamwise Direction

Various information of flow field can be obtained from the numerical simulation, which facilitates a better understanding of fluid dynamics in microchannel. Figure 2.9 shows the flow development of the ratio of maximum velocity to mean velocity $V_{\max}/V_{ave}$ in the streamwise direction throughout the entire flow regimes. The streamwise axis is normalized by the hydraulic diameter d_h. The three different behaviours of flow are presented clearly in this figure. The laminar flows, i.e. Re=1347 and Re 1535, are developing smoothly and monotonically towards the fully developed flow. The transitional turbulent flow, i.e. Reynolds number from 1885 to 4000, develops toward a fully developed intermittency which is proposed by Abraham et al. (Abraham, Sparrow et al. 2008) after the initial laminar flow development. The distance for this initial laminar development decrease as

the Reynolds numbers of flow increase. Immediately after the breakdown of initial laminar development, the fully turbulent flows, i.e. Re=5000 and 6000, attain the fully developed flow very quickly.

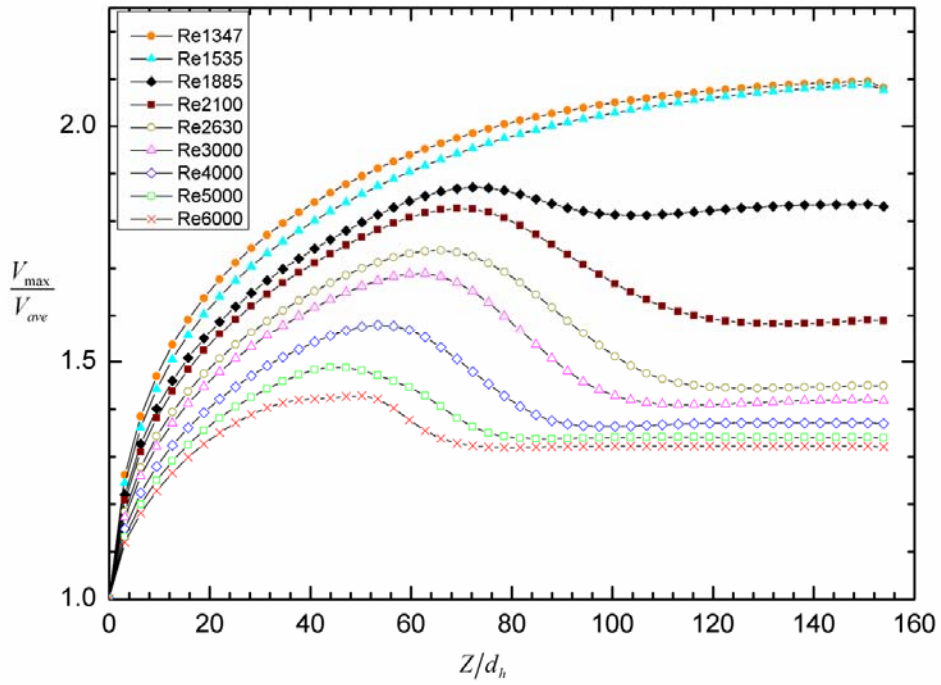

Fig. 2.9 The streamwise flow development of the ratio of maximum velocity to mean velocity

Another flow characteristic predicted by LCTM transitional model is the development of turbulent eddy viscosity μ_{turb}/μ_m, i.e. normalized by molecular viscosity, against the streamwise direction as shown in Fig. 2.10. Although a turbulent intensity of 5 %, i.e. $\mu_{turb}/\mu_m = 10$ is set as the default for all the simulation as prescribed before, the turbulent eddy viscosity

decays immediately in very short distance and is suppressed successfully to 0 in the laminar flow case. Whereas, In the cases of transitional turbulent and fully turbulent flows, the turbulent eddy viscosity grows steadily with the increase of Reynolds number.

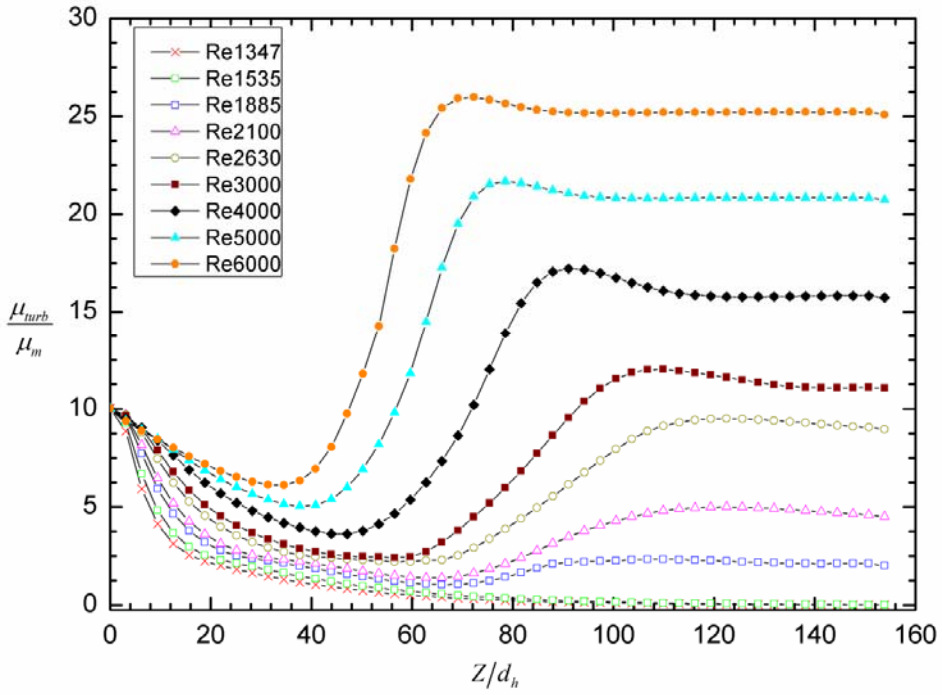

Fig. 2.10 The streamwise flow development of eddy viscosity

2.4 Result and Discussion for the Simulation of Micro-tube

By varying the inlet velocity, various simulation results of micro-tube against corresponding Reynolds numbers can be obtained. In this case, the Reynolds number varies from 1000 to 6000 covering all regimes, i.e. the laminar,

transitional, and fully turbulent flow regimes. As shown in Fig. 2.11, the friction factors calculated from simulation data are also compared with the Moody chart as for the rectangular case. The theoretical friction factor of circular tube shown as the solid line in laminar regime and the turbulent friction factor obtained from the empirical Colebrook-White formula shown as the solid line in fully turbulent regime are used for comparison. Whereas, the dots between the laminar and fully turbulent regimes are the calculated friction factor obtained from the simulation.

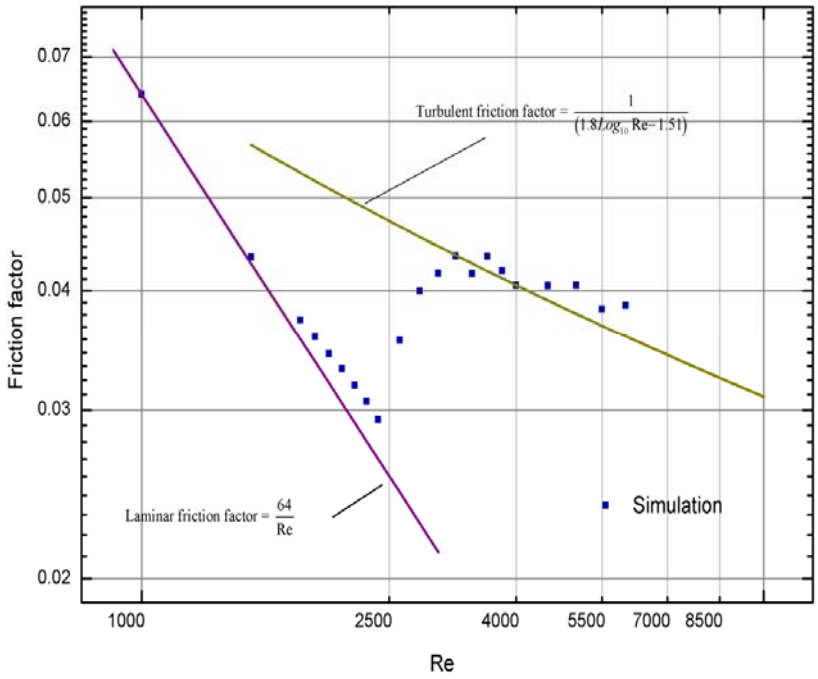

Fig. 2.11 Circular case: the computed friction factor compared with the Moody chart

Figure 2.11 shows again the match for laminar and fully turbulent regimes

between our simulation data and the empirical formula as well as the laminar theoretical prediction. The pipe flow characteristics simulated by this LCTM transition model is accurately predicted, though with a slight deviation in quantity. In the paper of Natrajan and Christensen (Natrajan and Christensen 2007), by varying flow rate, the pressure drops across the micro-tube against various Reynolds numbers were measured. These measured data of pressure drop and friction factor were compared with conventional laminar theory as well as the experimental results obtained from Sharp and Adrian (Sharp and Adrian 2004).

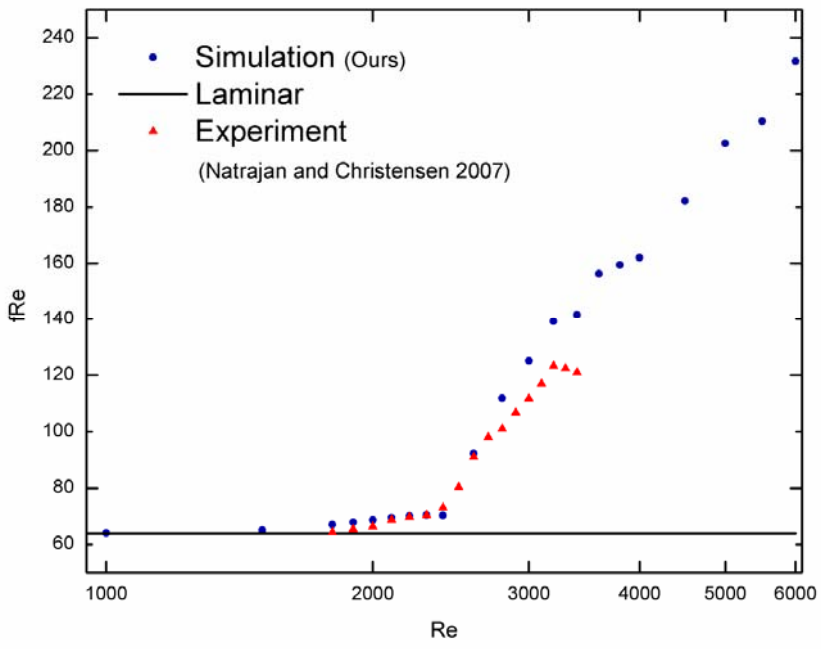

Fig. 2.12 Circular case: the variation of $f \cdot \mathrm{Re}$ against Re

Here, we compared their measured data with the calculated friction factors obtained from our simulation as shown in Fig. 2.12. The slight deviation from the analytical laminar flow starts from Re=1800, which is very close to the prediction of experimental result at Reynolds number 1900. Also the behaviour of turbulent transition is accurately predicted by our numerical simulation. As the Reynolds number increases, the discrepancy between simulation results and experimental data slightly increase. By comparing with velocity profile calculated from DNS results (Eggles et al. 1994), fully turbulent flow attained at Reynolds number 3400 was concluded by Natrajan and Christensen (Natrajan and Christensen 2007). However, with this conclusion it raised another discrepancy with the conventional macroscale flow based on the Moody chart, as shown in Fig. 2.13. This discrepancy could be attributed to experimental error in measuring the pressure drop. To justify this discrepancy it requires further information about their experimental setup and conditions to make conclusion. Nevertheless, this is for sure that more experimental data are needed for a complete calibration of this LCTM transition model used for quantitatively and accurately predicting micro-tube flows.

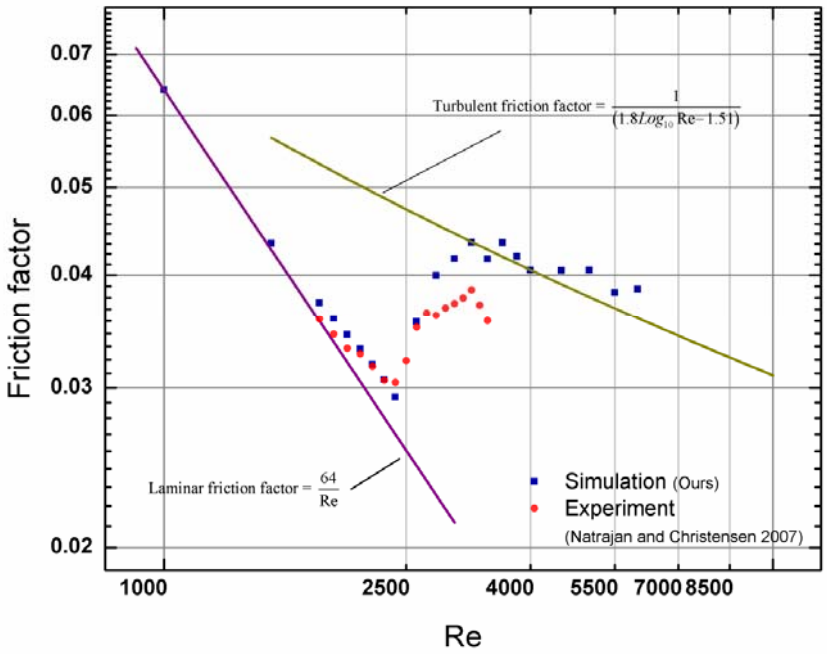

Fig. 2.13 Circular case: the comparison between the computed friction factors (ours) and experimental data from the published literature (Natrajan and Christensen 2007)

2.5 Summary

A numerical approach suitable for predicting turbulence transition in rectangular microchannel has been successfully applied and validated by using a local correlation-based Transition model (LCTM) combining with the SST turbulence model. It can simulate the entire flow regimes from laminar throughout fully turbulent flow. Detail information such as friction factors for laminar, transitional turbulent, and fully turbulent flows in the fully developed region can be obtained by using this approach. The numerical

results show accurate estimations of the friction factor for laminar and fully turbulent regimes by comparing with theoretical values for laminar regime and empirical values for fully turbulent regime. The onset of turbulent transition is also clearly predicted by the calculated friction factor as well as by the normalized velocity profile where both of them start departing from the theoretical value of friction factor for laminar flow and the parabolic shape of laminar flow, respectively. The calculated velocity profile has been compared with micro-PIV results showing good agreement as well. All these evidences indicate that the long lasting problem involved in the study of turbulence transition for micro channels with rectangular cross-sections can be overcome by using micro-PIV combined with the numerical approach investigated here.

Chapter 3

Numerical Simulation of Micromixer

3.1 Introduction

The micromixer is an important microfluidic devices used in the areas of chemistry and life science. The function of micromixer is to mix the fluids homogenously and efficiently in space as well as time domains. The main concept for designing micromixer is to maximise the mixing efficiency and production yields while minimizing the sample consumption. In the bio-chemistry and micro process engineering, micromixer is often used as a micro-reactor where the chemical reaction is taken place. Often rapid mixing of fluids is essential for observing those rapid reactions such as the kinetics of protein folding. For example, in order to explore the early event of protein folding the complete mixing time is required to be within sub-milliseconds. Various designs and operation strategies have been proposed for optimising micromixers by utilising various physical mechanisms such as molecular

diffusion, chaotic advection, and turbulent diffusion as illustrated in Fig. 3.1. The continuous-flow micromixer utilising the turbulent mixing is superior over those discussed previously in the introductory chapter.

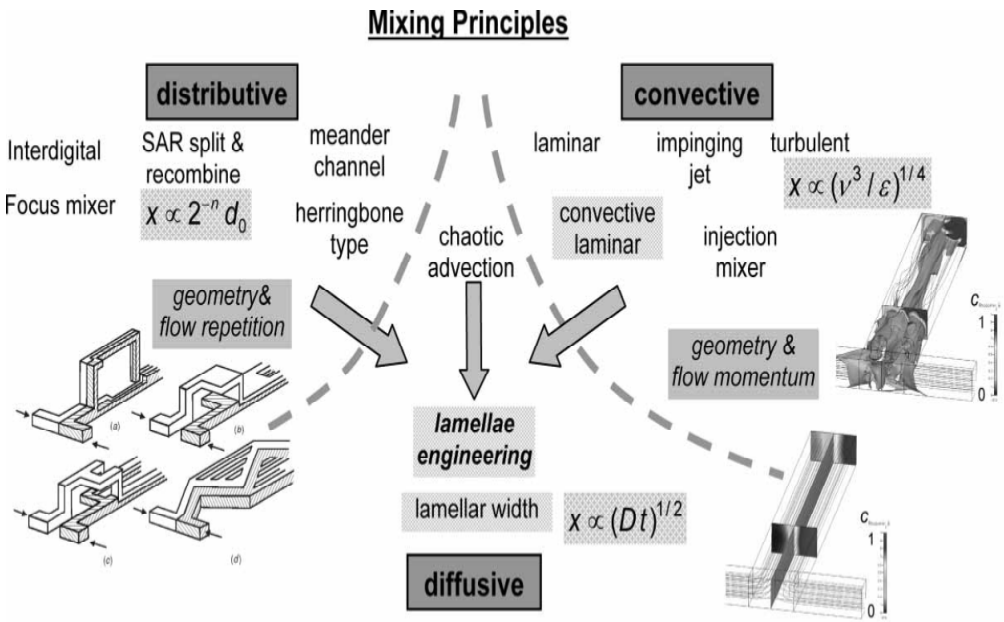

Fig. 3.1 Mixing priciples for micromixer by Kockmann (Kockmann 2008a)

However, in the past time the focus was mainly placed on the laminar and chaotic micromixers owing to the difficulties of imposing and maintaining the turbulent flow in a micro-scale device (Hessel, Lowe et al. 2005, Nguyen and Wu 2005). The extremely high pressure drop generated by high flow rate of fluid in the micromixer can potentially cause the leaking problem of sealing as well as the failure of bonding connection. The appearance of cavitation bubbles could further cause the loss of mixing efficiency and the

erosion on micromixer itself. All of these issues cause the difficulties in investigating turbulent micromixer experimentally. Moreover, lack of experimental data in validating and calibrating a suitable numerical approach makes the CFD studies on turbulent micromixer more difficult.

The mixing mechanism of micromixer in the laminar flow condition mainly relies on the flow convection and molecular diffusion. For more details on various types of laminar and chaotic micromixers the readers are referred to the book (Nguyen 2012). As the in-flow velocity of fluids is low[4], i.e. the Reynolds number is smaller than 10, the mixing is mainly dominated by molecular diffusion. As the Reynolds number becomes higher than this value, the mixing is mainly dominated by convection. A review and classification on the laminar and chaotic flow mixing with the characteristics of their flow pattern is given by Kockmann (Kockmann 2008b). As the Reynolds numbers are increased from 0.01 to 1000, the flow patterns in the mixing channel also varies in sequence, such as from laminar straight streamline, symmetric

[4] The characteristic velocity of flow in the microfluidics typically has a Reynolds numbers approaching to or approximately equal to 0.

vortex flow, engulfment flow[5], periodic pulsating flow, and chaotic pulsating flow. Within this range of Reynolds number, the mixing mechanism is being transformed from laminar diffusion throughout to chaotic convection. These changes on the flow pattern are mainly caused by the induced hydrodynamic instability, i.e. Kevin-Helmholtz instability, which is resulted from the high shear flow between the contact areas of two fluids. This instability leads to the unstable flow condition and periodic fluctuating behaviours of flow. Eventually, the chaotic mixing of flow structure is obtained as the Reynolds number is approximately greater than 500. These classifications are also illustrated by Kockmann (Kockmann 2008a) as illustrated in Fig. 3.2.

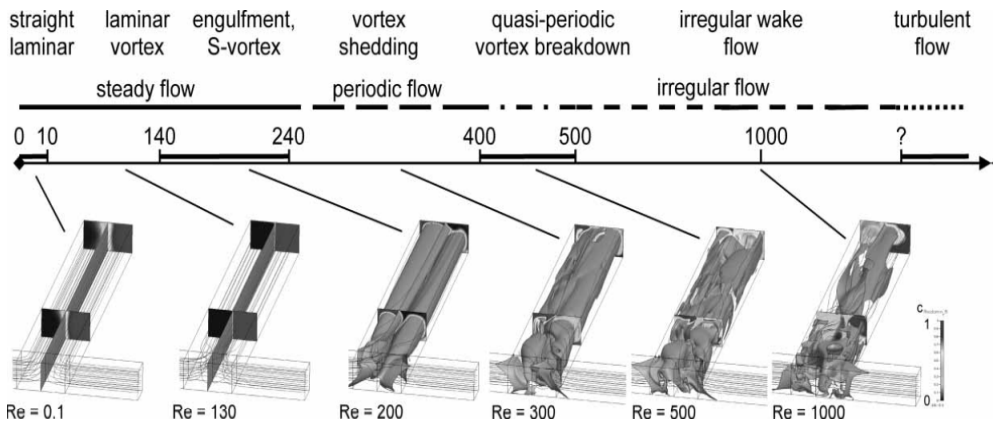

Fig 3.2 The classification of flow regimes on 1:1 mixing by Kockmann (Kockmann 2008a)

[5] The engulfment flow refers to the breakdown of symmetric vortex flow becoming as asymmetric one. The streamlines of fluids are swapped to the opposite side and engulfed to each other.

Soleymani et al. (Soleymani, Kolehmainen et al. 2008) performs a numerical investigation showing that the development of vortices is essential for achieving a good mixing and strongly depends on the flow rate and the geometrical parameters of micromixer such as aspect ratio, mixing angle and throttle size. These dependencies predicted by the numerical simulation also have been investigated experimentally by Sultan et al. (Ashar Sultan, Fonte et al. 2012) and Krupa et al. (Krupa, Ashar Sultan et al. 2012). Recent progress of continuous-flow micromixer utilising turbulent mechanism for mixing has intrigued great interests in investigating a numerical approach for guiding the design of micromixer utilising turbulent mixing. In this chapter, different mixing mechanisms of micro-mixer are investigated by using a newly developed transitional turbulence model. This numerical approach as introduced in the previous chapter enables us to simulate the whole flow regimes including laminar, transition-turbulent, and fully turbulent flows for predicting the turbulent eddy viscosity and the velocity distribution accurately. With these predicted data one can further obtain the scalar transport in the micromixer by solving convection-diffusion equation numerically. Here, in order to simplify the problem but without loss of generality, a basic

T-junction micromixer is employed as the geometric model for simulating and characterizing the flow. As for the discrimination on the mixing quality of a micromixer, the segregation of intensity is employed for quantitatively analysing the simulated micromixer. This numerical approach provides us a CFD tool for guiding and optimising the design of turbulent micromixer.

3.2 Governing Equations of Numerical Simulation for the Micromixer

In order to evaluate the degree of mixing, a passive scalar tracer that has no effect on the material properties such as dye is often used in the experiment of mixing. By utilising the conservation law of species one can derive a convection-diffusion equation to simulate the transport of this scalar property in the micromixer. This scalar transport equation that characterises the convection[6] and molecular diffusion is written as

$$\left(\frac{\partial c}{\partial t} + u_i \frac{\partial c}{\partial x_i} \right) = D_m \frac{\partial^2 c}{\partial x_i^{\,2}} \quad , \quad i = 1 \sim 3 \tag{3.1}$$

[6] Convection refers to the fluid movement exerted by the force acting upon or within it

where c denotes the concentration field of scalar material and D_m denotes the kinematic diffusivity[7], i.e. the coefficient of molecular diffusion determined by the material properties. The term in the right hand side represents the mixing caused by molecular diffusion. The first and second terms in the left hand side represent the time dependence and convection of scalar field, respectively.

By utilising the concept of Reynolds decomposition, the mixture fraction and velocity can be divided into the fields of mean flow and fluctuating flow.

$$\begin{cases} c_i(x,t) = \overline{c}_i(x,t) + c_i'(x,t) \\ u_i(x,t) = \overline{u}_i(x,t) + u_i'(x,t) \end{cases} \tag{3.2}$$

Inserting eq. (3.2) into eq. (3.1), one can obtain

$$\frac{\partial \overline{c}}{\partial t} + \left(\overline{u}_i \frac{\partial \overline{c}}{\partial x_i} + \frac{\partial \overline{u_i' c'}}{\partial x_i} \right) = D_m \frac{\partial^2 \overline{c}}{\partial x_i^{\,2}} \tag{3.3}$$

where $\overline{u_i' c'}$ is the averaged fluctuating flux of the scalar due to the fluctuating velocity. This fluctuating flux is not closed and needed to be

[7] Note that kinematic diffusivity is assumed to be isotropic for simplifying the problem.

modelled. Using the assumption of Reynolds analogy used for Reynolds stress, the scalar flux is assumed to be proportional to the gradient of the mean scalar field $\overline{c}$, i.e. the gradient-diffusion hypothesis, i.e. the fick's law of molecular diffusion.

$$\overline{u_i' c'} = -D_{turb} \frac{\partial \overline{c}}{\partial x_i} \tag{3.4}$$

where D_{turb} is turbulent diffusivity[8], the effective mass diffusion coefficient due to turbulence. By inserting eq. (3.4) into eq. (3.3) the convection Diffusion equation with turbulent diffusion[9] can be obtained

$$\frac{\partial c}{\partial t} + u_i \frac{\partial c}{\partial x_i} = \left(D_m + D_{turb}\right) \frac{\partial^2 c}{\partial {x_i}^2} \quad , \quad i = 1 \sim 3 \tag{3.5}$$

For details on the derivation and discussion on the convection-diffusion equation, readers are referred to books, e.g. (Bird, Stewart et al. 2007) and (Cussler 2009).

---

[8] Note that the turbulent diffusivity is assumed to be isotropic for simplifying the problem.

[9] Note that for the conciseness the overbars for c and u_i in the equation 4.5 are all omitted.

Combining this equation together with LCTM transition model allows us to simulate the scalar transport in the micromixer throughout the entire flow regime including laminar, turbulence transitional, and fully turbulent flows. As discussed previously in the chapter two, the governing equations of LCTM are consisted of three sets of equations. The first set is the continuity equation and the RANS equation. The second set, i.e. the SST turbulence model which predicts the turbulent viscosity, is coupled with the third set of equations, the essential part of LCTM transition model. The LCTM model corrects the prediction of turbulent viscosity and mean flow velocity based on an empirical formula for different flow regimes, especially for the regime of laminar-turbulent transition. In this study, the convection-diffusion equation is connected with the LCTM transition model by the velocity field of flow and the coefficient of turbulent diffusivity D_{turb}. In eq. (3.5), the coefficient of turbulent diffusivity is taken as

$$D_{turb} = \frac{\mu_t}{Sc_t} \tag{3.6}$$

where μ_t is turbulent viscosity and Sc_t is turbulence Schmidt number, which is a dimensionless number representing the ratio of the turbulent

momentum diffusivity to the turbulent mass diffusivity. In order to simplify the problem, Sc_t is fixed as 0.9 in our study and this empirical constant number[10] will be used in all our simulations using LCTM transition model since our aim, here, is to demonstrate and exemplify a viable numerical approach for tackling and evaluating rapid mixing in micromixer, especially for those in the transition-turbulent and fully turbulent regime. Furthermore, as shown in Fig. 2.10, the turbulent viscosity calculated by LCTM transition model is damped to zero in the laminar flow regime as the flow is fully developed. Therefore, the turbulent term in eq. (3.5) thus disappears and resulting in a convection-diffusion equation for laminar flow.

3.3 Evaluation of Micromixer by Mixing Quality

In order to evaluate the mixing quality of a micromixer, a concept for measuring the intensity of segregation is defined by Danckwerts (Danckwerts 1958). The segregation in a mixture means that some parts of mixture contain

[10] The value 0.9 is a non-universal empirical constant number generally adopted in CFD simulation of turbulent flow modelling. However, its adaptability in the transition-turbulent regime will require further experimental investigation.

a higher concentration of material than the average concentration in the mixture. The Danckwerts' intensity of segregation I_s that describes a relative variance of the concentration in a mixture is as follows.

$$I_s = \frac{\sigma^2}{\sigma_{\max}^2} \quad , \quad \sigma^2 = \int_A \left(c - \overline{c}\right)^2 dA \tag{3.7}$$

where σ^2 is the variance of concentration field c and $\overline{c}$ is the mean value of concentration field. $\sigma_{\max}^2$ is a reference value for the normalization, which can be defined as the maximum possbile variance as shown by eq. (3.8) or as the variance at the initial time or at the entrance of mixing channel (Bothe, Stemich et al. 2008).

$$\sigma_{\max}^2 = \overline{c}\left(c_{\max} - \overline{c}\right) \tag{3.8}$$

Here, we employed the definition from Danckwerts' original work for our numerical investigation. In a binary mixture, assume that there is one component of mixture with an average volume fraction $\overline{a}$. Then another component of the mixture is $1-\overline{a}$. Therefore, the maximum possible variance $\sigma_{\max}^2$ is $\overline{a}\left(1-\overline{a}\right)$.

$$I_s = \frac{\sigma^2}{\bar{a}(1-\bar{a})} \quad , \quad \sigma^2 = \frac{1}{|A|}\int_A (a-\bar{a})^2 dA \tag{3.9}$$

Herein, a measure for the intensity of segregation I_M is given as

$$I_M = 1 - \sqrt{I_S} = 1 - \frac{\sigma}{\sigma_{\max}} \tag{3.10}$$

where I_M varies from the value of one to zero, corresponding to homogeously mixing and completetly segregated states, respectively. For more detail discussion on the evaluation of mixing quality, readers are referred to the book (Bockhorn, Mewes et al. 2010).

3.4 Mixing Simulation Using LCTM Transition Model for T-junction Micromixer

The T-junction micromixer is a simple but typical micromixer for demonstration purpose as illustrated in Fig 3.3. The orthogonally connected intersection between inflow and outflow channels allows us to examine the influence of mixing mechanisms such as diffusion, convection, turbulence and their combinations etc. The mixing process in this type of micromixer is initiated by a head-on collision of two fluids injected separately into the

in-flow channels in the junction where the in-flow and out-flow channels are joined together. After a bend of 90 degree on the direction of both fluids, the joining fluids are mixed as it flows through the out-flow channel, i.e. the mixing channel of micromixer.

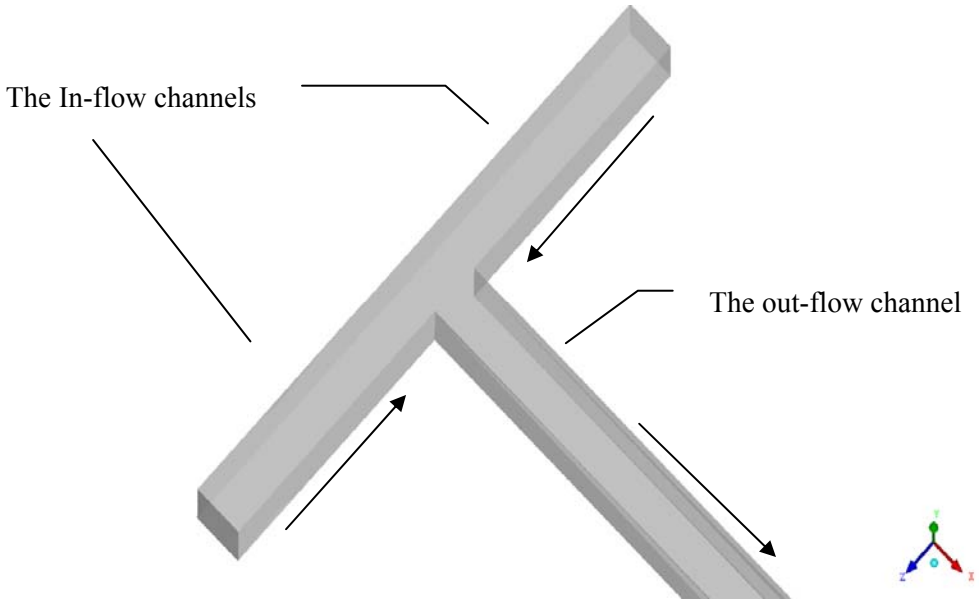

Fig. 3.3 Illustration of T-Mixer

The geometric model we used here is a typical T-junction micromixer with a rectangular cross-section of 100 by 100 μm[11] across the entire micromixer where the hydraulic diameter[12] D_h is 100 μm. The T-mixer is 5 D_h long in

[11] i.e. the symmetrical 1:1 mixing.

[12] The hydraulic diameter D_h is defined as $\frac{4A}{P}$ where A is the cross section area and P is the wetted perimeter of the cross section.

the inlet channels and 100 D_h long in the outlet channel. The numerical implementation is realized by the CFD software, ANSYS CFX, as discussed in the chapter 2. The mesh requirement is taken to be the same criteria as the micro-channel simulation in the chapter 2. Approximately 1,060,711 nodes are deployed with 1,008,000 elements for the simulation of micromixer. The special criterion $y^+ < 1$ is fulfilled to resolve the near-wall behaviour of flow for all the simulation along the stream-wise location. Firstly, we implement the laminar flow simulation to examine the mixing quality of this T-junction micromixer.

In Fig. 3.4, the mixing efficiency of simulated micromixer at distance of 2000 um after the flow enters mixing channel is shown against Reynolds number[13]. It shows that the mixing quality are high as the Reynolds numbers are either extremely low or higher enough. This is because as the flow velocity is extremely slow, the fluids has a very long residence time to diffuse in the mixing channel. However, To complete the mixing, attaining a high mixing

[13] Note that all the Reynolds number mentioned in this chapter is based on the in-flow velocity.

efficiency, would require a huge amount of time. For example, in this case, it would take approximately 1.57 s for the flow of Reynolds number 0.01 to arrive at the location of 2000 um in the mixing channel whereas it only takes 15 us for the flow of Reynolds number 750.

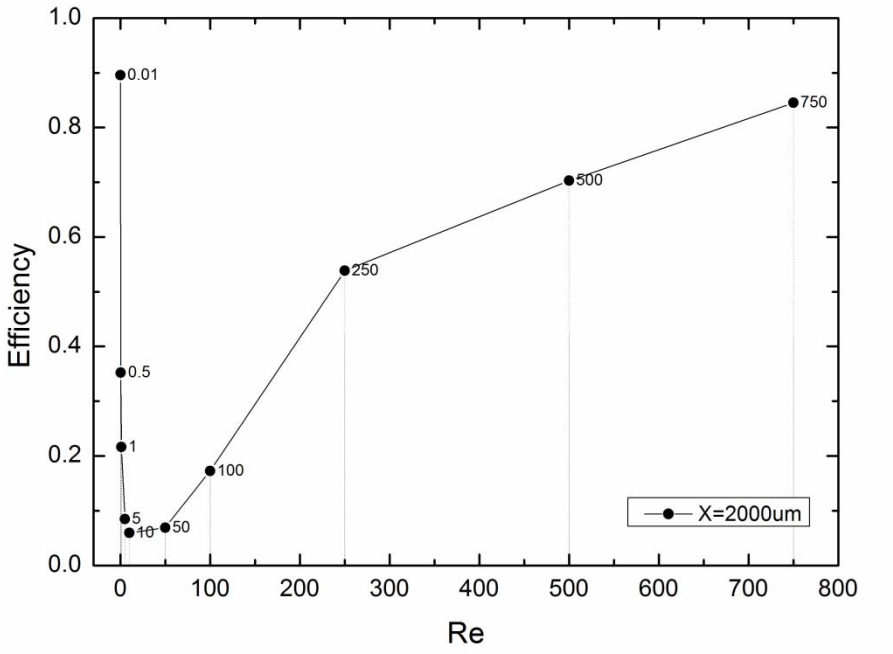

Fig. 3.4 Mixing efficiency against Reynolds number (laminar simulation)

In contrast, as the Reynolds number is higher enough, the roll-up of vortex flow structure is generated by the convection of flow, resulting in the reduction on the striation thickness of flow, i.e. the distance between two components. Herein, the mixing efficiency of micromixer is increased. For the Reynolds number ranging from 1 to 100, the mixing efficiency is

relatively low because there is no enough time for diffusion of the (virtually) straight laminar structure of flow in the mixing channel. For details of discussion on these flow characteristics, please refer to (Kockmann 2008b).

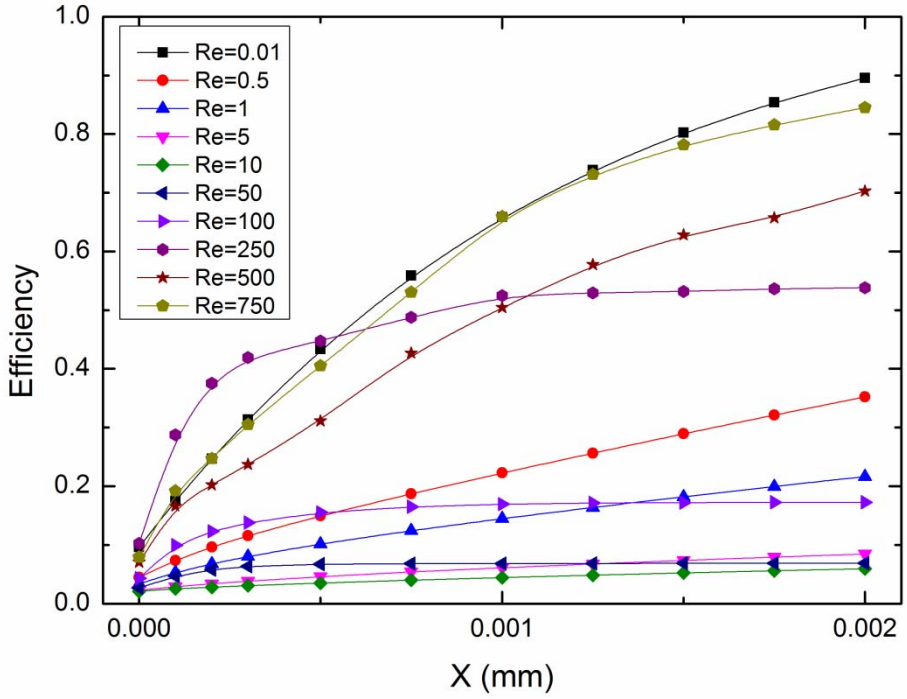

Fig. 3.5 Mixing efficiency against the length of mixing channel (laminar simulation)

In Fig. 3.5, the mixing efficiency against the length of mixing channel, X, is shown. It clearly reflects the behaviours of flow described above. The beginning of mixing is denoted as 0 where the flow enters the mixing channel and only the first 2000 um of mixing channel is displayed. Note that as the Reynolds number exceeds 500, the steady state of flow no longer exists and the transient flow modelling is adapted for simulating the periodic or

fluctuating flow behaviours in the mixing channel. Therefore, the results for Reynolds number 500 and 750 shown in Fig. 3.5 have been time-averaged. In this chapter, all the results obtained by transient simulation has been averaged by numerous instantaneous results of simulations in order to present the expecting value of mixing efficiency obtained from unsteady flow structures.

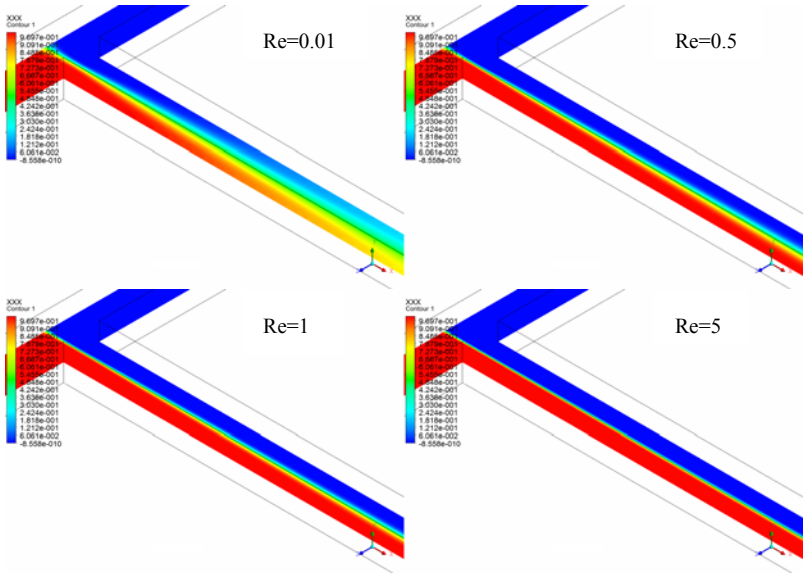

Fig. 3.6 Overview on the fluids mixing along the mixing channel from Reynolds number 0.01 to 5 (laminar flow model)

In Fig. 3.6 the fluids mixing from Reynolds number 0.01 to 5 with the view of cross-sections parallel to mixing channel is shown. The red and blue colours represent 1 (with the dye) and 0 (without the dye), respectively. As the colour is turned into green (i.e. 50:50), representing an evenly mixture[14].

[14] i.e. The dye has been evenly spread into the fluid that originally had no dye.

Figure 3.6 indicates that the mixing quality is very high for the case of Reynolds number 0.01 and is low for the rest of cases because the mixing here only relies on molecular diffusion as discussed before.

In Fig. 3.7 the streamlines of flow in the micromixer from Reynolds number 0.01 to 5 are shown. Under this flow regime, all the streamlines simply stays as straight laminar flow in the mixing channel without any vortex structure. The fluids flow through the mixing channel symmetrically even without any entanglements of streamlines. Therefore to design this type of micromixer, designers should focus on reducing the striation thickness of fluids, i.e. increasing the contact area between fluids by various measures.

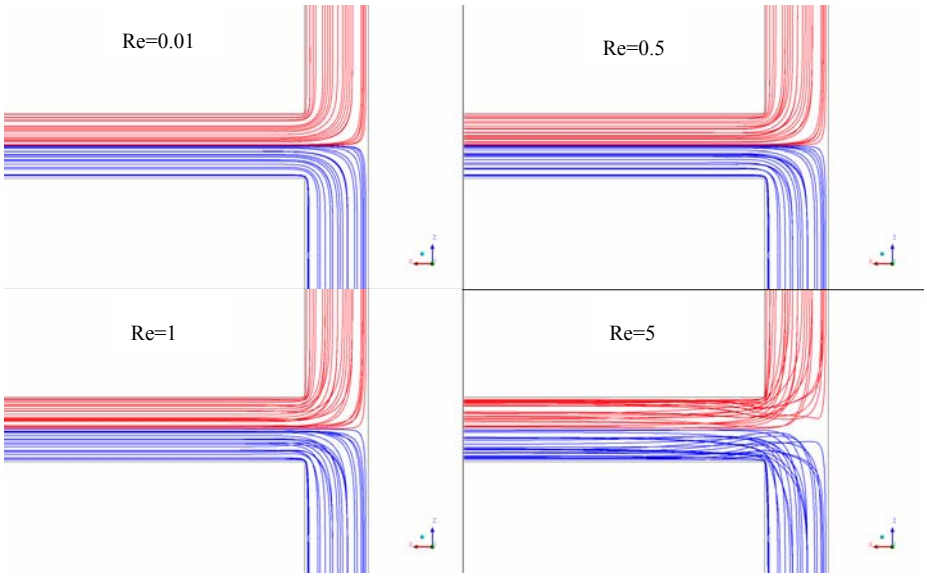

Fig. 3.7 Overview on the streamlines of flow along the mixing channel from Reynolds number 0.01 to 5 (laminar flow model)

In Figs. 3.8 and 3.9, the fluids mixing from Reynolds number 100 to 750 with the views of cross-sections that are parallel and perpendicular to mixing channel is shown, respectively. Note that for the cases of Reynolds number 500 and 750, the transient results are displayed.

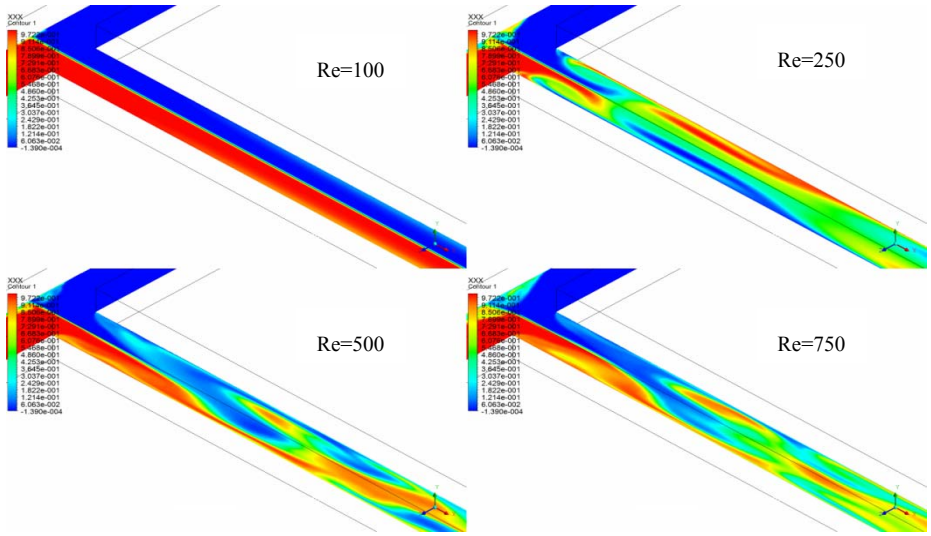

Fig. 3.8 Overview on the fluids mixing with the view of cross-sections parallel to mixing channel from Reynolds number 100 to 750 (laminar flow model)

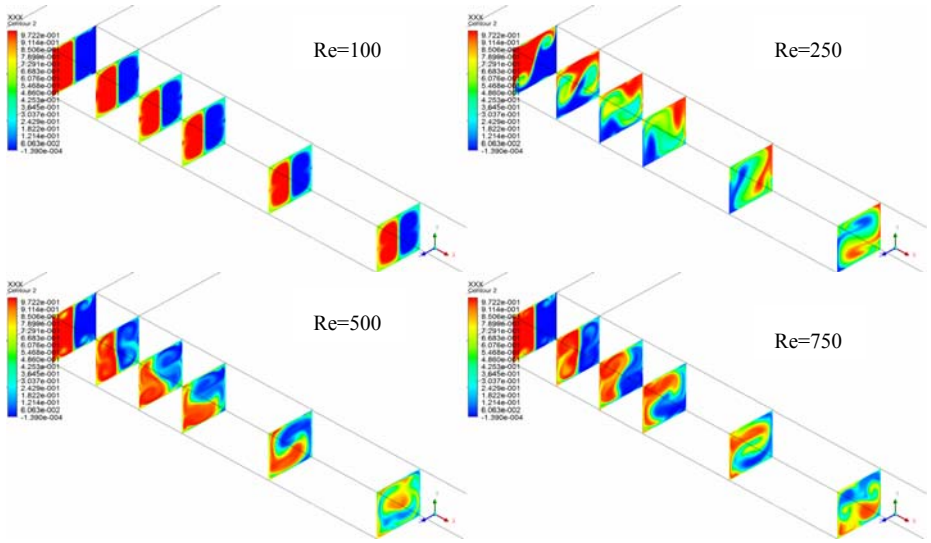

Fig. 3.9 Overview on the fluids mixing with the view of cross-sections perpendicular to mixing channel from Reynolds number 100 to 750 (laminar flow model)

As the Reynolds number is increased, the vortices generated by the convection of flow further enhance the mixing quality of fluids. One thing worth noting is that the mixing quality for Reynolds number 250 goes up quickly within a very short distance as shown in Fig. 3.5. This is because the roll-up vortices induced by the convection of flow happens at the interface of fluids as shown in Fig. 3.9, greatly enhancing the mixing. This indicates that an ideal flow structure could be generated through the convection mechanism even in the laminar flow to plays a significant role for promoting mixing.

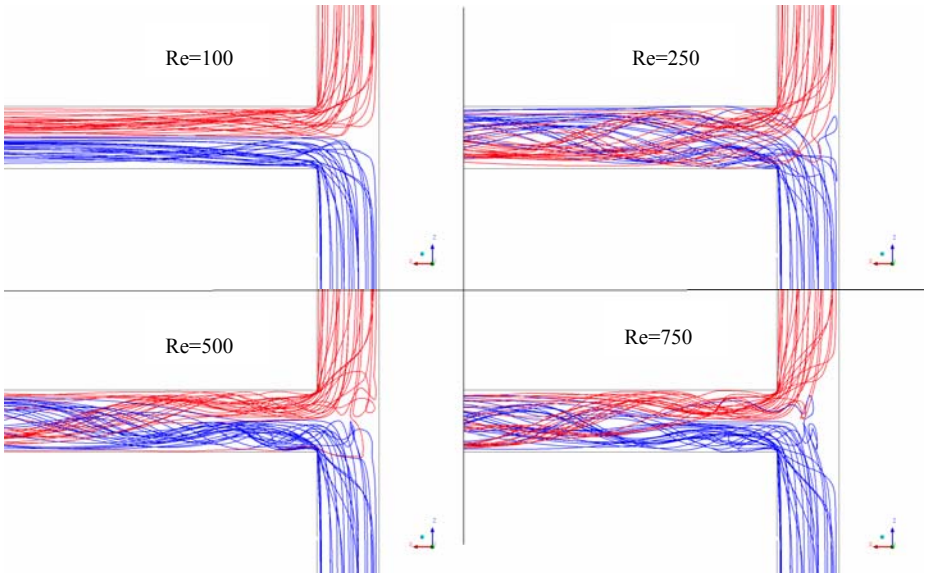

Fig. 3.10 Overview on the streamlines of flow along the mixing channel from Reynolds number 100 to 750 (laminar flow model)

In Fig. 3.10, the streamlines of flow from Reynolds number 100 to 750 are shown. It illustrates that the vortices has been generated for the flow of

Reynolds number 100. however, the vortices remain aside its own fluid instead of interplaying with each other. For the rest cases, the interplay of vortices created by convection produces the intricate entanglement of streamlines.

In Fig 3.11, the streamlines of flow from Reynolds number 100 to 750 viewed from the entrance to exit of mixing channel clearly illustrates the evolution and complexity of streamlines entanglement.

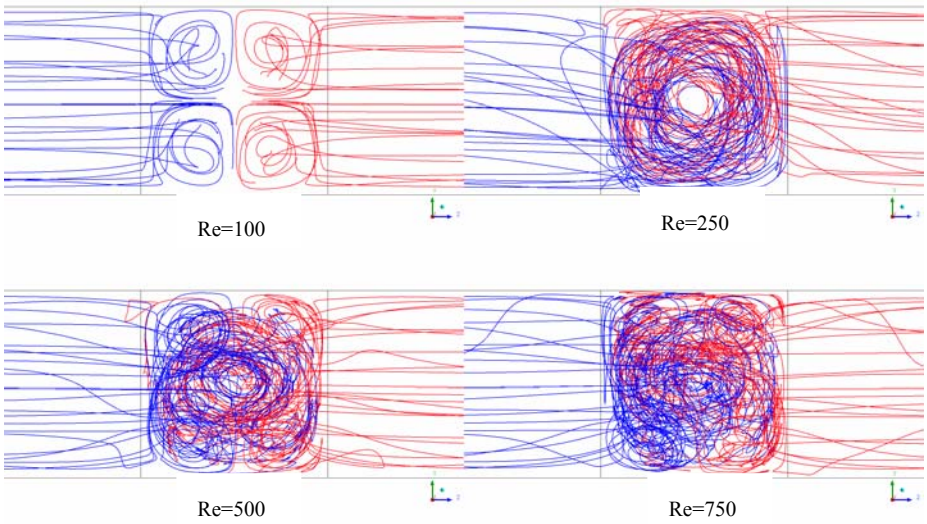

Fig. 3.11 The streamlines of flow viewed from the entrance to exit of mixing channel (laminar flow model)

Recent progress on the continuous-flow micromixer as introduced in the first chapter has shown that there is no upper limit of Reynolds number for such a

micromixer. As the critical Reynolds number for turbulence transition is exceeded, the onset of turbulent flow is triggered and turbulence structure is to be developed. The mixing mechanisms of micromixer in such flow conditions are dominated by molecular diffusion, flow convection and turbulent diffusion. For these mixing flows in micromixer, simulations by using Reynolds-averaged Navier-Stokes turbulence modelling was not possible until this approach presented in this thesis by using LCTM coupled with convection-diffusion equation. Now let us further discuss the contour of flow mixings obtained by this numerical approach firstly investigated by this PhD programme for turbulence micro-mixers.

In Fig 3.12, the mixing quality of micromixer against Reynolds number at distance of 2000 um is shown. All the results from Reynolds number 100 to 1800 is transiently simulated by using LCTM and time-averaged. The mixing quality increases quickly as the Reynolds number increase from 100 to 750. Beyond the Reynolds number 750, the mixing quality remains virtually steady until Reynolds number 1800. Nevertheless, with the higher Reynolds number, i.e. the higher in-flow velocity, the micromixer will achieve higher

mixing quality during a much shorter time.

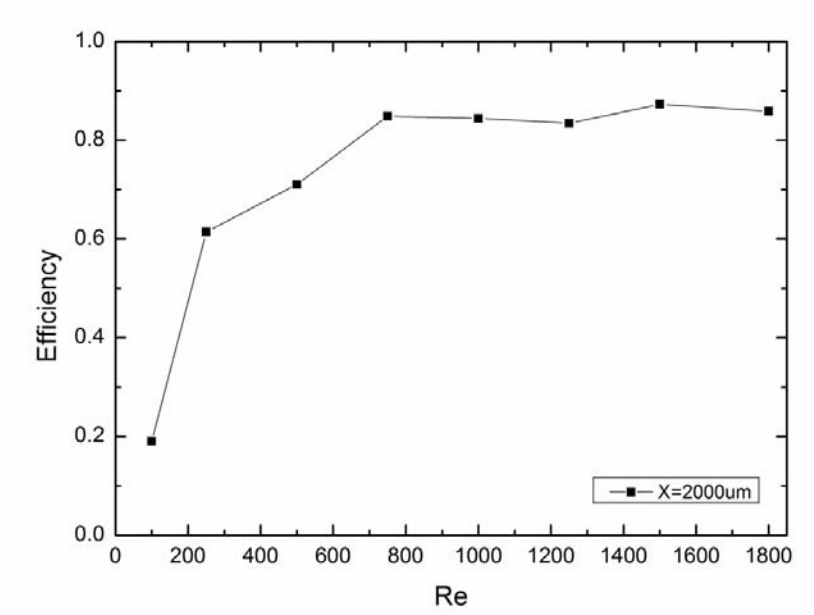

Fig. 3.12 The mixing efficiency against Reynolds number (LCTM)

In Fig. 3.13, the mixing quality of micromixer simulated by using LCTM against mixing channel is shown.

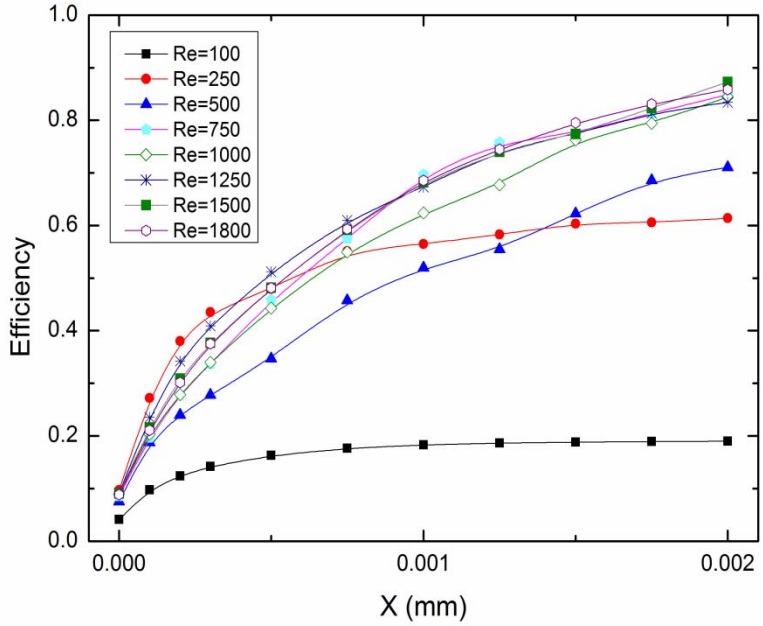

Fig. 3.13 The mixing efficiency against mixing channel (LCTM)

In general, the mixing completes quicker with increased Reynolds numbers. For the cases of Reynolds number exceeding 750, the mixing quality over the distance of 2000 um remains more or less the similar rate. As the result of laminar simulation (Fig. 3.5), the flow of Reynolds number 250 obtained from LCTM (Fig. 3.13) also shows a rapid increasing on the mixing quality over a very short distance. Now, let us compare the results by laminar flow model and LCTM alongside as shown in Fig. 3.14. The results for Reynolds numbers of 100, 250, 500, 750 where they show discrepancies are compared at 2000 um against Reynolds number. The discrepancies are marginal except for the maximum 12.3% at Reynolds number 250.

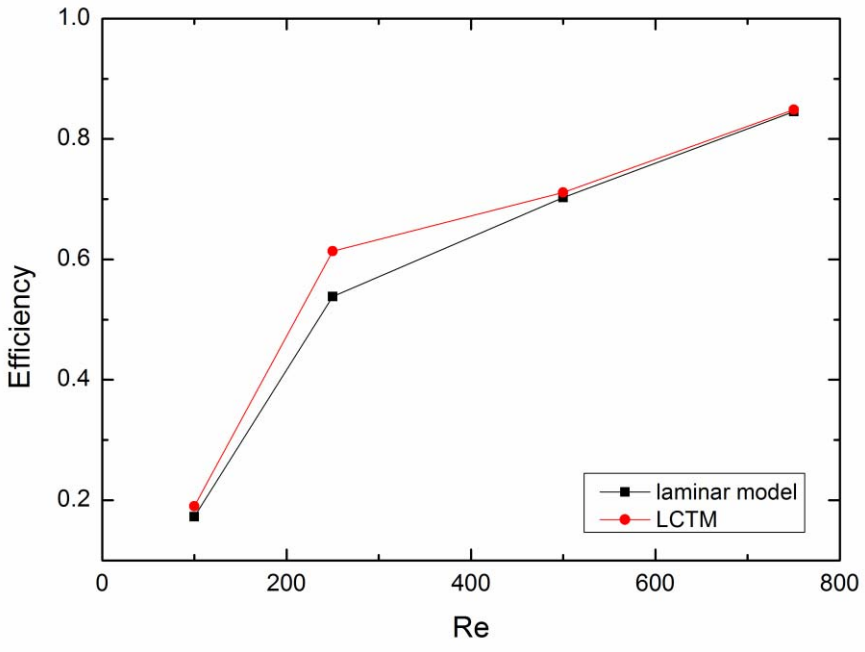

Fig. 3.14 Comparison on mixing efficiency calculated by both models against Re

The mixing qualities against X obtained from these two models is also investigated as shown in Fig. 3.15. These two curves start to deviate from Reynolds number 100 reaching a maximum of 12.3% at Reynolds number 250.

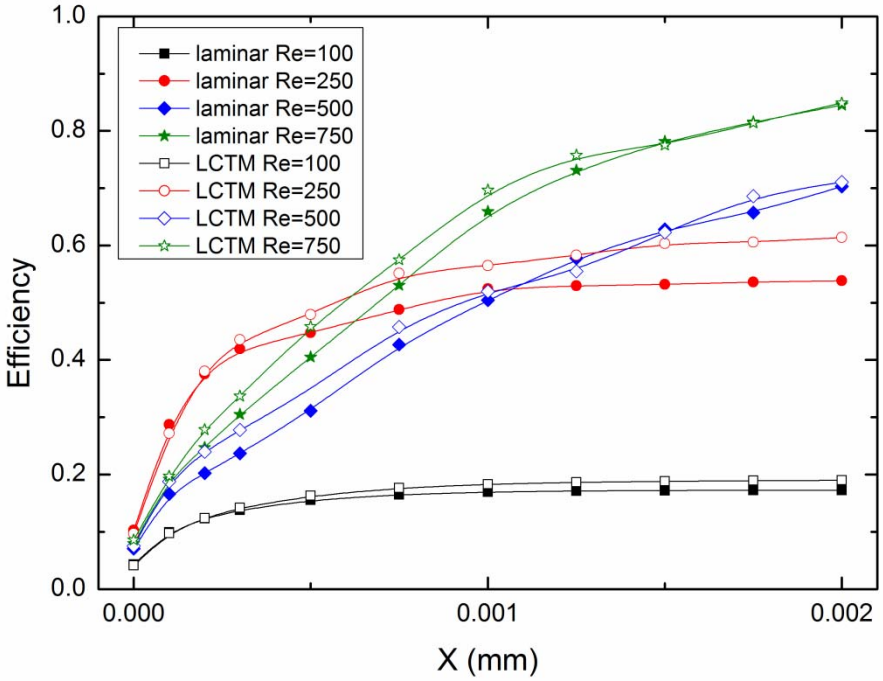

Fig. 3.15 Comparison on mixing efficiencies calculated by both models against mixing channel

Although the discrepancies seem not to be small enough from the view of quantitative prediction despite of the fact that it is acceptable for the qualitative analysis. However, this validation on mixing efficiency is performed in the transition-turbulent flow regime, currently there are no available data from either experiments or numerical simulations for an

appropriated and quantitative comparison. And it is difficult to sat which model caused the discrepancy, though the LCTM approach is more rational. Therefore, future experimental validation is essential. Nevertheless, these simulated results are still valuable for qualitative discussion, providing guidelines for designing the micromixer for the rapid mixing applications.

Now let us further discuss the LCTM contour of flow mixing in comparison with those of laminar model (referring to Fig. 3.8). In Fig. 3.16, LCTM contours are shown along the mixing channel for Reynolds number 100 to 750. For Reynolds number 100 and 250, the contour patterns from both models are highly resemble.

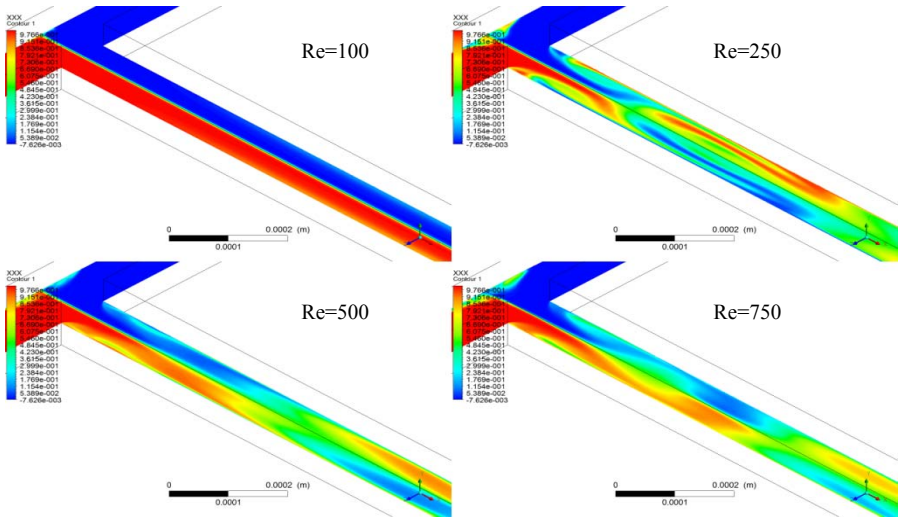

Fig. 3.16 Overview on the fluids mixing along the mixing channel from Reynolds number 100 to 750 (LCTM)

Note that for Reynolds number 500 and 750 the flow structures shown in both models are the instantaneous results which are not necessarily similar.

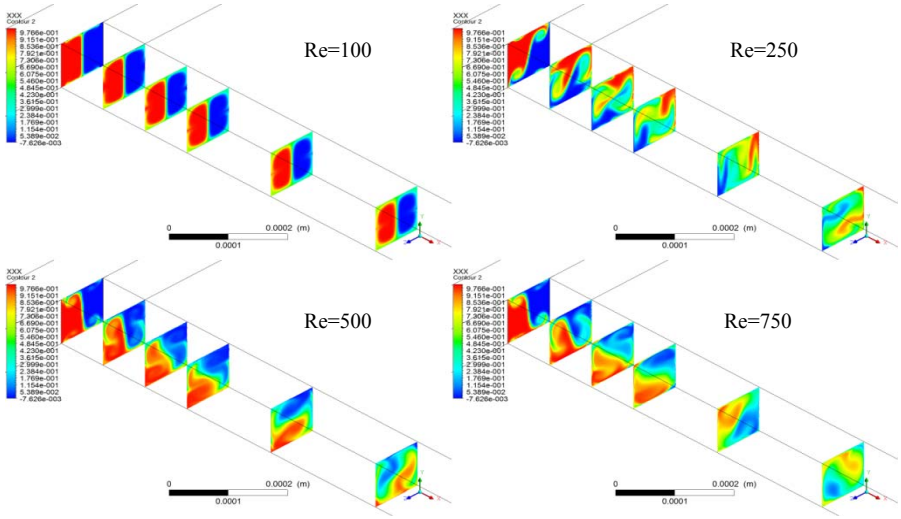

Fig. 3.17 Overview on the fluids mixing with the view of cross-sections perpendicular to mixing channel from Reynolds number 100 to 750 (LCTM)

In Fig. 3.17, these contours are viewed on cross-sections perpendicular to mixing channel. Again the first two case for Reynolds number of 100 and 250 displays the highly similar patterns.

When the Reynolds number (based on the inlet velocity) exceeds 1000, the onset of turbulence in the mixing channel is triggered, referring to chapter 2. The flow in the mixing channel enters the regime transition-turbulence flow. In Figs. 3.18 and 3.19, the contours for Reynolds number 1000 to 1800 are shown in the views of cross-sections that are parallel and perpendicular to

mixing channel, respectively.

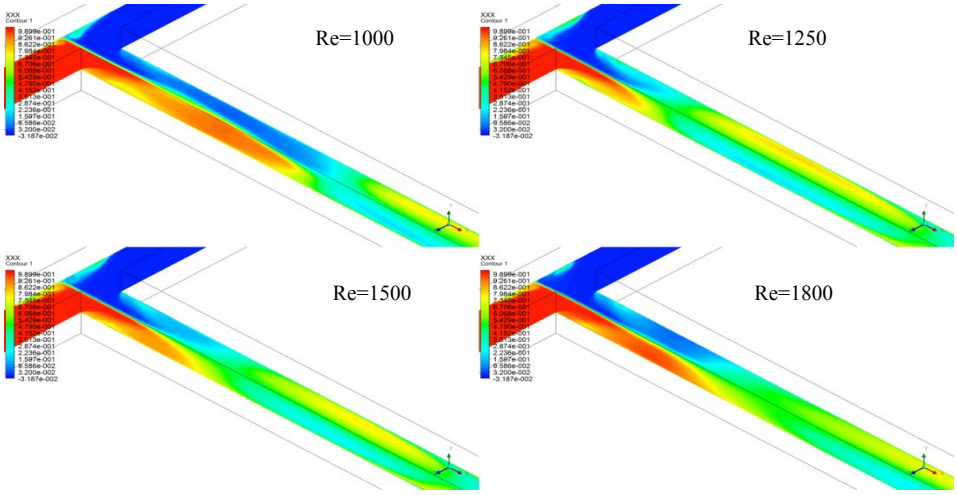

Fig. 3.18 Overview on the fluids mixing along the mixing channel from Reynolds number 1000 to 1800 (LCTM)

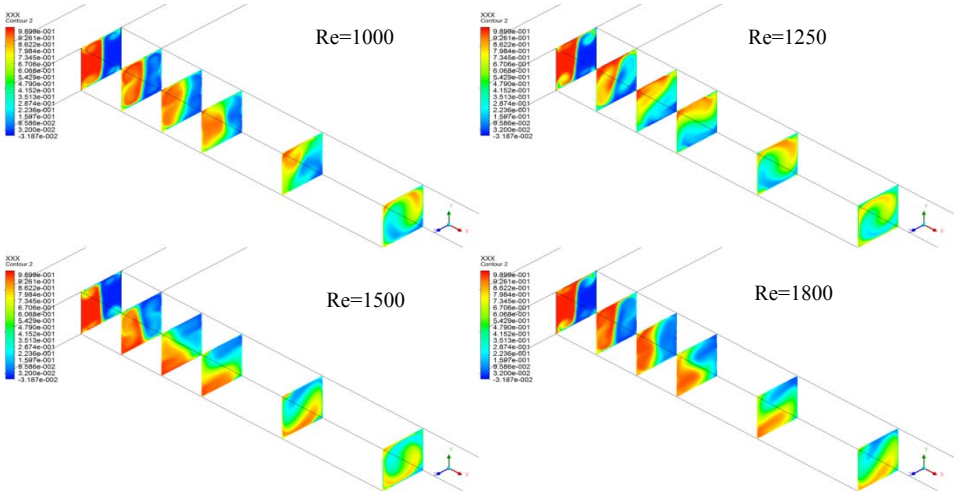

Fig. 3.19 Overview on the fluids mixing with the view of cross-sections perpendicular to mixing channel from Reynolds number 1000 to 1800 (LCTM)

These contours show clearly how the mixing quality being affected and confined by the geometric structure of micromixer. For example, as shown in Fig. 3.19, the mixing quality for the case of Reynolds number 1250 is clearly

promoted by the development of vortices close to the fluids interface that is similar for the case of Reynolds number 250. This results in a higher mixing quality in the beginning of mixing as shown in Fig. 3.13. This example demonstrates that the convection of flow that induces the development of vortices and consequently promotes the mixing is essential even for the flow with turbulent diffusion. In other words, in order to perform a good mixing in a very short time, not only the turbulent mixing is required but also the convection of flow needs to be firstly considered appropriately for reducing the striation thickness of flow by creating vortices at right position and right time with proper size. This strategy of mixing we demonstrated here numerically was observed firstly experimentally by (Majumdar, Sutin et al. 2005) and Matsumoto et al. (Matsumoto, Yane et al. 2007).

3.5 **Summary**

In this chapter, the LCTM turbulence model adapted for the micro-channel simulation in the previous chapter is coupled with scalar dispersion for investigating the numerical simulation of micromixer. The numerical results calculated by this LCTM approach show good agreement qualitatively with

those laminar flow model even in the laminar flow regime. Therefore, after further work on the validations with experimental data is done in the future, it could be used as a general numerical approach for those micro-mixers in which the flow across entire flow regimes from the very low Reynolds number of straight laminar flow through highly intermittent transition-turbulence to fully turbulent flow.

The numerical results show that the high in-flow velocity is essential for achieving good mixing in a very short time. The creation of vortices close to the interface of fluids has significant influence on mixing quality, even for turbulent mixing. The mechanism of rapid mixing in the micromixer relies on an appropriate combination of molecular diffusion, flow convection and turbulent diffusion. To achieve a good mixing , this requires a micromixer utilizing these three elements appropriately in a concert way through its properly configurated structure.

Chapter 4

Laser-induced Cavitation Bubbles in the Micro-scale

4.1 Introduction

Cavitation is a phenomenon that describes the rapid appearance of vapour cavity inside the liquid medium and its subsequent violent implosion. This phenomenon was originally discovered by Barnaby and Parsons in 1893 on investigating the propeller failure of a new British destroyer (H.M.S. Daring). The term 'cavitation' suggested by R. E. Froude was cited for the first time by Barnaby and Thornycroft (Barnaby and Thornycroft 1895) and in their paper they concluded the insufficient thrust of propellers are resulted from the formation of voids and clouds of bubbles where the pressure near the blade fell a negative value (tension) of about a half of an atmosphere. For more information on the discovery of cavitation, please see the review in e.g. (Li 2000). Since then, this phenomenon that is induced nearby the propellers

of ship or hydro-turbine has been referred as the hydrodynamic cavitation. For almost a century, it was mainly concerned by the professionals in the industries of marine and hydraulic machinery. Its violent collapse toward the wall boundary often accompanies with high-speed impinging jet that causes the damage on the propellers and the deterioration on the machine system. Therefore, for a long time, cavitation was almost always treated as an unwanted phenomenon to be avoided in those engineering practice. Recently, with the discovery of favourite effects of cavitation, this phenomenon has been widely studied across many disciplines with various applications such as utilising cavitation for the gene and drug delivery, non-invasive surgery[15] and therapy, and the surface cleaning and water treatment (Ohl, Arora et al. 2006, Coussios and Roy 2008, Gogate and Kabadi 2009). The cavitation has now become as a powerful tool for scientific researches and industrial applications. The attitude towards cavitation has now been drastically changed in order to facilitate and exploit the new use of this phenomenon. Based on the physical mechanism of how the cavitation is generated,

[15] E.g. the non-invasive destruction of human stones by Warwick cavitation group (Li, S. and Billson, D. (2011). EPSRC WIMRC Final Report, University of Warwick.

cavitation can be classified into two main categories (Lauterborn 1979): cavitation brought by the tension in the liquid and by the energy deposit, as illustrated in Fig. 4.1.

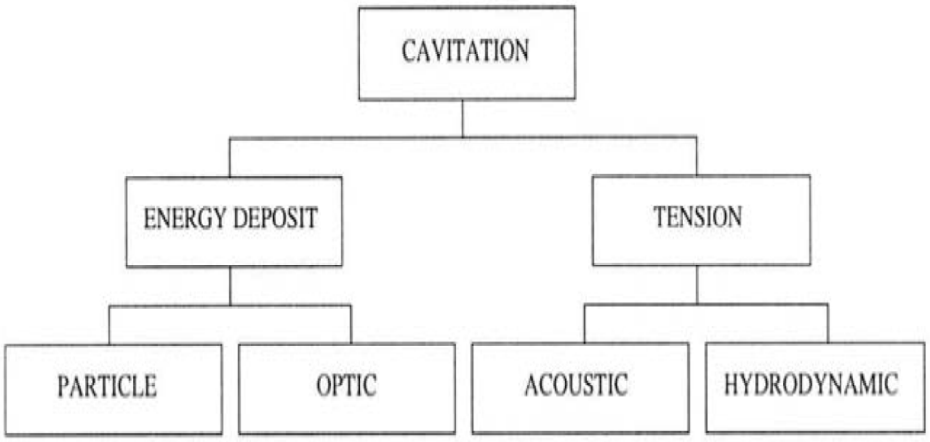

Fig. 4.1 The classification of Cavitations (Lauterborn 1979)

In the first category, the hydrodynamic cavitation and acoustic cavitation are due to the rapid reduction of local pressure in the liquid where the negative pressure (i.e. tension) is observed. The hydrodynamic cavitation is mainly observed in the place where the rapid change of pressure drop is caused either by the constraint of geometric structure or high-speed flow.

Here, a cavitation number (index) σ is introduced by using the concise description given by Acosta in e.g. (Li 2000) for characterizing this type of

cavitation.

$$\sigma = \frac{p_\infty - p_v}{\frac{1}{2}\rho U_\infty^{\,2}} \tag{4.1}$$

where p_∞ is a static reference pressure of fluid, p_v is the equilibrium vapour pressure of the pure liquid medium, U_∞ is the reference velocity, and ρ is the density of fluid. For the vaporous cavitation to occur $p_{\min} < p_v$ where $p_{\min}$ is the minimum pressure in the fluid. When the inception of cavitation occurs, the value σ is called cavitation inception number, σ_i. As the pressure is known (or computed) within the flow or on the wetted surface, it can be made in a dimensionless pressure coefficient c_p where $c_p = p - p_\infty \Big/ \frac{1}{2}\rho U_\infty^{\,2}$. Herein, the condition of vaporous cavitation inception is written as

$$\sigma_i < -c_{p\min} \tag{4.2}$$

The cavitation inception can be attained either by decreasing the reference pressure or increasing the flow velocity. The cavitation number can be rewritten in alternative form as

$$\sigma = \frac{p_\infty - p_v(T)}{\Delta p} \tag{4.3}$$

where Δp is the pressure difference that characterizes the system and ambient environment such as the difference between upstream and downstream pressure $p_{upstream} - p_{downstream}$ in the gate.

As for the acoustic cavitation, it is induced by acoustic waves, e.g. by a curved transducer to generate High Intensity Focused Ultrasound (HIFU). The HIFU can locally produce heat for the tissue ablation as well as shockwave for the lithotripsy but it produces more intense heating and higher pressure if the acoustically induced cavitation bubbles present there. Although HIFU has been widely used in the medical researches, the ultrasound therapies utilizing acoustic cavitation are just emerging in very limited scale.

In the category of energy deposit, this type of cavitation is generated by depositing very high intensity of energy into a tiny space where the threshold of optical breakdown in the liquid is exceeded. Following the optical breakdown where the plasma formatted, a vapour bubble appears, grows and

then collapses in a very short time scale. It is usually induced by focusing a high-intensity pulsed laser beam to achieve this optical breakdown. It is thus termed as laser-induced bubble.

The early experimental works in the laser-induced cavitation bubble are those without the boundary[16], e.g. (Felix and Ellis 1971, Lauterborn 1972), and with the boundary[17] , e.g. (Lauterborn and Bolle 1975). Using this technique, a single and spherical cavitation bubble can be achieved for the first time to be compared with the theoretical analysis (Plesset and Chapman 1971). Due to its easy manipulation and high reproducibility, this technique has been used extensively for characterizing various behaviours of single cavitation bubble such as bubble-wall interaction and bubble-bubble interaction etc. The experimental works on bubbles interacting with the nearby wall (Vogel, Lauterborn et al. 1989, Philipp and Lauterborn 1998, Lindau and Lauterborn 2003) revealed various physical processes of bubbles contributing to a fuller understanding of cavitation damage and erosion. By setting up two

[16] The cavitation bubble is produced in the free space.

[17] The cavitation bubble is produced in the asymmetric environment such as at a near-by wall boundary.

laser-induced cavitation bubbles close to each other or to a wall boundary, their dynamics can be explored further through experimental observations in a controllable environment (Lauterborn and Hentschel 1985, Blake, Robinson et al. 1993). The mechanics of bubble-bubble interaction is essential to the understanding of the collective bubbles since the cavitation in the natural world is mostly multi-bubble phenomenon. For a comprehensive review on the physics of cavitation bubble, readers are referred to e.g. (Werner Lauterborn and Thomas 2010).

Although the behaviours of vapour bubble are not the same as those generated by laser[18], laser-induced cavitation bubble plus high speed photography has become a powerful tool that allows us to conduct experiments investigating on the dynamics of cavitation bubble, which otherwise would not be possible. However, these experiments were mainly of the conventional system in the macro scale, i.e. above 1 mm. Recent progress in the microfluidics has intrigued the study of cavitation bubble in the

[18] During its growth phase the bubbles generated by laser behave differently from the vapour bubble; nevertheless during its collapse phase they behave the same.

microscale (Zwaan, Le Gac et al. 2007, Quinto-Su, Lim et al. 2009, Quinto-Su and Ohl 2009). Many novel applications by making use of the laser-induced cavitation bubble in the microfluidics have been proposed such as the transport of micro-particles (Ohl, Arora et al. 2006, Lautz, Sankin et al. 2010), high-speed fluid switch (Wu, Gao et al. 2008), mixing of fluids (Hellman, Rau et al. 2007), cell poration (Gac, Zwaan et al. 2007) , cell lysis (Quinto-Su, Lai et al. 2008) and generation of complex flow pattern (Quinto-Su, Venugopalan et al. 2008, Lim, Quinto-Su et al. 2010). All these studies mentioned above have demonstrated a great potential of laser-induced cavitation in the microscale for the technology development across various disciplines and industrial applications. However, the knowledge of microscale cavitation and its effects to the microscale device is unknown yet. Therefore, it is essential to study the dynamics of micro-scale bubble cavitation.

In this thesis the dynamics of cavitation bubble is mainly studied by the high-speed photography. The advance in the ultra high speed camera has made the dynamic study of micro-scale cavitation bubble possible due to its

high temporal resolution. The evolution of cavitation bubbles in microscale that normally only has a lifetime of a few tens microseconds is recorded by an ultra high speed camera that can produce one hundred frames of video at one go. This capacity of producing a high speed images has facilitated the investigation of bubble dynamics. However, another problem arises from using this technique, i.e. the data analysis of enormous bubble images. In order to analyse the subtle effects of micro-scale bubble such as the influence of surface tension and viscosity, the experimental conditions and parameters are controlled strictly and accurately with enormous number of bubble images to be recorded and analysed. The analysis of these bubble images has been a very tedious and impractical job if not mention to be analysed quantitatively[19]. Moreover, the subtle change of bubble within a series of recorded images is quite often too difficult to be perceived and measured by human's eye and hand, especially for the microscale bubbles. Therefore, a quantitatively computer-aided automatic analysis is highly demanded. Recent

[19] For example, one run of an experiment of 1000 high-speed videos of which each video contains 100 frames may result in total of one hundred thousands of images to be analysed. If one frame needs 1 minute to analyse, the total would require 69 days by working round the clock to complete.

advance in image segmentation offers a possible solution to resolve this problem. In this thesis, a new approach of self-adjusting and semi-automatic active contour for detecting and digitizing the contours of micro-bubble image has been developed based on the available concept and methods for active contour detection used in other field such as medical imaging and computer vision, etc. The detailed technique of this newly developed method will be introduced in the next chapter.

As the first step of the whole joint project, during the time of my PhD period, I have designed and built up an experimental facility of laser-induced cavitation micro-bubbles under the support of Prof. Shengcai Li. This experimental setup will serve as a research platform for advanced studies on the erosion of microscale cavitation and cavitation bubbles in the microchannel and microfluidic device in the future. The current experimental setup and some trial results[20] will be discussed in the following sections.

[20] Mainly for the verification and calibration of the experiment facility and for the trial run of the newly developed active contour detection code.

4.2 Experimental Setup

The cavitation bubble is generated by focusing a Q-switch Nd-Yag laser beam (Litron Laser Nano TRL 850G-10) into a test cuvette filled by de-ion water. The pulsed laser, 11 mm in the diameter of beam, has a maximum energy of 800 mj at a wavelength of 1064 nm with a repetition rate of 10 hertz. The laser head adopted a design of bolt-on modules for the customized application as shown in Fig. 4.2. With a second harmonic generator equipped with our laser system, the frequency doubled laser beam, used for this experiment, emits at a wavelength of 532 nm with a maximum energy of 450 mj and a pulse width of 8 ns. An optical attenuator is also fitted onto the laser head to allow the energy output to be manually adjusted.

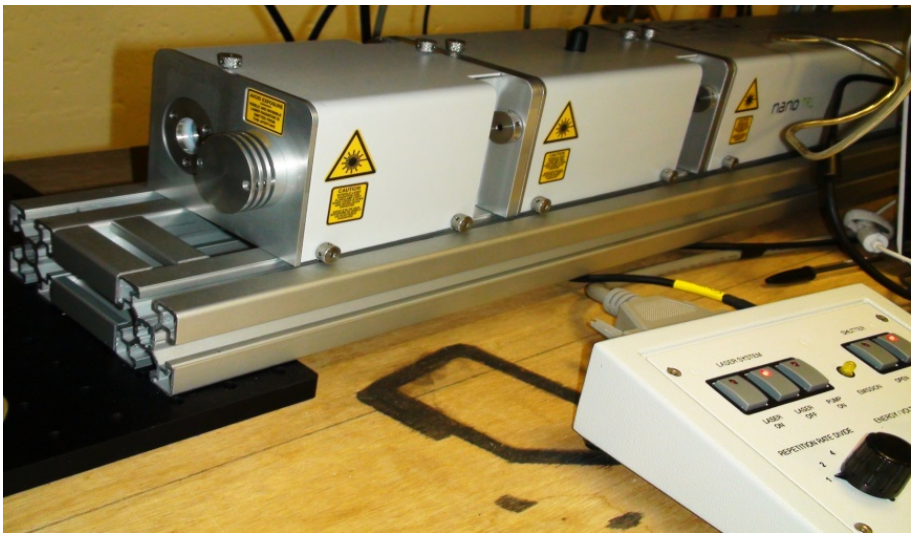

Fig. 4.2 Modular laser head and control panel

In order to achieve a diffraction-limited, or so-called aberration-free, spot a microscope objective with 0.25 numerical aperture and 15mm working distance is employed as the focusing optics for achieving an extremely high energy concentration at a focusing spot of 1.3 um. The use of this compact microscope objective increases the reproducibility of a single bubble owing to a more reliable alignment of focusing lens. A 50 : 50 beam splitter is aligned at 45 degree in the middle of optical path between the focusing objective and the laser head. This allows us to monitor the laser energy of every single firing while simultaneously creating the required bubble by the subsequent focusing laser. The laser energy is measured by a pyroelectric energy sensors connected with an energy meter.

The cuvette is made of Perspex glass, Polymethylmethacrylate (PMMA). On the front panel of cuvette where the laser is incident perpendicularly, a Fused Silica laser window of 1 inch diameter with high damage threshold specific for Nd-Yag laser is installed as the incident window of laser. The optical path for generating the cavitation bubble in this experiment is in the following sequences: 1. Laser beam firing, 2. Laser beam passing through the beam

splitter, 3. Focusing laser beam through the microscope objective, 4. Laser beam passing through the laser window into cuvette, 5. Laser energy deposit at the focal point, generating the required cavitation bubble.

The life time of cavitation bubbles during their first cycle of collapse typically varies from a few dozens of microseconds to several hundreds of microseconds subject to the maximum radius of bubble ranging from a few hundreds of micrometers to several thousands of micrometers, respectively. Therefore, the requirements for the instruments and detection methods are very high in terms of their spatial and temporal resolutions. That is, much finer spatial and temporal resolutions in comparison with those used for conventional cavitation experiments are demanded in order to capture the images of these tiny and swift bubbles.

The dynamic images of cavitation bubble are recorded by a high speed camera, Shimadzu HPV-1, with a backlight illumination of a 150 watt continuous Metal-halide light source. This Shimadzu HPV-1 has the capability of ultra high speed video recording for 100 frames at one go with

the resolution of 312 by 260 pixels at maximum of 1 million frame rate. The camera has a function of direct video output allowing the preview of images, making the adjustment of focus and aperture of lens much easier.

Fig. 4.3 High speed video camera with K2 long distance microscope

The evolution of bubble is visualized by shadowgraph technique that the backlighted bubble casts a sharp shadow onto the lens of high speed camera. The image variation of bubble shadow is thus recorded by the camera in a time sequence. Shadowgraph is a fundamental and powerful flow visualization method and is based on the property of light, which travels straight in a homogeneously uniform medium, characteristized by its index of refraction. Once the bubble appears in the water, the density difference

between gas and liquid causes the change of refraction index. The luminance in the medium is thus redistributed because partial rays of backlighting are bent, refracted, and reflected. The resultant shadow image of the bubble is thus formed, casting onto the recording device.

For achieving a high spatial resolution of bubble image, a long distance microscope (Infinity K2/SC) with close-focus objective (CF-1/B) and magnification amplifiers (CF tube 1.66X and TX tube 2.0X), as shown in Fig. 4.3, is configured and integrated with the high speed camera. This setup at a working distance of 222 mm gives a total of 7 times magnification on the sample being observed.

A notch Filter with a central stop-band wavelength of 533 nm is placed between the camera and the cavitation chamber to filter out the bright light of laser. This allows us to observe the interaction between the focusing laser and material, in this case the de-ion water, including the resultant plasma and the accompanying cavitation bubble.

The time synchronization of the laser and the camera is essential for capturing the evolution of cavitation bubble due to its extremely fast variation in temporal domain. This is achieved by utilising a oscilloscope to monitor the time delay between the signals of laser firing and camera triggering, and then set the delay in the camera accordingly to catch the appearance of the bubble throughout its life cycle.

4.3 General Description of Laser-induced Cavitation Bubble

As a focusing laser beam enters into a liquid medium in our case, the deposit of high-intensity laser energy at the focal point induces the optical breakdown of the liquid, causing the plasma formation and the appearance of cavitation bubble together with the shock wave irradiation. This process is broadly divided into two stages in sequence: the stage of bubble formation and its growth and the stage of bubble deformation and its collapse. General description of this process is that as the plasma accompanying with high temperature and pressure is formed in a hot spot, a tiny cavity is induced by the liquid breakdown and expanded through the energy exchange. The

pressure force is then conversed into the potential energy of cavitation bubble that results in a rapid growth of bubble and the balance achieved at the maximum of bubble radius. Following this energy balance the local pressure of ambient environment come into force that triggers the subsequent violently rapid collapse of this cavitation bubble. The potential energy is then conversed to the inertial force of bubble accompanying with an increasing bubble-wall velocity and the internal pressure as the volume of bubble is being compressed. At the collapsing point, the extremely high pressure might subsequently trigger another cycle of growth and collapse, often named as rebound.

The behaviour of laser-induced cavitation bubble can be further divided into spherical and non-spherical cavitation bubbles subject to the environment the bubble encounters. The spherical cavitation bubble generally appears in free space, i.e. symmetric environment; the non-spherical cavitation bubble often appears close to a nearby wall boundary, i.e. asymmetric environment. As a cavitation bubble is generated in an asymmetric environment, during its collapsing phase, the bubble evolves dynamically towards the wall boundary

with its geometric features such as shape and volume varying rapidly. These variations can be used to characterize the dynamics of cavitation bubble. Therefore, the possibility[21] of using active contour method to delineate such fast varying geometric features of cavitation bubble quantitatively and automatically is essential for analysing the dynamics of cavitation bubble in such an environment. As shown in the next chapter, the affine snake with EGVF field offers a promising approach to tackle this problem and a consistent protocol based on physical mechanism for detecting the contour of cavitation bubble obtained from the experiment. Furthermore, the parametric contour obtained by using the active contour method helps to construct parameters of cavitation bubble during various phases and the corresponding geometric models. These quantified finding can further facilitate the comparison of experimental data with numerical data obtained from theoretical calculations thus to advance our understandings of micro-bubble dynamics. In order to apply the active contour method to our case, an self-adjusting and automatic approach has been developed in this PhD

[21] Active contour method has never been applied in the analysis of cavitation bubble images until this study.

programme based on the currently available concept and work used in other fields.

4.4 Discussion and Results of Spherical Cavitation Bubble

By using our newly developed active contour method, the discrete digitalized contour of cavitation bubble and geometric against time can be extracted from images. These geometric data of bubble is further used for calculating dynamic parameters of cavitation bubble, such as the velocity and acceleration of bubble that can be readily calculated based on the movement of geometric centre of bubble. The volume calculation of bubble can be performed by using the shell method for the solid of evolution with the assumption of bubble generally remaining axisymmetry. The change of internal temperature and pressure of cavitation bubble against time is subsequently obtained by assuming an adiabatic process during its first cycle of growth and collapse. This assumption is generally satisfactory and acceptable due to the rapid increasing and decreasing of the bubble pressure. Even for multi-bubble case, this ideally simplified assumption is still valid to a certain degree as demonstrated by the experimental measurement on the

multi-bubble sonoluminescence (McNamara, Didenko et al. 1999). According to the classical thermodynamics (Carter 2001), the relationship between pressure and volume for an adiabatic process in a ideal gas is given as

$$PV^{\gamma_c} = K \tag{4.4}$$

where the K is a constant of integration and γ_c is an adiabatic index that is a ratio of specific heat for constant pressure to specific heat for constant volume, i.e. heat capacity ratio.

Some typical cases of laser-induced cavitation bubbles are discussed here in the rest of chapter. Figure 4.4 is a series of images of spherical cavitation bubble with $R_m \approx$ 0.7033 mm. The sequence of frames taken by Shimadzu HPV-1 high speed camera is arranged from the left to the right and then from the top to the bottom. The time interval for the first 20 frames is 1 μs and for the rest is 2 μs. The cavitation bubble is induced by the optical breakdown, plasma, as shown in the first three images where the bright white light is observed. The cavitation bubble experiences a cycle of growth and collapse as shown in these images. To extract some characteristic data such as the max and min radii only from these images, people might be able to do it

manually; however, this will become completely impossible to manually extract geometrical information quantitatively from over hundred thousand of these images for thoroughly investigating the dynamics of such cavitation bubbles. By utilizing the active contour method developed through this PhD programme as demonstrated in the next chapter, this difficulty is resolved.

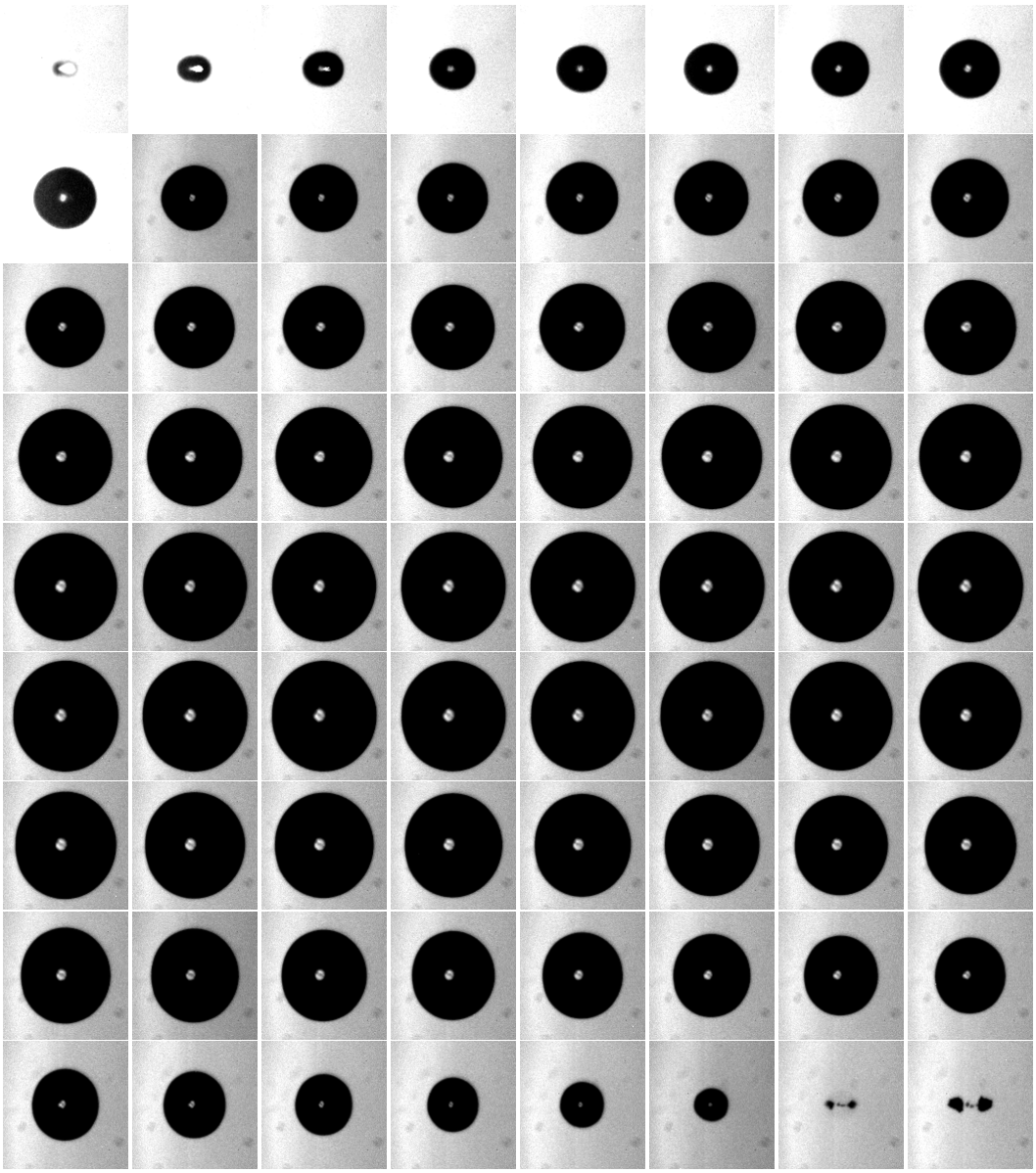

Fig. 4.4 The growth and collapse of spherical cavitation bubble with $R_m \approx$ 0.7033 mm

Figure 4.5 shows the complete contours detected from the images in Fig. 4.4 by using this method.

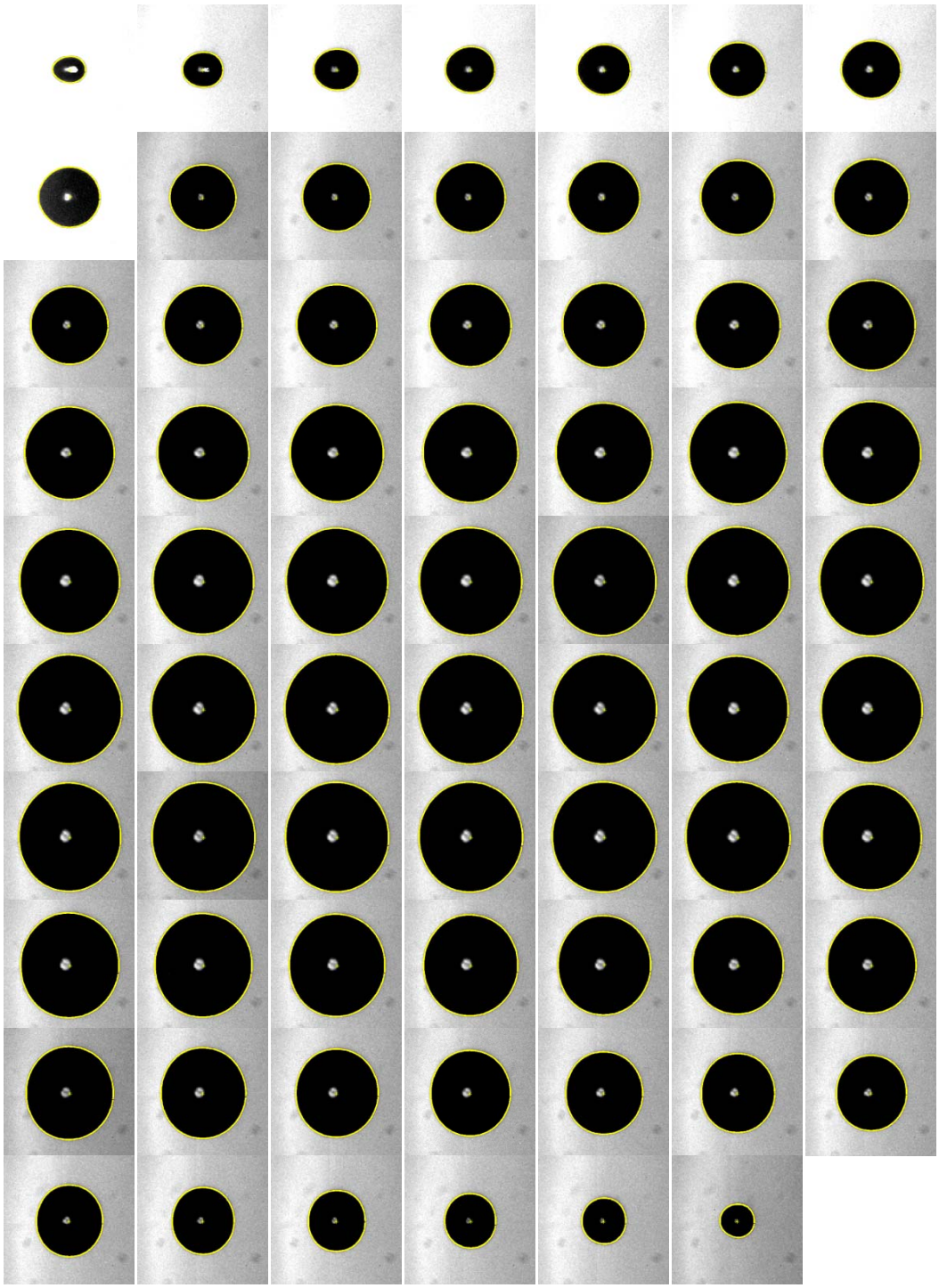

Fig. 4.5 The contour delineation of spherical cavitation bubble with $R_m \approx$ 0.7033 mm

The delineation of bubble contour is designated as the yellow line on the bubble contour. These contours are formed by a set of discrete points that are locked onto the edge of bubble as demonstrated in chapter 5. Note that the tracking of bubble contour starts from the second frame in the Fig. 4.4 since the first frame is of plasma. And the last two frames are not tracked since the single spherical bubble is collapsed into two splitting bubbles due to the high instability at the final stage of collapse.

Figure 4.6 shows a complete set of geometric data during the growth and collapse phases against time. All these geometric values are extracted and calculated from the detected bubble contours as shown in Fig. 4.5. These curves of various dynamic variables are thus reflecting the time history of cavitation bubble. In Figs. 4.6a and 4.6b, the x-coordinate and y-coordinate of centroid of bubble are plotted with respect to time. Both values have been translated by setting the centroid of bubble in the first frame as the origin. By doing this, the relative displacement of bubble centroid can be readily seen. Figure 4.6c is the time history of bubble volume from which the maximum

radius and the Rayleigh collapse time T_c[22] (Rayleight 1917) can be easily found. The Rayleigh collapse time for this case is 62 μs . The method used for estimating the bubble volume is shown in chapter 5.

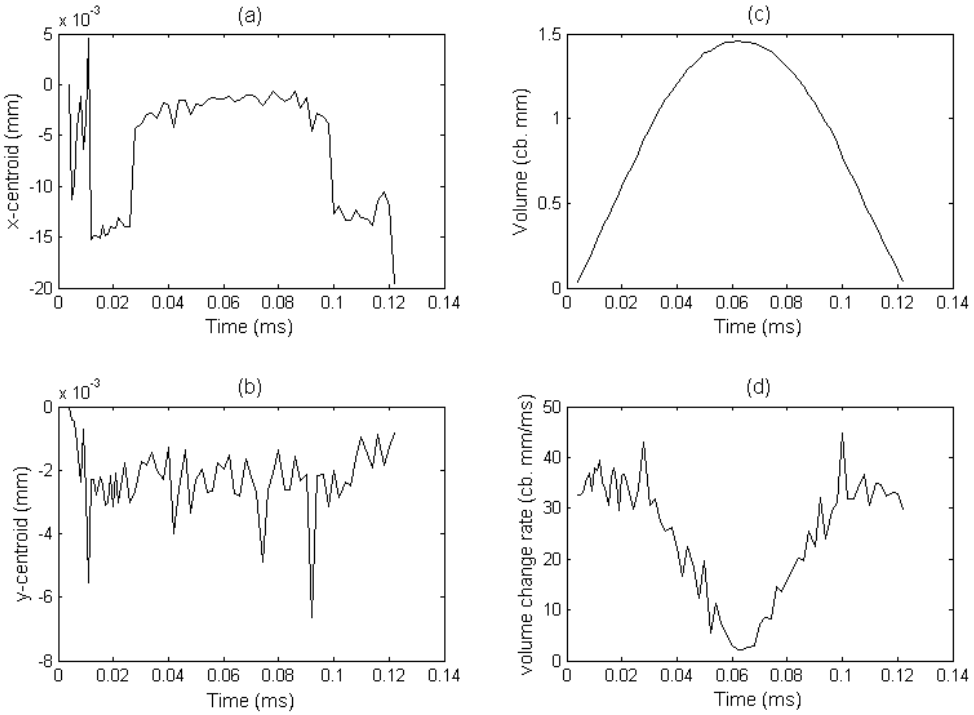

Fig. 4.6 Geometric data of spherical cavitation bubble with $R_m \approx$ 0.7033 mm

Figure 4.6d shows the change rate of volume against time[23]. It clearly demonstrates that higher change rates of volume are close to both the initial point and the collapse point, and during the phases of growth and collapse the

---

[22] The time from the maximum to the next minimum of the bubble volumes

[23] The original data shown in the figure can be further post-processed by using fitting methods such as least-square fitting for obtaining a smooth curve and better illustration.

change rate is monotonically decreasing and increasing, respectively. As the bubble is approaching the maximum volume, the change rate of volume achieves the lowest value, indicating all the kinetic energy being converted as the potential energy at the maximum volume and then the unstable equilibrium being broken by the pressure in the ambient environment driving the bubble to collapse.

Figure 4.7 shows the time history of relative change in temperature and pressure by assuming an adiabatic process with the heat capacity ratio, γ_c = 1.4. All the time scale in Fig. 4.7 has been normalized by the Rayleigh collapse time T_c. In Figs. 4.7a and 4.7b the time history of volume is normalized by the maximum and initial volumes of bubble, respectively. The curves of the relative change in pressure and temperature in Figs 4.7c and 4.7d are obtained by utilizing eq. (4.5) and eq. (4.6) to deduce the following relationships, respectively.

$$\frac{P}{P_m} = \left(\frac{V_m}{V} \right)^{\gamma_c} \tag{4.5}$$

$$\frac{TP}{TP_0} = \left(\frac{V_0}{V} \right)^{\gamma_c - 1} \tag{4.6}$$

where P , V , and TP are the pressure, volume, and temperature, respectively. V_m and P_m are the maximum volume and the minimum pressure, respectively; V_0 and TP_0 are the initial value of volume and temperature, respectively.

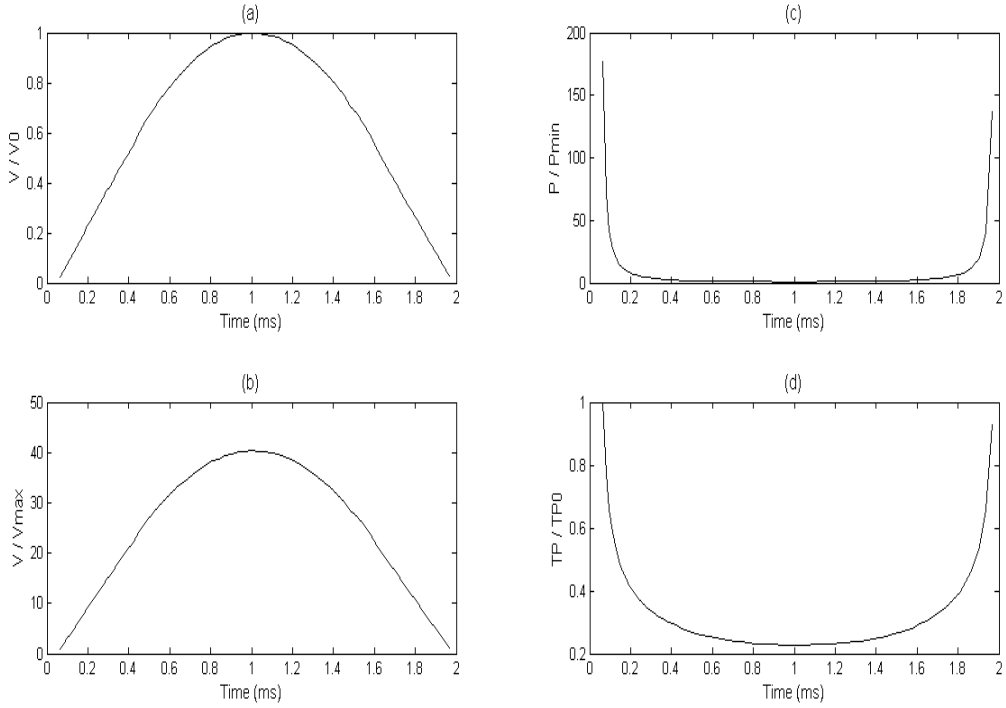

Fig. 4.7 The time history of relative change in temperature and pressure

Figure 4.7c shows the time history of relative change in pressure normalized by the pressure at maximum of volume. Figure 4.7d shows the time history of relative change in temperature normalized by the initial temperature. The tendency of violent collapse close to the final stage of collapse in both curves is closely reflected. However, owing to the low temporal resolution of this

case[24] and low sampling points close to the collapse, the relative change of pressure and temperature at that moment cannot be resolved. Nevertheless, this issue can be solved once the temporal resolution there is improved. As shown in the above figures, with the help of active contour method developed from this PhD study, for the first time the global dynamics of cavitation bubble can be correctly and accurately quantified from the experimental images. This method will greatly benefit the physical modelling of bubble cavitation by comparing the quantitative experimental data with the numerical data calculated from physical models of cavitation bubble.

Now, let us exam these experimental data by comparing with the classical theory of spherical cavitation bubble. The Rayleigh collapse time derived for the collapse of spherical cavitation bubble by Lord Rayleigh (Rayleight 1917) has been adapted widely for comparing with experimental data, e.g. (Vogel, Lauterborn et al. 1989). This characteristic time denoted as the time of cavitation bubble from its maximum size to its first collapse. The Rayleigh collapse time T_c is written as

[24] The inter-frame interval is 2 μs .

$$T_c = 0.915 R_{\max} \sqrt{\frac{\rho_\infty}{p_\infty - p_v}} \tag{4.7}$$

Here, ρ_∞ denotes the density of the liquid and $p_\infty - p_v$ denotes the difference between the static pressure and the vapour pressure of the liquid, water in this case. For water at 20 ^0C, $\rho_\infty = 998 \ \frac{kg}{m^3}$, $p_v = 2330 \ pa$, and $p_\infty = 1.01325 \times 10^5 \ pa$. The maximum of radius for this case, $R_m \approx$ 0.7033 mm, is approximately calculated from the maximum volume of bubble obtained from active contour method with the assumption of spherical bubble[25]. Note that the cavitation bubble in this case is actually a spheroid with long and short axis[26] instead of a completely spherical bubble. Although it looks like a circular shape in Fig. 4.4, the difference between the long and short axis varies within 50 μm which is the distance hard to be perceived. This is due to a small size of bubble undergoing a high instability of bubble shape under the optical breakdown of elliptic shape. Nevertheless, it has been confirmed that T_c is still validated for this kind of spheroid-shaped cavitation bubble, even for the cavitation bubble with a ratio 5:1 between the

[25] The bubble radius is corresponded to the radius of sphere with the same volume as the spheroid.

[26] This can be calculated from the bubble contour obtained from the active contour method.

long and short axis induced by a femto-second optical breakdown (Vogel, Noack et al. 1999). Therefore, the collapse time T_c based on $R_m \approx 0.7033$ mm is 64.61 μs which is an error of 4 percent comparing with 62 μs of experimental estimation. This error has been formed mainly due to a measured error from the scale calculation on the spatial resolution of optical magnification. After a scale correction, the error has been reduced to below 2 percent, which is a satisfactory result in general.

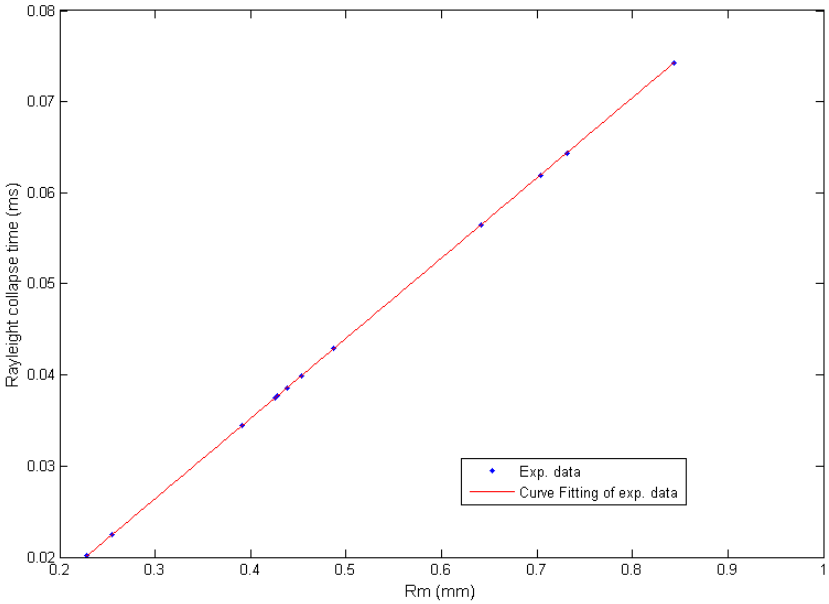

Fig. 4.8 Rayleigh collapse time of spherical cavitation bubble against the maximum volume of bubble

In Fig. 4.8 the Rayleigh collapse time with respect to the maximum radius of spherical cavitation bubble is plotted. Here, the maximum volume of bubbles

obtained from the active contour method is used for estimating the effective maximum radius of bubble. Then the fitting curve of Rayleigh collapse time is obtained by substituting these experimentally obtained effective maximum bubble radiuses into eq. 4.7.

Except for the Rayleigh collapse time, the mechanic energy E_B of spherical cavitation bubble can also be calculated directly from the maximum volume obtained by the active contour method. The energy is written as

$$E_B = \frac{4}{3}\pi\left(p_\infty - p_v\right)R_{\max}^3 = \left(p_\infty - p_v\right)V_{\max} \tag{4.8}$$

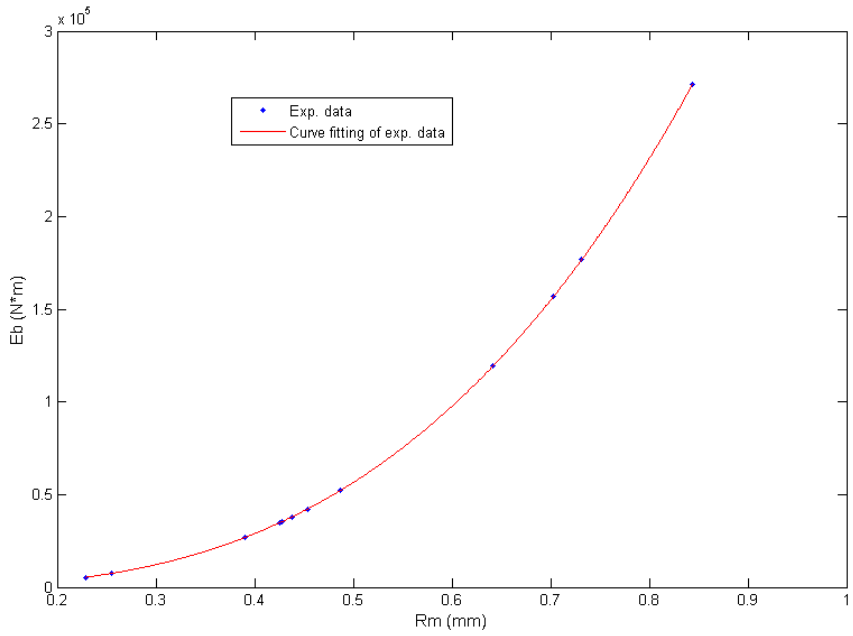

Fig. 4.9 Mechanic energy of spherical cavitation bubble with respect to maximum volume

Figure 4.9 shows the mechanic energy of spherical cavitation bubble with

respect to time. The fitting curve is obtained by substituting the maximum volume of bubble measured by the active contour methods into eq. 4.8.

4.5 Discussion and Results of Non-spherical Cavitation Bubble

The behaviours of non-spherical cavitation bubble can be classified into three types subject to the environments. Bubble could be interacting with rigid wall, soft wall, and free surface. Among these interactions, the bubble-wall interaction is the hottest research topic owing to its direct connection with the mechanism of cavitation erosion towards the nearby materials. The behaviour of non-spherical cavitation bubble is generally subject to a characterized non-dimensional stand-off parameter γ , which is defined as the ratio of the distance between initial bubble centre and boundary surface to the maximum bubble radius R_m . Its behaviour has been studied extensively and qualitatively using the laser-induced bubbles as reported in many documents since the first report in 1975 (Lauterborn and Bolle 1975). However, the dynamics of cavitation bubble have been mainly focused on local rather global behaviour of bubble due to the difficulty in quantitative analysis of

images. Now, by utilizing the active contour method, the global behaviour of non-spherical cavitation bubble close to the wall boundary can be quantitatively studied. In this section, for the purpose of demonstration we select a few typical cases from experimental results of bubble interactions with rigid wall and soft wall.

4.5.1 Interaction between Non-spherical Cavitation Bubble and Rigid-wall Boundary

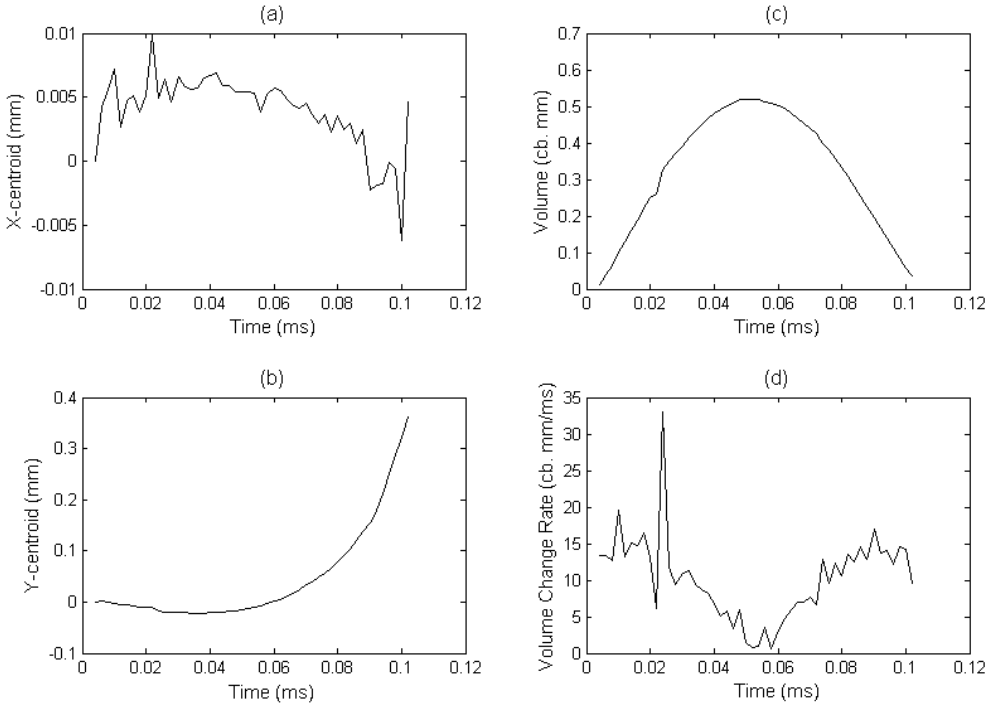

Figure 4.10 The non-spherical cavitation bubble nearby rigid wall with $R_m \approx$ 0.5 mm and $\gamma \approx 1.2$.

Figure 4.10 shows the geometric data of non-spherical cavitation bubble with

$R_m \approx$ 0.5 mm and $\gamma \approx 1.2$. Figures 4.10a and 4.10b show the movement of bubble centroids. The bubble drifts very little in the x-coordinate, which is parallel to wall. On the contrary, the y-coordinate of bubble centroid is pulled towards the wall boundary[27]. Figures 4.10c and 4.10d show the volume and the volume change rate of bubble, respectively. The sharp jump on the change rate of volume is due to the uneven illumination of backlight that results in a slightly inaccurate measurement on the bubble volume. The tendency of volume change rate in Fig. 4.10d is generally similar to that of spherical bubble.

Figure 4.11 shows the time history of relative pressure and temperature. All the time scale has been normalized by the time at which the bubble reaches the maximum volume. The volume is normalized to the maximum volume and the initial volume in Figs. 4.11a and 4.11b, respectively. Figures 4.11c and 4.11d show the relative change of pressure and temperature normalized by the pressure at maximum volume and the initial temperature, respectively. The curve of relative pressure close to the final stage of collapse as shown in

[27] The wall boundary is in the upper side where the ordinate is positive.

Figure 4.11c is difficult to obtain because the bubble image is attached to the wall-boundary image.

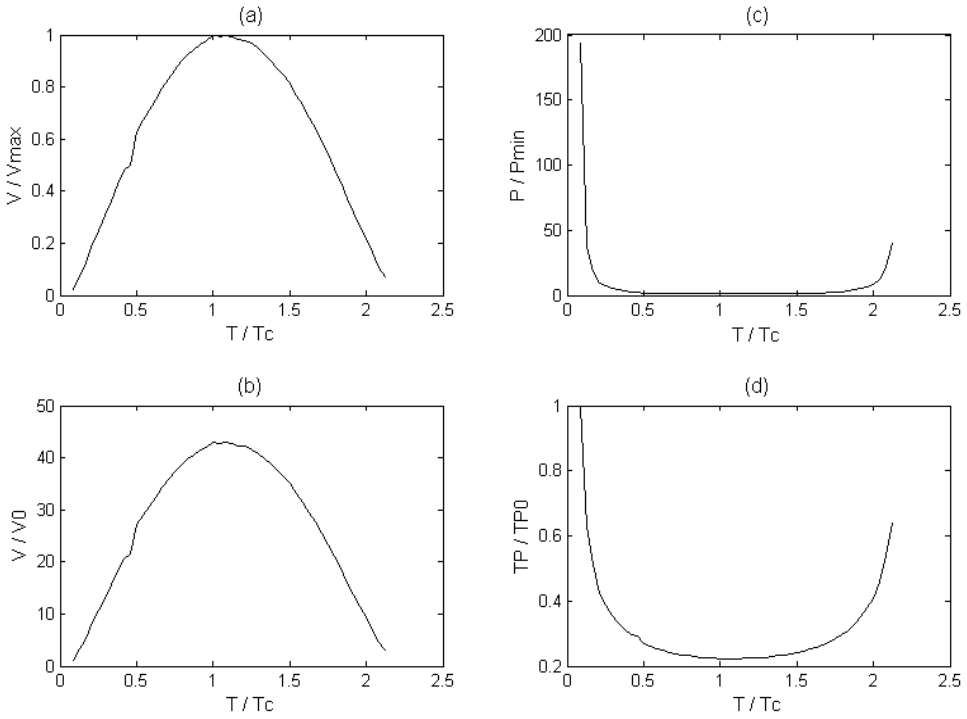

Fig. 4.11 The relative pressure and temperature of bubble nearby rigid wall with $R_m \approx$ 0.5 mm and $\gamma \approx 1.2$

4.5.2 Interaction between Non-spherical Cavitation Bubble and Soft-wall Boundary.

Figure 4.12 shows the geometric data of non-spherical cavitation bubble close to a soft wall with $R_m \approx$ 0.633 mm and $\gamma \approx 1.07$. The x-coordinate of centroid in Fig. 4.12a remains steady as the previous cases. However, the y-coordinate of centroid in Fig. 4.12b quantitatively reveals a drastically

different behaviour of the bubble interacting with a nearby soft wall from those collapsing bubbles close to a nearby rigid wall. As observed from the high-speed video images, the bubble with a nearby soft wall moves away from the wall during the expansion of the bubble but it moves to the wall before collapsing onto the wall; whereas the bubble with a nearby rigid wall is directly attracted towards the wall. In Fig. 4.12d, the first sharp jump of volume change rate is caused by the uneven illumination from the backlight, which is also observed in Fig. 4.10d.

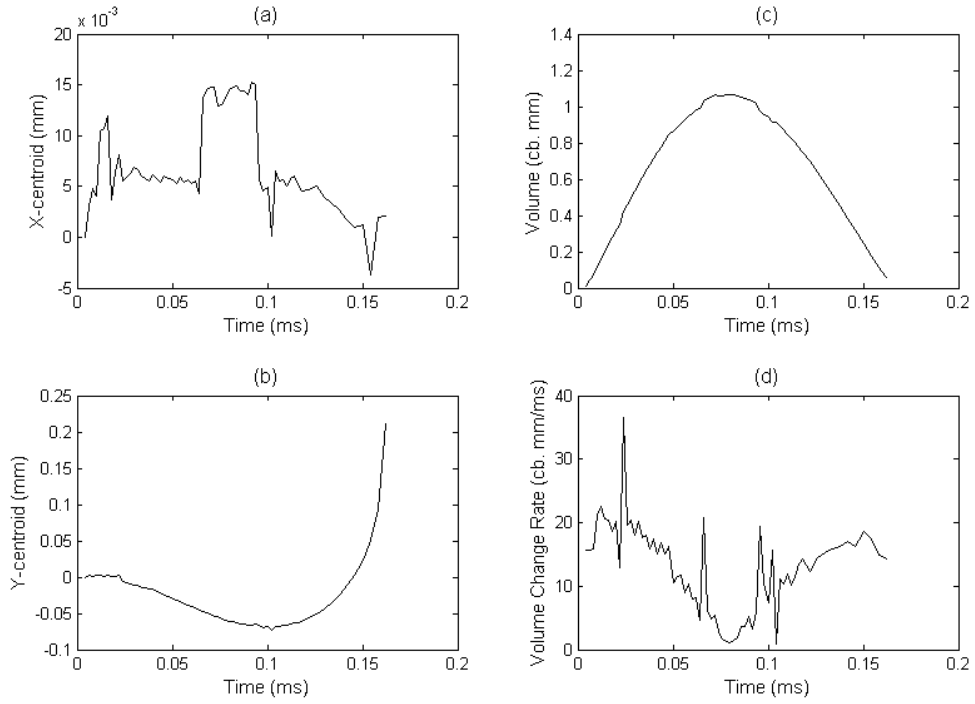

Fig. 4.12 The non-spherical cavitation bubble nearby soft wall with $R_m \approx$ 0.633 mm and $\gamma \approx 1.07$

However, the next two sharp jumps in the volume change rate which are not

observed in the case of rigid wall might be arguably owing to the effect of floating behaviour which results in the variation in bubble shape. This needs to be further investigated to conclude in the future.

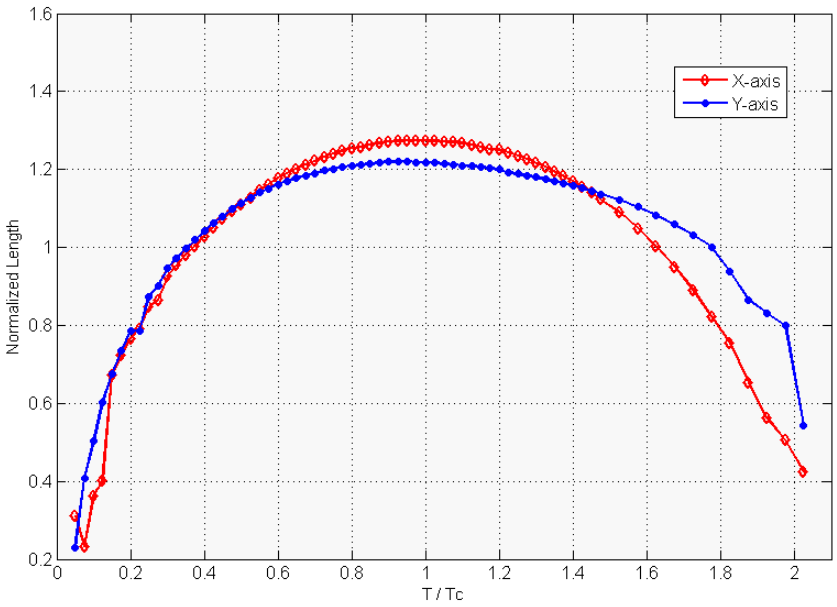

Fig. 4.13 The shape variation of cavitation bubble

It has been quantitatively observed from the geometric data of bubble contour that there are shape variations against time in terms of interchanging the long and short axes of bubble in this area. Figure 4.13 shows the length variations of bubble X-axis and Y-axis with $R_m \approx 0.633$ mm and $\gamma \approx 1.07$. The shape of cavitation bubble firstly varies from sphere to spheroid and, then, from oblate to prolate spheroid. Furthermore, Figure 4.13 also shows the normalized length of X-axis and Y-axis of bubble against normalized time

with solid dot lines. The length variations against time in the initial stage of growth and final stage of collapse are more drastic than those in the middle where the volume change rate is more smooth and steady. These quantitative geometric data are globally obtained for the first time and can be compared with numerical data for investigating the shape instability of cavitation bubble during the first cycle of growth and collapse.

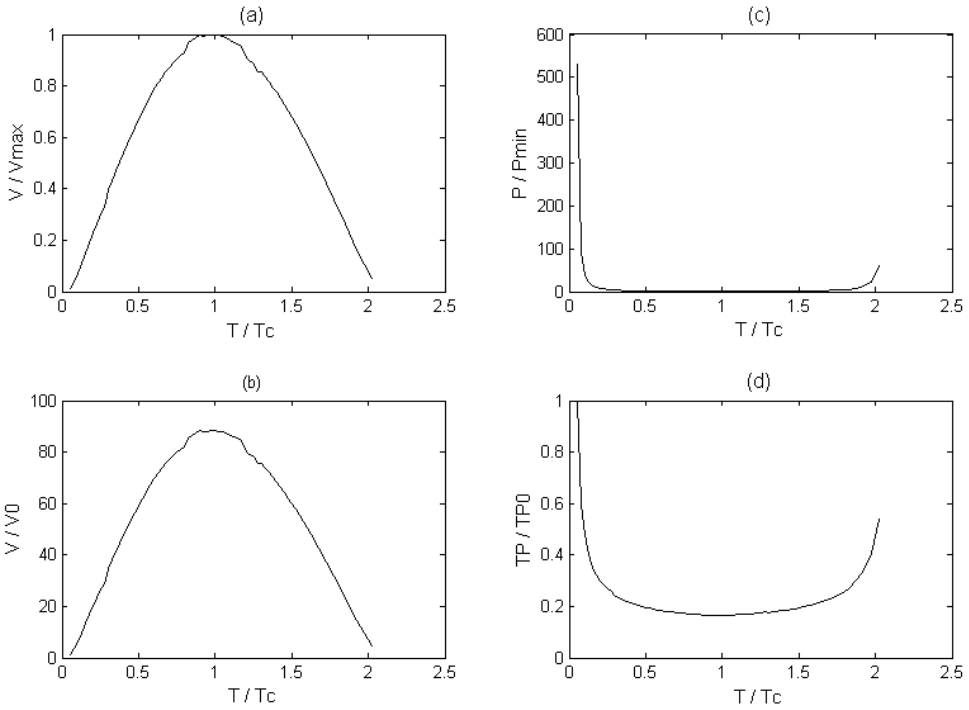

Fig. 4.14 The relative pressure and temperature of bubble nearby soft wall with $R_m \approx$ 0.633 mm and $\gamma \approx 1.07$

Figure 4.14 shows the time history of relative pressure and temperature of bubble with $R_m \approx$ 0.633 mm and $\gamma \approx 1.07$.

4.6 Summary

In this chapter, the experiment of laser-induced cavitation bubble in microscale has been conducted for quantitatively revealing the behaviours of spherical and non-spherical cavitation bubble. Through this demonstration case, the newly developed novel method for delineating the cavitation bubble contour is demonstrated showing its ability to quantitatively analyse the behaviour of cavitation bubble. By utilising this novel method as explained in detail in the next chapter, various geometric and dynamic data of cavitation bubble can be extracted quantitatively for further analysing the global behaviour of bubbles thoroughly. This technique can make further advance in the physical modelling of cavitation bubble.

Chapter 5

Active Contour Method for Bubble Contour Delineation

5.1 Introduction of Image Segmentation

The image segmentation is generally defined as "a process of partitioning an image into homogenous groups such that each region is homogenous but the union of no two adjacent regions is homogenous (Pal and Pal 1993)." It is an essential technique for many scientific and industrial applications such as medical imaging and computer vision, etc. The purpose of image segmentation is to partition an image into meaningful regions where the objectives are described, recognised, and classified. By using this technique for image pre-process, regions of interest can be identified and isolated. One can characterize the objectives for group classification and/or for extraction of particular information subject to the segmentation method employed. For example, in order to analyze the dynamics of cavitation bubble using the

images captured by ultra high speed camera, the variations of bubble contour and corresponding geometric parameters such as the radius and volumetric (or mass) centre etc are fundamentally essential information. The image segmentation offers an effective way acquiring such information and also can standardize the procedure for cavitation bubble analysis based on the images obtained from the experiment. Harvey et al. (Harvey, Best et al. 1996) uses the thresholding method to analyse the first pulsation of cavitation bubble (i.e. the phase of expansion and collapse) nearby the wall boundary. In the Zuo's PhD thesis (Zuo 2008), various techniques of image segmentation such as Thresholds method and active contour method (snake) have been introduced for the use of cavitation cloud and spherical cavitation bubble in the free space, respectively. Therefore, it is a promising approach for quantifying and analysing the experimentally obtained images of bubbles. In this thesis, the active contour methods are employed and developed a step further in an automatic and self-adjusting way to dynamically acquire various contours of spherical and non-spherical cavitation bubbles in infinite space and with nearby boundaries etc. A new variant of active contour method is introduced to meet the specific need in the delineation of cavitation bubble contour.

Furthermore, through this process of image segmentation, a systematic procedure for analysing a series of cavitation bubble images taken by an ultra high speed camera has been standardized as well.

5.2 Active Contour Method (Snake)

According to their concept and technique, there are various approaches for image segmentation. Based on the concept, i.e. boundary (exterior border) and region (interior space), most segmentation approaches fall into two main categories: edge-based and region-based methods. The region-based methods is to find regions based on the similarity of neighbouring pixels whereas the edge-based methods is to find the edge pixels based on the difference within the pixels of image and link them to delineate a contour. According to the technique employed, they can be classified as contextual technique that considers the relationships between the features (i.e. the gray-level values, texture and gradient magnitude, etc) in an image and the non-contextual technique that ignores these relationships (i.e. simply segment each pixels into a histogram based on gray-level value only). The segmentation methods often utilise multiple techniques and concepts in conjunction with each other.

This further complicates the classification of segmentation methods based on a single criterion. For more information on image segmentation methods, readers are referred to the book by Dougherty (Dougherty 2009). For more detail of various approaches and classifications of image segmentation please refer to the review papers (Pal and Pal 1993, Pham, Xu et al. 2000).

The method selection for image segmentation is subject to its application together with the scale of information sought for. The simplest method of image segmentation currently used widely is a pixel-based method such as the threshold method. The image is segmented into a binary image by setting a threshold to distinguish the distinct frequency distributions of regions based on the grey-level scale of each pixel in the histogram. However, the drawback of this method is the lack of sensitivity to accurately classify the regions where the contrast is poor, in particular for those regions of interest sharing similar properties to the adjacent regions. For example, for the image of cavitation bubble with nearby wall boundary captured by the shadowgraph technique, both bubble and wall boundary show very little contrast to each other. Moreover, the success of this method strongly depends on the selection

of an appropriated global threshold for segmenting the whole image or a series of images, especially as the frequency distribution in the histogram has an overlapping bi-mode or multiple-mode. Therefore, threshold method is not suitable for our application based on above reasons and a more sophisticated segmentation method is needed. For the image of cavitation bubble the region of interest is often a continuously smooth closed contour. Consequently, the edge-based method is also not suitable for our application owing to its major drawback, i.e. easily forming disconnected or spurious edges. The region-based method such as region growing method is too sensitive for the selection and the location of seed pixels which might potentially bias the segmented result and incorrectly resolve the edges of adjacent regions.

The active contour method offers a promising alternative solution that satisfies our application. The active contour method (i.e. snakes) was firstly introduced by Kass et al. (Kass, Witkin et al. 1988) for detecting the salient features of image (i.e. the edges, lines, and subjective contours). The active contour is a controlled continuous spline imposed upon the image to locate or enclose these features of image by minimizing an associated energy functional. This energy functional is composed of a sum of internal and

external energies which represent the spline and image features, respectively. As the energy of spline attains the local minimum of energy in the image, the contour (i.e. the features of image) is delineated and matched by the spline. This method is also named as snake because the active contour deforms elastically and flexibly during the iterations in finding the energy minimum.

The mathematic model of active contour method is based on solving energy functional E_{snake} by Euler-Lagrange Equation to attain its local minima (Kass, Witkin et al. 1988). The energy functional is written as

$$E_{snake} = \int_{s} \left(E_{\text{int}} + E_{ext} \right) ds \tag{5.1}$$

where E_{int} and E_{ext} denote the internal spline energy and the external image energy, respectively and $s \in [0,1]$.

Given a parametric curve $\chi(s) = (x(s), y(s))$ where (x, y) is two-dimensional coordinate system representing the location of curve on the image plane and s is dummy variable representing a set of intervals of the curve within the predefined end-points. The internal energy E_{int} is

formulated as

$$E_{int} = \int_s \frac{1}{2}\left(\alpha \left|\chi_s(s)\right|^2 + \beta \left|\chi_{ss}(s)\right|^2\right) ds \tag{5.2}$$

where the weighting parameters, α and β, allow us to control the elasticity and stiffness of active contour. $\chi_s(s)$ and $\chi_{ss}(s)$ denote the first and second derivatives of $\chi(s)$ with respect to s.

The external energy E_{ext} can be formulated in many ways depending on the features of image interested (Kass, Witkin et al. 1988). For example, given a gray-level scale distribution of image $I(x, y)$, the simplest image energy functional is $\pm I(x, y)$, for which the active contour will be attracted towards the bright or dark lines depending on the sign[28] of image energy. Another example for finding edges in an image is a simple energy functional $-\left|\nabla I(x, y)\right|^2$, for which the active contour is attracted towards the edges with large gradients of gray-level scale. The external energy can also be devised to convolute with a Gaussian function of standard distribution σ

[28] For positive sign the active contour is attracted to dark lines on the bright background; for negative sign, tendency is toward bright lines on the dark background.

for blurring the image energy[29]. This filter operator can increase the capture range that the active contour can detect and travel towards the equilibrium. But it comes with a penalty of losing the detail of image that also results in a difficulty for the active contours to localize the features of image. The energy functional E_{snake} is then rewritten as

$$E_{snake} = \int_s \left(\frac{1}{2}(\alpha(s)|\chi_s(s)|^2 + \beta(s)|\chi_{ss}(s)|^2) + E_{ext}(\chi(s)) \right) ds \qquad (5.3)$$

By applying calculus of variations for obtaining a stationary point of energy functional E_{snake}, the Euler-Lagrange Equation is obtained as

$$\alpha\chi_{ss}(s) - \beta\chi_{ssss}(s) - \nabla E_{ext}(\chi(s)) = 0 \qquad (5.4)$$

This equation is also a force balance equation[30]. By solving eq. (5.4) numerically, the solution obtained reflects the features of image interested.

---

[29] Gaussian filter is a spatial smoothing operator that can remove detail and noise resulting a blurring of image.

[30] i.e. $F_{\text{int}} + F_{ext} = 0$, where $F_{\text{int}} = \alpha\chi_{ss}(s) - \beta\chi_{ssss}(s)$ and $F_{ext} = -\nabla E_{ext}(\chi(s))$

5.3 Motion tracking by Active Contour Method (EGVF Snake)

The snake method is a breakthrough that utilise the idea of energy functional minimization for image segmentation and motion tracking. However there are two difficulties with the traditional snake. Firstly, the traditional snake often gets stuck in the local minima caused by the non-uniform illumination or noise other than the true minima. The initial active contour needs to be assigned as close as possible to the target of interest in order to locate the features of target successfully. Secondly, the traditional snake is unstable for those of highly concave boundaries, often generating incorrect shapes of contour. In order to resolve these problems, the Gradient Vector Flow field (GVF) is introduced as a new external force for the active contour methods by Xu et al. (Xu and Prince 1998). It is derived from the image by minimizing a certain energy functional that is composed of a pair of decoupled linear partial differential equations. The idea of GVF is to diffuse the gradient vectors of a gray-level scale edge map computed from image. Given a vector field $V(x,y) = (u(x,y), v(x,y))$, the energy functional E_{GVF} for obtaining GVF field is defined as

$$E_{GVF} = \iint \left(\mu(u_x^2 + u_y^2 + v_x^2 + v_y^2) + |\nabla f|^2 |V - \nabla f|^2 \right) dxdy \qquad (5.5)$$

where μ is a control parameter for reducing the effect caused by noise and ∇f is defined as the gradient of edge map[31] $f(x,y)$. This energy functional is designed to preserve the property of edge map that has vectors pointing toward the edges and to improve the capture range of active contour. By applying the calculus of variation, the Euler-Lagrange Equations are obtained as

$$\begin{cases} \mu\nabla^2 u - \left(f_x^2 + f_y^2\right)(u - f_x) = 0 \\ \mu\nabla^2 v - \left(f_x^2 + f_y^2\right)(v - f_y) = 0 \end{cases} \qquad (5.6)$$

where ∇^2 is the Laplacian operator and μ is a non-negative parameter controlling the smoothness of the field $V(x,y)$. The GVF field is then obtained by solving eq. (5.6) numerically. As ∇f is zero (i.e. the edge map is constant), the above equations become a set of Laplace equations. In these homogenous regions the GVF field is dominated by the diffusion from the near-by boundary vectors resulting in a competition among these boundary

[31] The edge map could be any combination of the external forces used in the traditional snake.

vectors. Herein, this overcomes the problem of concavities in the traditional snake. As the GVF field is computed, it replaces the original external force in the traditional snake as a new external force to obtain the GVF snake below

$$\alpha\chi_{ss}(s)-\beta\chi_{ssss}(s)+V_{GVF}=0 \tag{5.7}$$

Furthermore, a Generalized GVF (GGVF) snake is proposed by Xu and Prince (Xu and Prince 1998) by replacing the constant μ and $|\nabla f|^2$ in the equation of GVF field with more general weighting functions g and h. The generalized GVF snake is defined as

$$\begin{cases} g\left(|\nabla f|\right)\nabla^2 u - h\left(|\nabla f|\right)\left(u-\nabla f_x\right)=0 \\ g\left(|\nabla f|\right)\nabla^2 v - h\left(|\nabla f|\right)\left(v-\nabla f_y\right)=0 \end{cases} \tag{5.8}$$

where $g(|\nabla f|)=\exp\left(-\left(\frac{|\nabla f|}{K}\right)\right)$ and $h\left(|\nabla f|\right)=1-g\left(|\nabla f|\right)$

The constant K in eq. (5.8) is a positive user-defined constant controlling the smoothness of GGVF field. The GGVF snake improves the convergence rate of active contour in the long, thin boundary indentations where the GVF snake would take very long time to converge. Except for the better boundary localization over the GVF snake that can be seen as a special case of GGVF

snake, GGVF snake also has better performance on noisy images.

The devised mechanism of snake enables the active contour to deform flexibly toward the salient image features, which are subject to the external image force and various constraint forces[32], through a process of energy minimization. Then the active contour locks onto their boundary where the locations are the energy minimum. This mechanism allows the snake to segment and track the target simultaneously, provided the frame-to-frame movement of target is slow enough for the active contour to relocate the same energy minimum and lock onto it again. The ability to track the movement of target makes active contour method more popular in biological imaging analysis, especially for the study of cell movement. For the detailed discussion on using active contour model to track the cell motion, the reader is referred to the work of Leymarie and Levine (Leymarie and Levine 1993). Based on the GGVF snake, Ray et al. (Ray, Acton et al. 2002) propose an enhanced external force for tracking the fast-rolling leukocytes in order to overcome the shortcomings of GGVF snake when used in the motion

[32] The prior knowledge of image features observed can be imposed as the constraint force.

tracking. This modified external force is named as Enhanced Gradient Vector Flow (EGVF) for distinguishing from GGVF. In the EGVF field, a Dirichlet boundary condition is imposed as a constraint onto the GVF field to obtain the EGVF-PDE equations as the following

$$\left.\begin{aligned} g\nabla^2 u - (1-g)\left(u - f_x\right) = 0 \\ g\nabla^2 v - (1-g)\left(v - f_y\right) = 0 \end{aligned}\right\} \quad ,(u,v) \in (D - C)$$
$$(u,v) = \vec{n} \qquad ,(x,y) \in \partial C \tag{5.9}$$
$$\nabla(u,v) = 0 \qquad ,(x,y) \in \partial D$$

where D denotes the domain of image with boundary ∂D and C denotes the domain of initial active contour with boundary ∂C. $\vec{n}$ is a unit outward vector normal to the boundary. Through the constraint of Dirichlet boundary condition, EGVF snake overcome the sensitivity problem of initial location in the GGVF field where the initial snake is required to contain the medial axis of target, otherwise the snake will collapse to the nearby boundary. Also, the unit outward vector $\vec{n}$ in the Dirichlet boundary condition can be replaced by a velocity direction vector of prior knowledge. Whit this estimated direction of movement, the EGVF field is biased in the direction of motion. As a result, the allowed maximum displacement of target is extended further within frames and the initial snake will move toward the

target along this biased direction. This enhancement greatly improves the capability of EGVF snake to track the fast-moving target since the maximum displacement in GGVF snake is less than the radius of target. After solving eq. (5.9) iteratively for obtaining the EGVF field V_{EGVF}, the solution V_{EGVF} is used as a new external force to obtain EGVF snake,

$$\alpha\chi_{ss}(s)-\beta\chi_{ssss}(s)+V_{EGVF}=0 \tag{5.10}$$

5.4 Implementation of Active Contour Method for Tracking Cavitation Bubble

In this thesis the EGVF snake proposed by Ray et al. (Ray, Acton et al. 2002) is adapted to track the dynamics of cavitation bubble owing to its superiority over the GGVF snake as described before. Supposing that there is a temporal sequence of images, the tracking algorithm devised for our application with the nearest neighbour assumption[33] is briefly explained as follows

1. *Target detection*

[33] The nearest neighbour assumption is that the closest detection in space with respect to a previous target position is matched to a given criteria.

A target is detected manually by placing an initial active contour onto the target in the first frame. Then the evolution of active contour is iteratively solved to delineate the target.

2. *Tracking*

a. *Initial active contour placement*

The final contour delineating the target from the previous frame is placed onto the target of the current video frame as an initial active contour.

b. *Active contour evolution*

The evolution of active contour is literately solved to delineate the target of current video frame.

Now, we should look into the discretization scheme for active contour methods. To solve the snake introduced by the Kass et al. (Kass, Witkin et al. 1988), we can apply the gradient decent method, i.e. first-order optimization algorithm, to eq. 5.10 as follows,

$$\frac{\partial X}{\partial \tau} = \alpha \frac{\partial^2 X}{\partial s^2} - \beta \frac{\partial^4 X}{\partial s^4} + \frac{\partial f}{\partial x} \qquad (5.11)$$

$$\frac{\partial Y}{\partial \tau} = \alpha \frac{\partial^2 Y}{\partial s^2} - \beta \frac{\partial^4 Y}{\partial s^4} + \frac{\partial f}{\partial y} \tag{5.12}$$

Let both $\frac{\partial X}{\partial \tau}$ and $\frac{\partial Y}{\partial \tau}$ be zero, the local minimum is reached, and the target contours is thus delineated by the snake.

In order to solve this by iteration method, the continuous curve of snake $\chi(s) = (x(s), y(s))$, $s \in [0,1]$ is approximated to a discrete curve of snake which is a set of discrete points, snaxels[34], which is $(x(s), y(s)) \to (x_i, y_i)$, $s \in [0,1] \to i \in \{0,1,.....,n-1\}$. n is the total number of snaxels, control points, of snake. The eq. (5.12) and eq. (5.13) in finite discretization scheme are

$$\frac{X_i^{\tau+1} - X_i^{\tau}}{\delta t} = \alpha\left(X_{i+1}^{\tau} - 2X_i^{\tau} + X_{i-1}^{\tau}\right) - \beta\left(X_{i+2}^{\tau} - 4X_{i+1}^{\tau} + 6X_i^{\tau} - 4X_{i-1}^{\tau} + X_{i-2}^{\tau}\right) + f_x(X_i^{\tau} + Y_i^{\tau}) \tag{5.13}$$

$$\frac{Y_i^{\tau+1} - Y_i^{\tau}}{\delta t} = \alpha\left(Y_{i+i}^{\tau} - 2Y_i^{\tau} + Y_{i-1}^{\tau}\right) - \beta\left(Y_{i+2}^{\tau} - 4Y_{i+1}^{\tau} + 6Y_i^{\tau} - 4Y_{i-1}^{\tau} + Y_{i-2}^{\tau}\right) + f_y(X_i^{\tau} + Y_i^{\tau}) \tag{5.14}$$

where τ and $\tau + 1$ represent the two successive discrete time points with a

---

[34] The sampled vertices are referred to as snaxels that represent the control points of the curve.

time interval δt.

Let

$$x^{\tau}=\begin{bmatrix} X_0^{\tau} \\ \vdots \\ X_{n-1}^{\tau} \end{bmatrix} \quad , \quad y^{\tau}=\begin{bmatrix} Y_0^{\tau} \\ \vdots \\ Y_{n-1}^{\tau} \end{bmatrix} \quad , \quad f_x^{\tau}=\begin{bmatrix} f_x(X_0^{\tau},Y_0^{\tau}) \\ \vdots \\ f_x(X_{n-1}^{\tau},Y_{n-1}^{\tau}) \end{bmatrix} \quad , \quad f_y^{\tau}=\begin{bmatrix} f_y(X_0^{\tau},Y_0^{\tau}) \\ \vdots \\ f_y(X_{n-1}^{\tau},Y_{n-1}^{\tau}) \end{bmatrix}$$

The eq. (5.13) and eq. (5.14) can be rewritten in the matrix form as follows

$$\frac{x^{\tau+1}-x^{\tau}}{\delta t}=-Ax^{\tau}+f_x^{\tau} \tag{5.15}$$

$$\frac{y^{\tau+1}-y^{\tau}}{\delta t}=-Ay^{\tau}+f_y^{\tau} \tag{5.16}$$

where A is a sparse matrix as shown in eq. (5.17).

$$A=\begin{bmatrix} c & b & a & & & a & b \\ b & c & b & a & & & a \\ a & b & c & b & a & & \\ & \ddots & \ddots & \ddots & \ddots & \ddots & \\ & & a & b & c & b & a \\ a & & & a & b & c & d \\ b & a & & & a & b & c \end{bmatrix} \tag{5.17}$$

In eq. (5.17) $a=\beta$, $b=-(4\beta+\alpha)$, $c=6\beta+2\alpha$.

Rearranging eq. (5.15) and (5.16)

$$x^{\tau+1} = x^{\tau} - \delta t(Ax^{\tau} - f_x^{\tau}) \tag{5.18}$$

$$y^{\tau+1} = y^{\tau} - \delta t(Ay^{\tau} - f_y^{\tau}) \tag{5.19}$$

The snake location at time $\tau+1$ is updated from the previous location at time τ following eq. (5.18) and eq. (5.19). This explicit scheme of finite difference method is straightforward but suffers from numerical instability subject to the chosen time step δt. Therefore, implicit scheme is preferable since it is numerically much more stable and converges much quicker. By using backward difference to discretize eq. (5.11) and (5.12), a implicit scheme can obtained be obtained as

$$x^{\tau+1} = \left(I_n + \delta t \cdot A\right)^{-1}(x^{\tau} + \delta t \cdot f_x^{\tau}) \tag{5.20}$$

$$y^{\tau+1} = \left(I_n + \delta t \cdot A\right)^{-1}(y^{\tau} + \delta t \cdot f_y^{\tau}) \tag{5.21}$$

where I_n is a n-by-n identity matrix. The matrix $\left(I_n + \delta t \cdot A\right)$ is positive definite and, herein, invertible. The eq. (5.20) and eq. (5.21) are referred as the snake evolution equations.

By iteratively solving these two equations, the contour of target is delineated by the snake. The stopping criteria is usually set either as a prescribed

numbers of iteration being achieved or a distance between the snaxels in the consecutive iterations being below a prescribed limit. For obtaining the solution of the GGVF or EGVF snake, the external force $\left(f_x^\tau, f_y^\tau\right)$ in the eq. (5.20) and eq. (5.21) is simply substituted with the external force V_{GGVF} and V_{EGVF}.

Although the snake introduced by Kass et al. (Kass, Witkin et al. 1988) gives an elegant method that can dynamically conform to the contour of target, there are still some problems (Brigger, Hoeg et al. 2000). They are (a) slow convergence due to the large number of coefficients to optimize the snake, (b) difficulty in determining the weights associated with smoothness constraints, and (c) the curve formed by a finite set of disconnected points. Therefore, a more subtle and compact parameterization method, B-spline snake, is thus developed in order to reduce the controlled parameters in the snake evolution equation by containing the control of smoothness implicitly within the spline itself (Menet, Marc et al. 1990, Menet, Saint-Marc et al. 1990). Brigger et al. (Brigger, Hoeg et al. 2000) further extends the concept of B-spline snake in order to improve its efficiency and proves that the cubic B-spline among

various families of spline has optimal solution for the snake cost function. Herein, in this study, the cubic B-spline is adapted to parameterize the internal energy of snake. A cubic B-spline $(x(s), y(s))$, $s \in [0,1]$,is a continuous curve of C^2 class that can be defined by a sequence of $N+3$ control points with integer $N > 0$,

$$X(s_{i,u}) = \begin{bmatrix} u^3 & u^2 & u^1 & 1 \end{bmatrix} M \begin{bmatrix} X_i \\ X_{i+1} \\ X_{i+2} \\ X_{i+3} \end{bmatrix} \quad , \quad Y(s_{i,u}) = \begin{bmatrix} u^3 & u^2 & u^1 & 1 \end{bmatrix} M \begin{bmatrix} Y_i \\ Y_{i+1} \\ Y_{i+2} \\ Y_{i+3} \end{bmatrix} \tag{5.22}$$

Here, $u \in [0,1]$, and the coefficient matrix M and the parameters are

$$M = \frac{1}{6} \begin{bmatrix} -1 & 3 & -3 & 1 \\ 3 & -6 & 3 & 0 \\ -3 & 0 & 3 & 0 \\ 1 & 4 & 1 & 0 \end{bmatrix} \tag{5.23}$$

$$s_{i,u} = \frac{i-1+u}{N} \tag{5.24}$$

In eq. (5.24), $1 \le i \le N$, the continuous curve with $s \in [0,1]$ is divided into N segments and the i th segment is defined $s_{i,u}$ [35] . The local deformation of

---

[35] Note that $s_{i,u} \in \left[\frac{i-1}{N}, \frac{i}{N}\right]$ and $\bigcup_{i=1}^{N} \left[\frac{i-1}{N}, \frac{i}{N}\right] = [0,1]$

cubic spline is evidently defined by four control points of the i_{th} segment. To close the cubic B spline curve, the knot points which are the starting point and the end point need to be connected or clamped. For more detailed properties and theory of cubic B-spline, please refer to the book edited by Ahlberg et al. (Ahlberg, Nilson et al. 1972).

With this cubic B-spline representation as the internal energy of snake, we can now utilize it for delineating the contour. Suppose there is a cubic S-spline $(x(s), y(s))$, $s \in [0,1]$, the energy functional of cubic B-spline snake is written as

$$E_{sp} = -\int_0^1 f\left(X\left(s\right), Y\left(s\right)\right) ds \tag{5.25}$$

f denotes the external force as described in the previous section. The internal energy is now implicitly contained within the energy functional eq. (5.25) because of the C^2 class smoothness of cubic B-spline. The discrete representation of N segments is then obtained as

$$E_{sp} = -\sum_{i=1}^{N} \int_{\frac{i-1}{N}}^{\frac{i}{N}} f\left(X\left(s_{i,u}\right), Y\left(s_{i,u}\right)\right) ds_{i,u} \tag{5.26}$$

Substituting eq. (5.24), we eventually have

$$E_{sp} = -\sum_{i=1}^{N} \int_{0}^{1} f\left(X\left(\frac{i-1+u}{N} \right), Y\left(\frac{i-1+u}{N} \right) \right) du \tag{5.27}$$

Now eq. (5.27) can be solved directly by the gradient decent method since E_{sp} is simply a function of control points. Thus,

$$X_i^{\tau+1} = X_i^{\tau} - \delta t \frac{\partial E_{sp}}{\partial X_i} \tag{5.28}$$

$$Y_i^{\tau+1} = Y_i^{\tau} - \delta t \frac{\partial E_{sp}}{\partial Y_i} \tag{5.29}$$

Here, τ and $\tau+1$ are two consecutive iterations with a time step of δt. With a suitable time step the iteration of eq. (5.28) and eq. (5.29) will approach the energy minimization.

One of objectives in this research is to dynamically track the evolution of laser-induced cavitation bubble by delineating the variation of bubble contour during its life-cycle. This type of bubbles in static water usually expand and collapse in an axisymmetry way[36] that is the bubble remains either sphere

[36] The laser beam direction is usually the axis during the phase of growth whereas the axis during the phase of collapse is often perpendicular to the boundary wall.

mostly in the case of infinite space or spheroid often with nearby boundaries. Consequently, affine snake that deforms its shape (active contour) through the affine transformation (Mukherjee and Acton 2007) with EGVF field is thus employed for our application. With this transformation we only need to track six parameters of affine transformation instead of tracking all the snaxels. Therefore, the entire transformation of arbitrary shape can be captured by only six parameters of affine transformation. Supposing a point (x', y') in two-dimensional space under the affine transformation, the new position of the point (x', y') is

$$\begin{bmatrix} x \\ y \end{bmatrix} = \begin{bmatrix} a & b \\ c & d \end{bmatrix} \begin{bmatrix} x' \\ y' \end{bmatrix} + \begin{bmatrix} t_x \\ t_y \end{bmatrix} \tag{5.30}$$

where (t_x, t_y) represents translation, and the matrix $\begin{bmatrix} a & b \\ c & d \end{bmatrix}$ represents rotation, scaling, and shearing. These six parameters are the parameters of affine transformation.

To delineate contour by affine snake, the following energy functional needs to be minimized.

$$E\left(\{X_i, Y_i\}_{i=1}^{N}\right) = -\frac{1}{N}\sum_{i=1}^{N} f\left(X_i, Y_i\right) \tag{5.31}$$

Again, one can use the gradient decent method to solve eq. (5.31) but suffers the pain of numerical instability. Alternatively, we can solve the affine transformation by least square method. Supposing the positions of contour at the iteration number τ are $\left\{X_i^{\tau}, Y_i^{\tau}\right\}_{i=1}^{N}$ and the predicted contour positions of target computed by gradient decent method are $\left\{X_i', Y_i'\right\}_{i=1}^{N}$, the curve $\left\{X_i^{\tau}, Y_i^{\tau}\right\}_{i=1}^{N}$ which undergoes the affine transformation to the new position $\left\{X_i', Y_i'\right\}_{i=1}^{N}$ can be written as

$$\begin{bmatrix} a & b \\ c & d \end{bmatrix}\begin{bmatrix} X_i^{\tau} \\ Y_i^{\tau} \end{bmatrix} + \begin{bmatrix} t_x \\ t_y \end{bmatrix} = \begin{bmatrix} X_i' \\ Y_i' \end{bmatrix} \tag{5.32}$$

By using the least square method to solve eq. (5.32), the parameters of affine transformation $\left(t_x, t_y, a^*, b^*, c^*, d^*\right)$ can be obtained. The position $\left\{X_i^{\tau}, Y_i^{\tau}\right\}_{i=1}^{N}$ is then updated to $\left\{X_i^{\tau+1}, Y_i^{\tau+1}\right\}_{i=1}^{N}$ as

$$\begin{bmatrix} a^* & b^* \\ c^* & d^* \end{bmatrix}\begin{bmatrix} X_i^{\tau} \\ Y_i^{\tau} \end{bmatrix} + \begin{bmatrix} t_x^* \\ t_y^* \end{bmatrix} = \begin{bmatrix} X_i^{\tau+1} \\ Y_i^{\tau+1} \end{bmatrix} \tag{5.33}$$

This iteration stops when the solution attains the minimum energy where there is no appreciable change in contour delineation between the previous

and current frames. For more detail on the active contour method and its tracking approaches, the readers are referred to the books by Acton and Ray (Acton and Ray 2006, Acton and Ray 2009).

Based on the previous discussion on active contour methods a Matlab program originally developed by Ray et al. (Ray, Ahmetovic et al. 2010) used for tracking metal droplet has been significantly modified and further developed to meet our sophisticated application for detecting the extremely fast changing and tiny contours of cavitation bubbles from a temporal series of high-speed video images. The snake-based approach in the program is specifically designed for minimizing manual controls but maximizing automations. The user is prompted to click only one point inside the interior area of target as the original point of initial contour to start the program. Furthermore, the self-adjusting approach on tracking the bubble contours is employed in the modified codes for achieving high accuracy in tracking of various cases. This is briefly explained below. The evolution of cavitation bubble throughout its life cycle experiences a vast volume-change. For these bubble images captured by high speed camera, its maximum radius could be

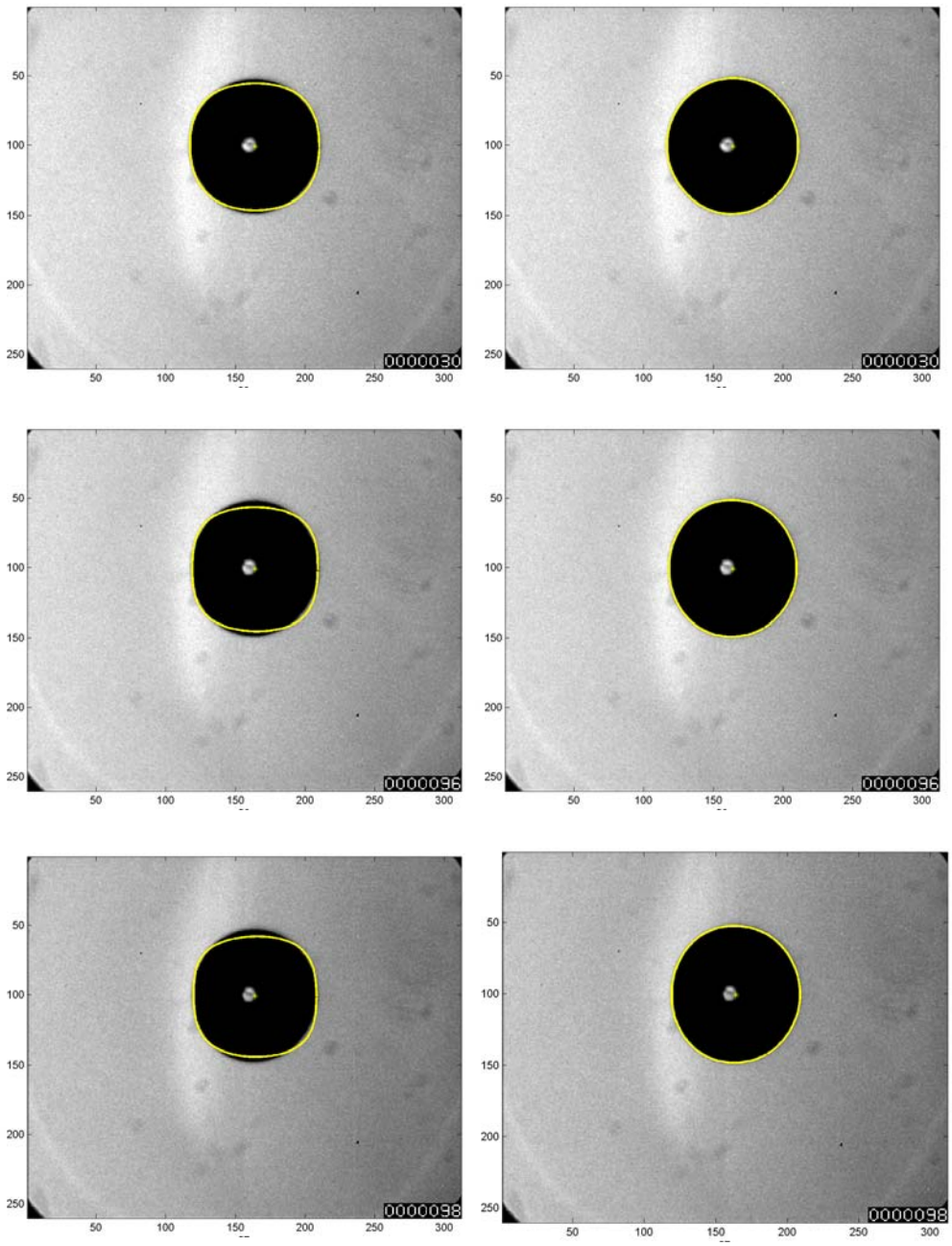

Fig. 5.1 Cavitation bubble tracking without and with adpative approach

easily several hundred times of its initial radius[37]. This is one of major differences comparing with the use of active contour method for tracking

[37] The initial radius refers to the radius of bubble in the first tracked image.

image contour in other fields[38]. Therefore, a self-adjusting approach for assigning the initial contours is essential for tracking cavitation bubbles accurately and correctly. Figure 5.1 shows the results of tracking cavitation bubble with and without self-adjusting approach. In the left hand side, these images tracked without self-adjusting approach show the failure of tracking because the size of initial contour is fixed and becomes too small when the bubble grows large. In contrast, the images of right hand sides show perfect tracking owing to the self-adjusting approach.

In our application, the EGVF field is chosen as the external force to guide the active contour. As for the internal energy, the affine snake is firstly used to delineate the contour of target followed by the cubic B-spline snake to refine the contour. Once the tracking is done, the data of bubble contours against time are obtained. This set of data is essential for extracting substantial information of bubble dynamics. For example, we can calculate accurately the volume of bubble and further analyse quantitatively those physical

[38] The target of interest usually remains more or less the same order of size during its evolution being tracked.

characteristics relating to the volumetric variations. These results can be used either to validate the existing theories or to discover unknown. The calculation of volume of bubble can be implemented as follows. The data of active contour of bubble is fitted to a series of polynomial equations (or Fourier equations). With the assumption of bubble virtually remaining axisymmetry during its movement and evolution, its volume can be calculated by shell method for the solid of evolution. Supposing a closed curve $y = f(x)$, $x \in [a,b]$ rotating along its y axis, the volume of the solid of revolution is

$$Volume = 2\pi \int_a^b xf(x)dx \tag{5.34}$$

5.5 Demonstrations of Tracking Cavitation Bubble

In this section, we demonstrate some typical examples of contour tracking by the affine snake with EGVF field for various bubbles investigated by us, noting that all the high-speed photographic images are not pre-processed by any image enhanced techniques.

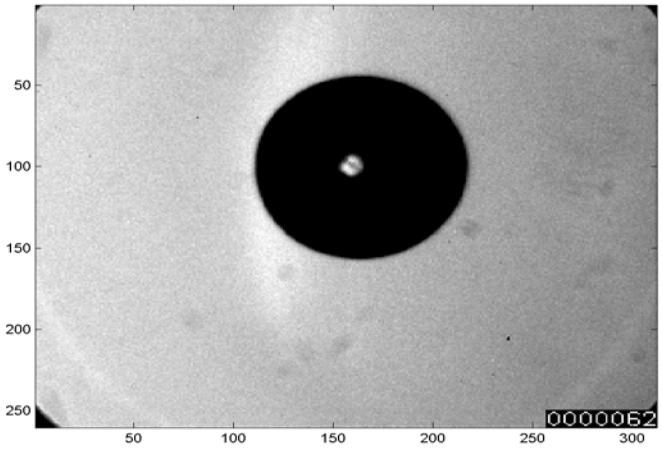

Fig. 5.2 Example of spherical cavitation bubble image

Firstly, we use a spherical cavitation bubble as a example to illustrate the robustness of this method. Figure 5.2 shows one frame of the video images that is a spherical cavitation bubble captured by Shimadzu HPV-1. To detect the contour of the bubble, an initial circle is assigned as the initial active contour by clicking a user-interactive point arbitrarily inside the image of bubble. From Fig. 5.3 it can be seen that no matter where the initial active contour is assigned within the image even on the edge of bubble, the robustness of this method is evidently demonstrated by tracking the bubble contour quickly. The evolution of initial contour is shown as a series of contours in red colour starting from the smallest circle where the initial contour has been assigned by the user.

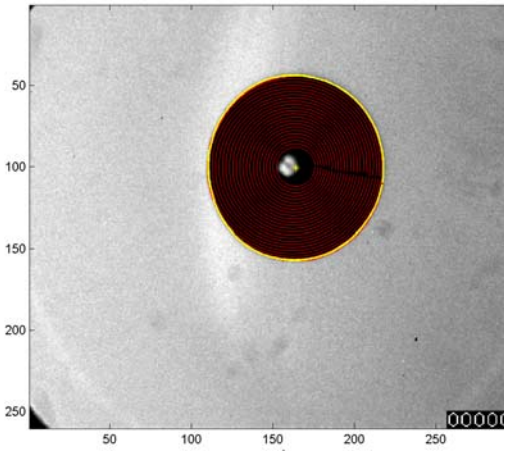

Fig. 5.3a The initial contour assigned at the centre.

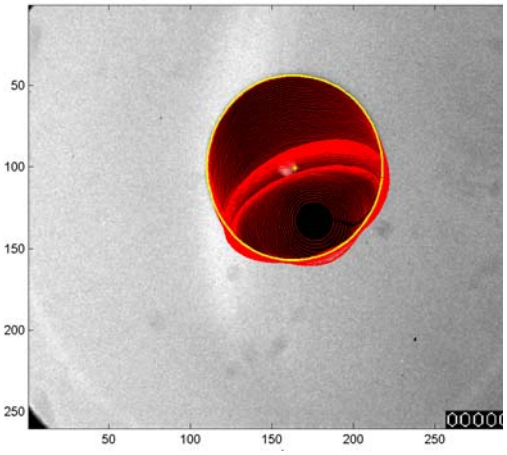

Fig. 5.3b The initial contour assigned in lower right part of bubble.

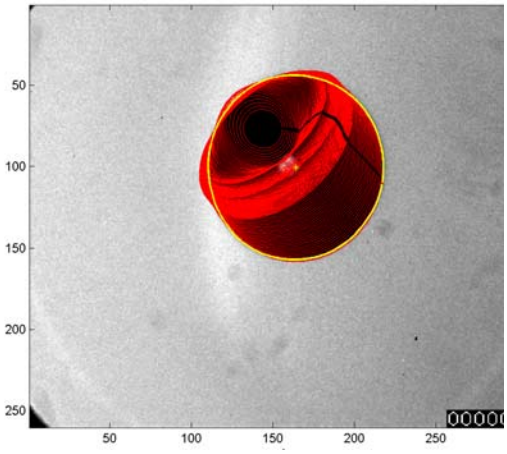

Fig. 5.3c The initial contour assigned in upper left part of bubble.

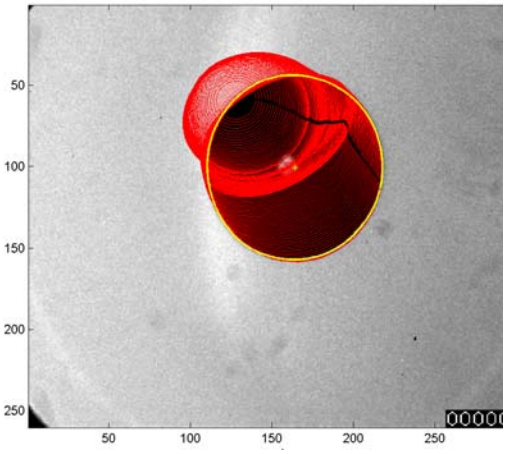

Fig. 5.3d The initial contour assigned on edge of bubble.

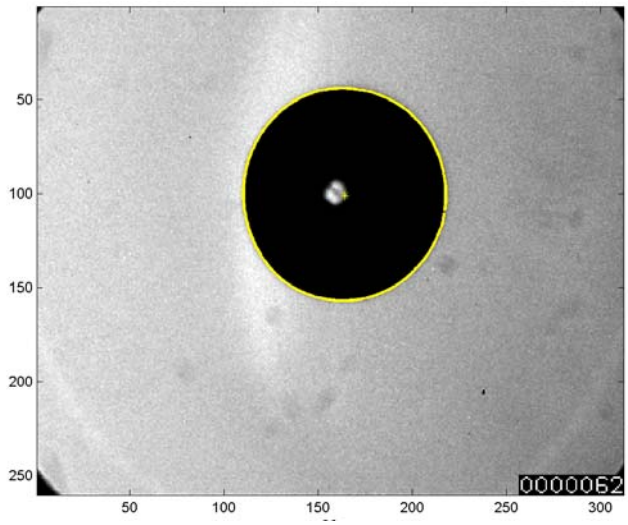

Fig. 5.4 Contour delineation of cavitation bubble

The final tracked contour is displayed in yellow and the geometric centre of this contour is marked by asterisk symbol as shown in Fig. 5.4. All the bubble contours are perfectly delineated by affine snake with EGVF field. The robustness of this method could be further understood from the characteristics reflected by the vector field of EGVF field of bubble image shown in Fig. 5.5a.

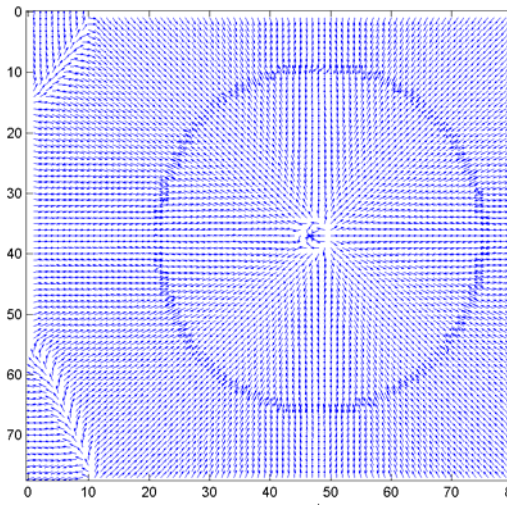

Fig. 5.5a The vector field of EGVF

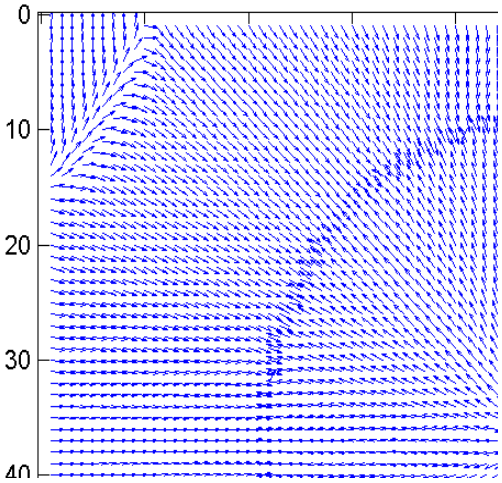

Fig. 5.5b Zoom-in of upper left part of figure

The targeted contour of bubble in the vector field is delineated as the darker-blue ring formed by the clusters of vectors. The centre is the location where the initial contour is assigned. Noting that the initial contour is not necessarily to be assigned at the centre owing to the Dirichlet boundary condition of EGVF field demonstrated by Fig. 5.3. The initial contour, once

assigned, is either pushed forward or pulled back toward the edge of bubble under the driving force of EGVF field in order to achieve the minimum energy. Figure 5.5b is the zoom-in of image that clearly shows the nearby vectors are directed toward the edge of bubble either from the inside or from the outside of the edge.

With this effective tool of image segmentation, a series of bubble images taken by the ultra-high speed camera can be tracked and delineated at one go. This will, for the first time, enable the researchers to quickly and quantitatively analyse experimental results in the form of enormous bubble images captured by high speed photography. Next we will use a few typical cases of laser-induced cavitation bubbles, either spherical or non-spherical, to demonstrate the ability and efficiency of this tracking approach modified and further developed from our studies. In the first case, a spherical cavitation bubble with $R_m \approx 0.7033$ mm is tracked. This type of laser-induced cavitation bubbles is usually generated in the free space. Owing to the similarity, only a part of tracked results is shown here. In Fig. 5.6, bubble contours with 1 μs time interval is tracked as the bubble outgrows the illumination of plasma. The pictures are read from left to right and then up to

down in sequence. The plasma is still bright enough to be seen clearly in the first three frames of Fig. 5.6. As the plasma disappears, the bubble becomes more spherical during its expansion. Clearly, this method tracks the cavitation bubble successfully, even under the uneven illumination of image.

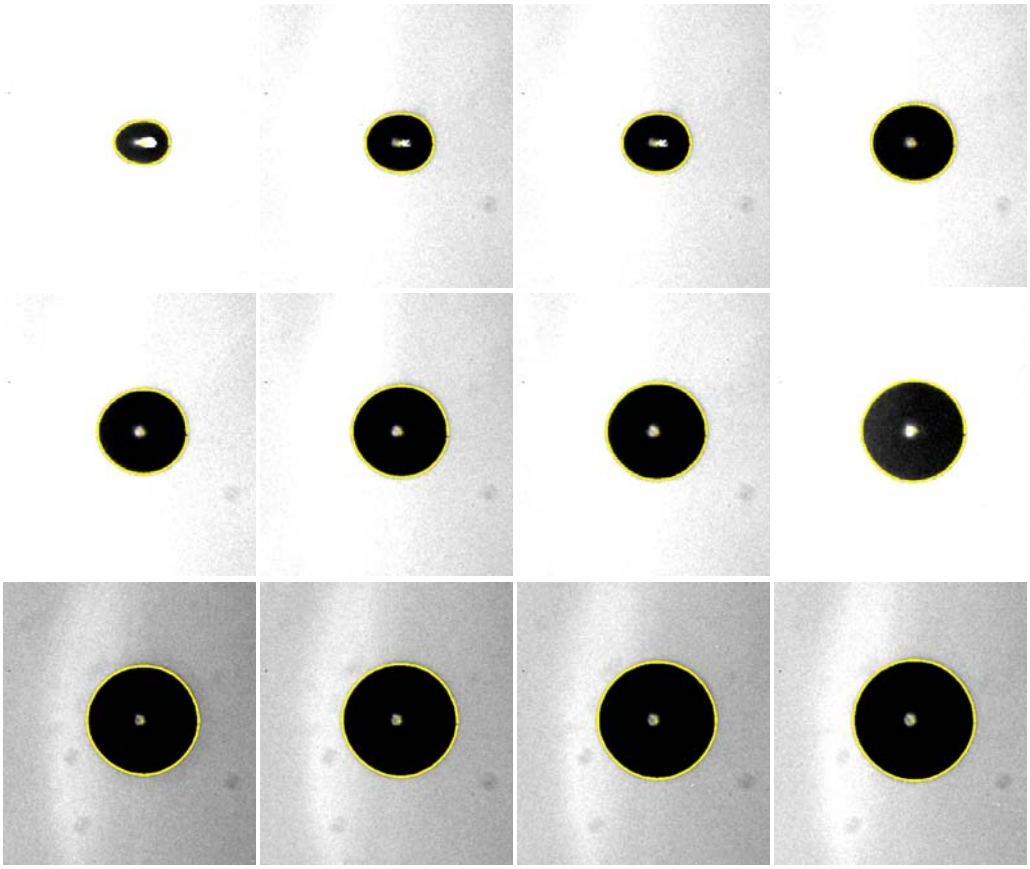

Fig. 5.6 The evolution of bubble at the first 12 microsecond after the bubble outgrows plasma

In Fig. 5.7, the collapse phase of spherical cavitation bubble is shown. Here, only the last few tracked images where the change of bubble images is fastest are displayed. The frames are arranged as 2 μs intervals. The images

captured during the final stage of bubble collapse are often very difficult to track. This is because the violently rapid collapse of bubble challenges the limit of high speed camera demanding a temporal resolution in the range of nanosecond. Whereas this is often compromised by the requirement of high space resolution. Thus, either a lower temporal resolution or a lower spatial resolution or a combination of both causes the failure of tracking. If the spatial resolution is sacrificed, the bubble-image tracking will deteriorate in accuracy and successful rate as the bubble image may consist of only a few pixels.

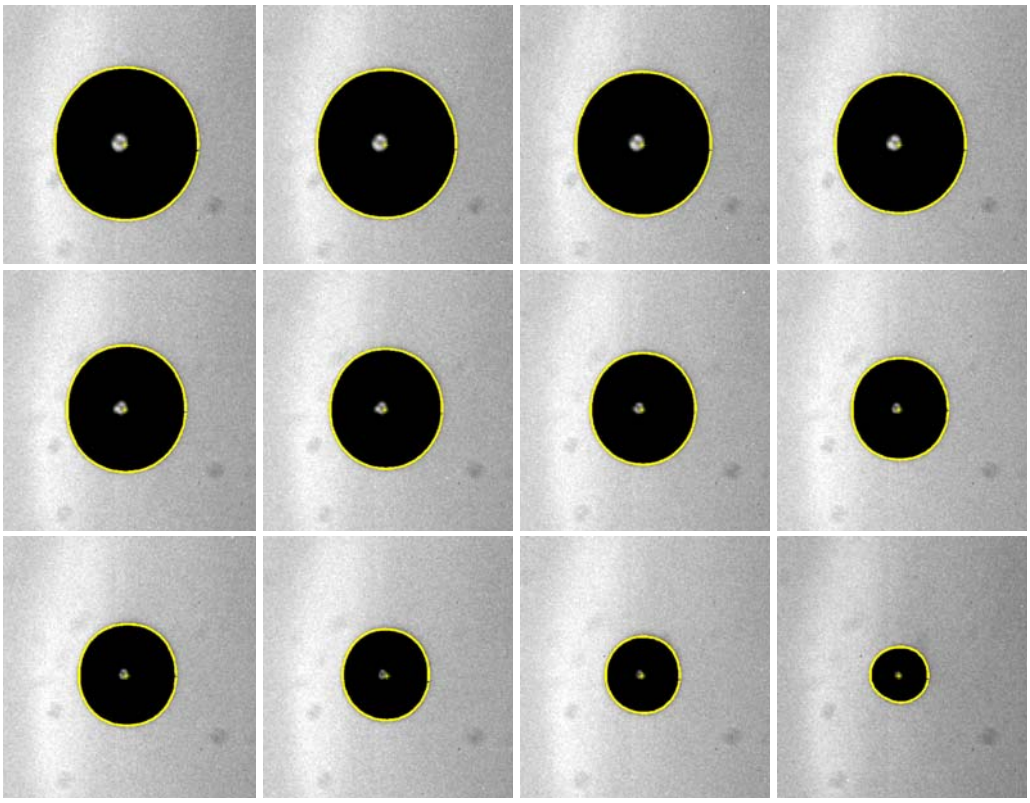

Fig. 5.7 The collapse of spherical bubble with $R_m \approx$ 0.7033 mm in the last stage

For the cases of non-spherical cavitation bubble, there are more interesting diverse variations of bubble shape that presents real challenge to the contour tracking. The non-spherical cavitation bubble is usually observed in the asymmetric environment where bubble interacts with nearby boundaries such as (soft or rigid) wall boundaries and free surface etc. Behaviours different from symmetrical collapse can be observed during bubble first collapse with these nearby boundaries. These behaviours are usually characterized by a stand-off parameter γ which is defined as the ratio of the distance between the initial bubble centre and the boundary surface to the maximum bubble radius R_m. Here, we demonstrate a few typical cases of non-spherical cavitation bubble with different values of γ tracked by affine snake with EGVF field. Figure 5.8 shows the collapse characteristics of bubble with $R_m \approx 0.6$ mm and $\gamma \approx 1.8$ near a rigid boundary where the wall is appeared as the dark long strip in the bottom of each frames. The cavitation bubble is in its last stage of first collapse. The time interval between frames is 2 μs. The bubble contours as shown are tracked successfully and accurately, though the active contour seems a little insensitive to the change in the last frame where the bubble shape is slightly concave. The reason that causes this

slight mismatch is mainly attributed to the low spatial resolution in that particular area of the image which contains only a few pixels[39].

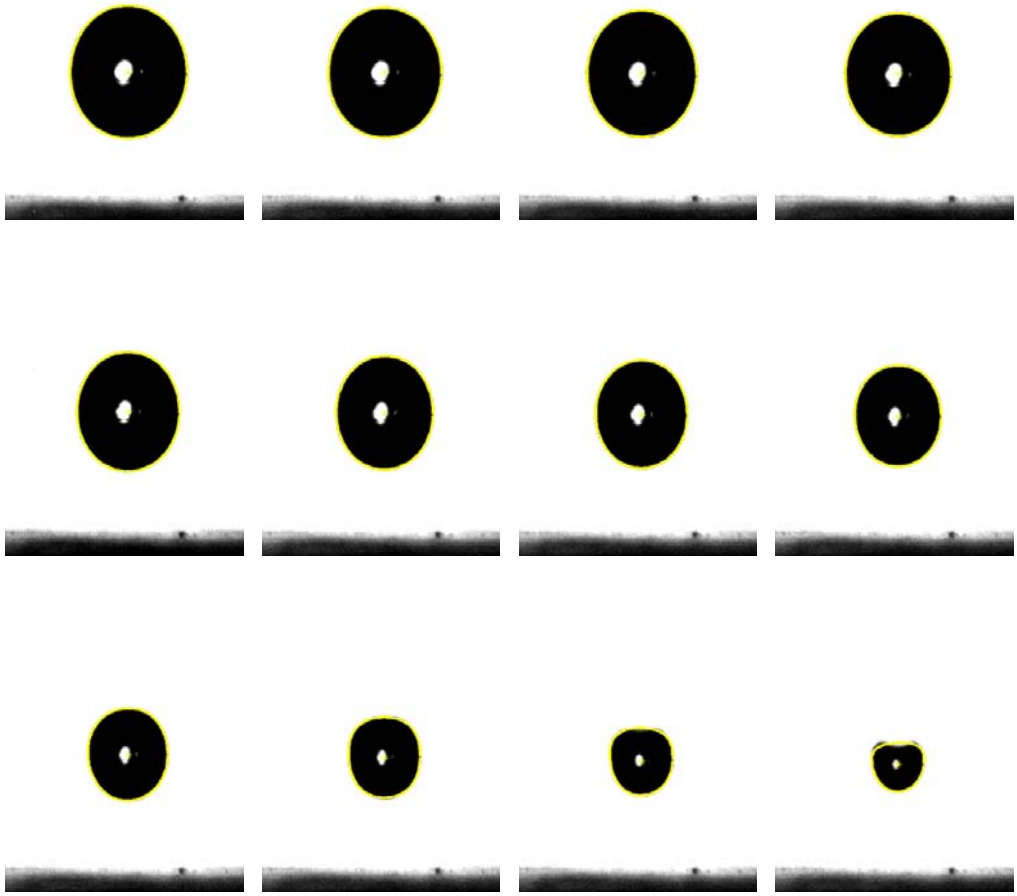

Fig. 5.8 The non-spherical bubble nearby rigid wall with $R_m \approx$ 0.6 mm and $\gamma \approx$ 1.8

Figure 5.9 shows another case of bubble collapse close to a rigid wall with $R_m \approx$ 0.5 mm, $\gamma \approx$ 1.2, and frame interval of 2 μs. The contours of

[39] The image magnification of objective lens on the long distance microscope used for the demonstration was not high enough. Further improvement can be achieved once a higher performance objective lens is employed.

bubble are correctly tracked and delineated when the bubble is placed very close to the wall boundary. Apart from the case of bubble interacting with rigid wall, the case of cavitation bubble interacting with nearby elastic wall boundary is also tested, which demonstrates very different characteristics in term of bubble shape and dynamics.

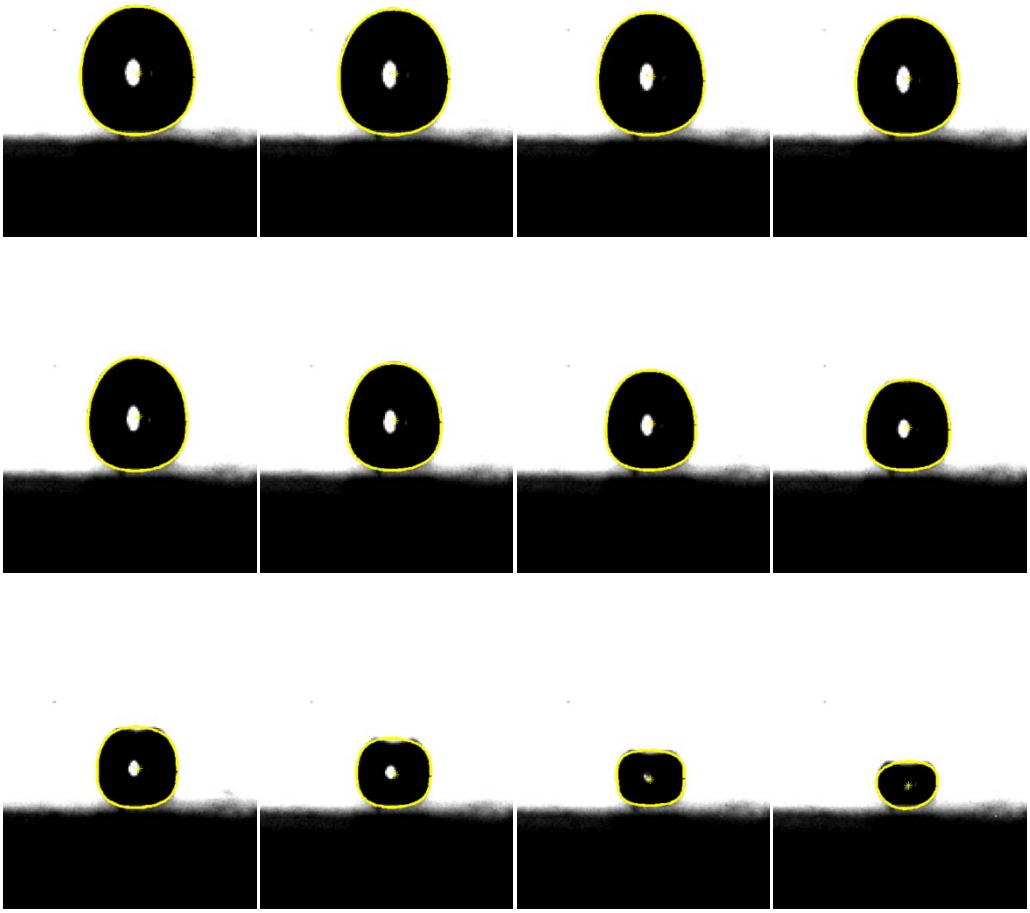

Fig. 5.9 The non-spherical bubble near rigid wall with $R_m \approx$ 0.5 mm and $\gamma \approx$ 1.2

Figure 5.10 is such a non-spherical bubble with $R_m \approx$ 0.475 mm close to an elastic wall boundary at $\gamma \approx$ 1.2.

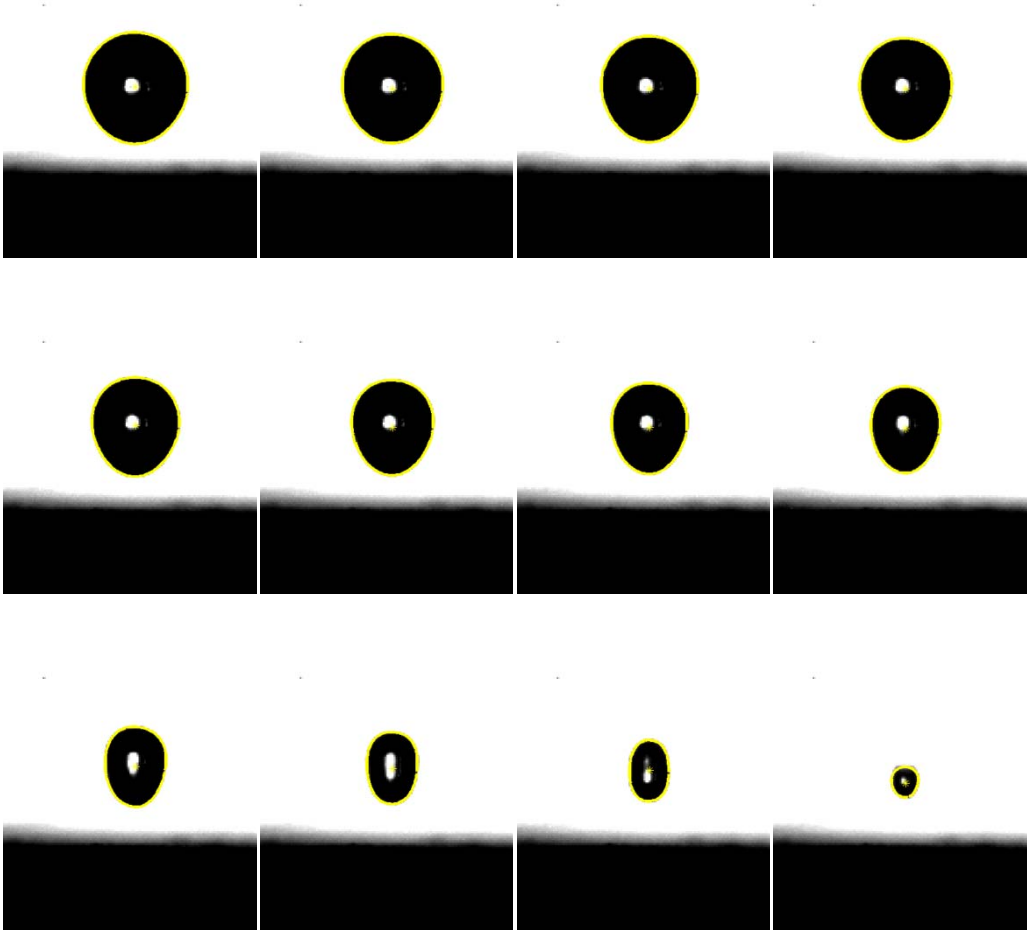

Fig. 5.10 The non-spherical bubble near an elastic wall with $R_m \approx$ 0.475 mm and $\gamma \approx$ 1.3

Figure 5.11 shows another example of non-spherical bubble close to an elastic wall with $R_m \approx$ 0.633 mm and $\gamma \approx$ 1.07. The time interval is 4 μs between each frame. These two cases show a fundamental difference in term of bubble shape variation compared with the case of a nearby rigid wall. Therefore, it is essential for researches to acquire these contour variations correctly and quantitatively for further investigating their distinguishing

dynamics against the properties of boundary walls.

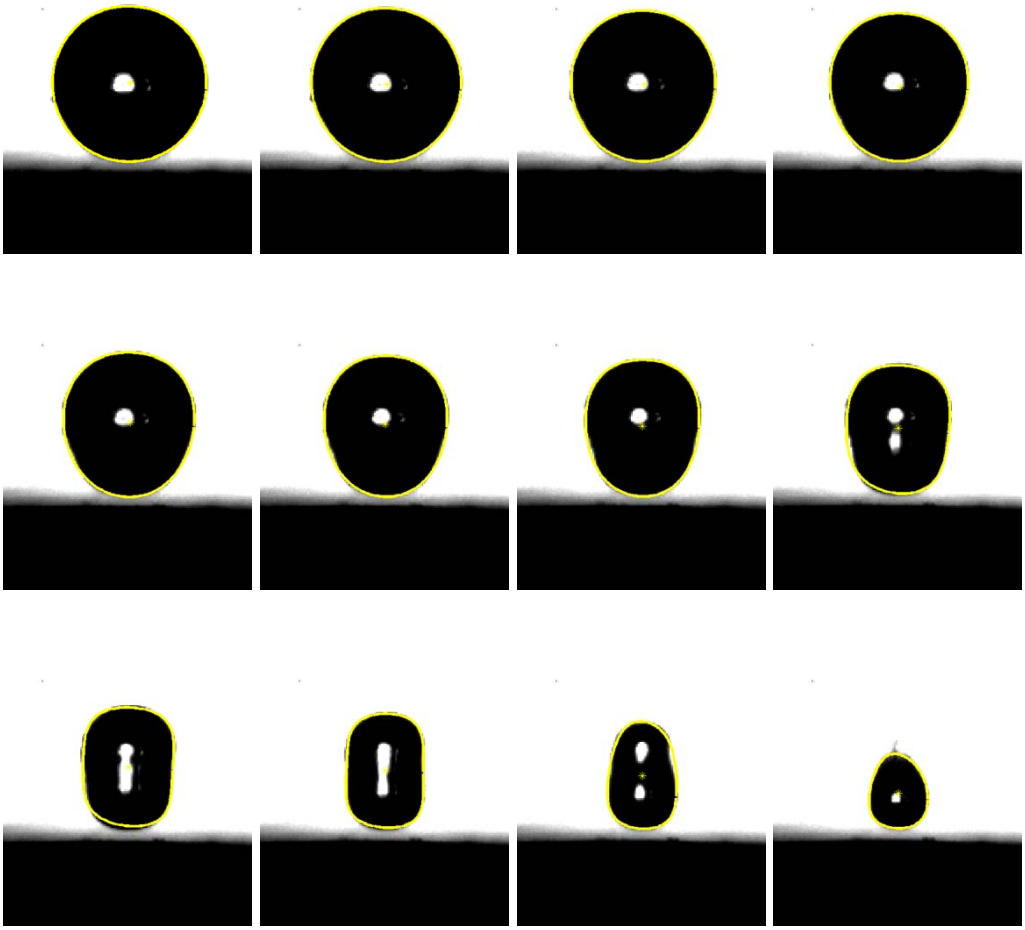

Fig. 5.11 The non-spherical bubble near an elastic wall with $R_m \approx$ 0.633 mm and $\gamma \approx$ 1.07

The last case to demonstrate is a bubble interacting with a free surface, e.g. air/liquid interface. Figure 5.12 shows the last stage of first collapse of bubble close to the free surface where the dark bar is observed. The frame interval is 2 μs . The bubble with $R_m \approx$ 0.55 mm is generated just under the water surface with $\gamma \approx$ 1.2. In short, the shape variation of bubble is

accurately delineated by affine snake with EGVF field.

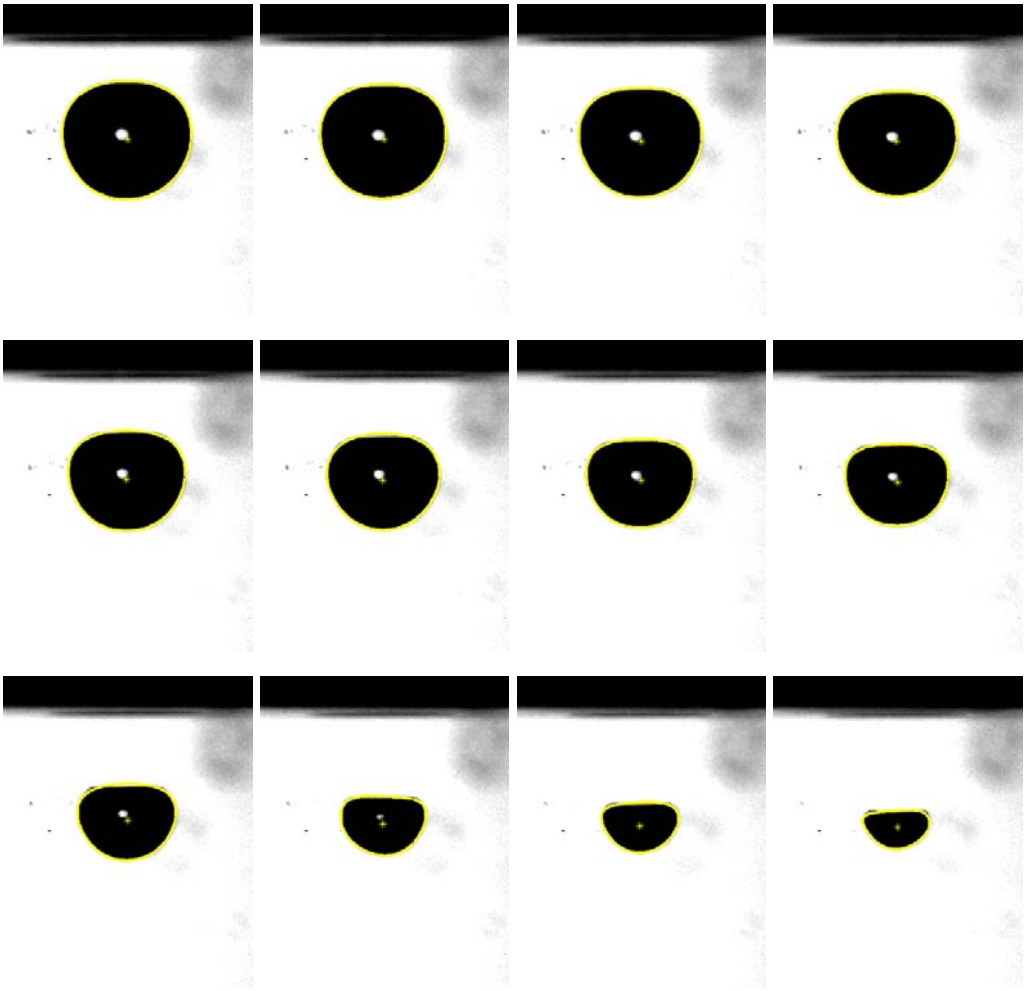

Fig. 5.12 The non-spherical bubble near a free surface with $R_m \approx 0.55$ mm and $\gamma \approx 1.2$

Except for the limitation caused by the availability and capability of instruments as mentioned previously, another disadvantage of this tracking method is the trackable image currently limited to the first cycle of growth and collapse of bubble. This is because of the infinitesimal volume at the collapse point that causes the crash of the program. Therefore, in order to

completely track the bubble oscillation, the programming needs to be further refine to avoid this singularity problem combining with increasing the image resolution around this point.

5.6 Summary

A much more effective active contour method, affine snake with EGVF field, has been purposely further developed to meet the challenging requirements of studying spherical and non-spherical cavitation bubbles. The study has also for the first time demonstrated the possibility of applying this approach to the tracking of spherical and non-spherical bubble images. This method developed through this PhD programme shows the ability of dynamically tracking and acquiring various contours of bubble automatically. Through the above demonstrating cases including spherical and non-spherical cavitation bubbles, the wide applicability of the affine snake with EGVF field for bubble contour delineation is assured. This powerful tool will greatly benefit the study of bubble dynamics by using high speed photography as already shown in our own studies presented in the preceding chapter of this thesis.

Chapter 6

Conclusions and Future Work

6.1 Conclusions

The achievements of this PhD study are summarized as follows:

1. Applied and validated a suitable numerical approach for simulating rectangular microchannel across the entire flow regimes including the laminar, transitional and fully turbulent flows. With the help of this numerical approach combined with micro-PIV, the long lasting gap for studying the turbulence transition for micro-channels, can be solved properly.

2. Applied this numerical approach further with scalar dispersion for simulating continuous-flow micro-mixers and for establishing a set of design criteria. This numerical approach thus provides a fast and efficient way for investigating the rapid mixing in micro-mixer used for

bio-medical applications, in particular for the given task of protein folding.

3. Established an experimental facility together with procedures for investigating laser-induced cavitation micro-bubbles in various environments including in the free-space, with the nearby free-surface, rigid and soft wall boundaries. Having done the calibration of this facility using an available high speed video-camera, the cavitation bubbles to be generated for observation can be controlled as small as around 200 μm in its maximum radius. This provides a feasible approach to study the cavitation erosion in microscale. This versatile facility can also serve as a general platform for micro-bubble studies. It is thus being used by another doctorial student for investigating the behaviours of cavitation micro-bubbles in non-Newtonian fluids with nearby visco-elastic wall boundaries.

4. Developed a self-adjusting active contour method, affine snake with EGVF field, for tracking the cavitation bubble contour dynamically and

semi-automatically. This novel method has also been demonstrated by using laser generated micro-bubbles from the facility developed by this PhD programme. This approach is for the first time applied to the study of cavitation bubbles. It provides more accuracy and reliability in tracking cavitation bubbles.

5. Perform experimental study of laser-induced micro-bubbles by using high speed video camera. Typical cases of laser-induced cavitation bubbles are demonstrated and characterised quantitatively for the first time by utilising the proposed active contour method. It shows the potential of this method. By combining with high speed photography, it provides a quantitative method for characterizing the global behaviours of cavitation bubbles, in particular in micro-scale, which is not available before. This technique is particularly useful for studying the shape instability during bubble collapse and growth.

6.2 Future works

This PhD study, according to its designated objectives, is mainly to

investigate new approach and tool for studying key fluid topics involved in developing the next-generation of continuous-flow micromixer. This study has completed successfully and set up a framework for such a purpose. By using the knowledge and novel techniques developed from this PhD programme in the relevant fields, many opportunities for advanced study can be followed as below.

1. Further calibrating the transitional turbulence model, using either experimental results from pressure drop and micro-PIV methods or numerical results from large eddy and direct numerical simulations, can provide more reliable empirical formula for this turbulence modelling and thus enhance its adaptability.

2. The numerical approach using the transitional turbulence model for investigating the micromixer for rapid mixing will be further tested and validated with the prototype test facility established by the collaborative partner of the biological department. This numerical approach will be

able to serve the design and the analysis of the newly developed continuous-flow micromixer in the future.

3. The experimental facility established through this PhD study will serve as a research platform for advanced studies on the erosion of microscale cavitation in the future. This experimental setup is designed to accommodate various types of microchannel and microfluidic device. The cavitation micro-bubbles and its microscale behaviours in such tiny and confined environment will be further studied by using this facility in the future.

4. Due to the nature of rapid mixing in continuous-flow micromixer, cavitation bubbles are very likely to occur as explained before. In order to design the next generation micromixer, the phenomenon of cavitation inside micromixer will be considered and further investigated in the cavitation research group at the school of engineering by using the knowledge and facilities developed by this PhD programme together with the collaborative partner of the biological department.

5. By utilising the active contour method proposed, the subtle effects of surface tension and viscosity in micro-bubbles will be investigated in the future. Also, the active contour method itself will also be advanced and improved further for those cases of cavitation bubble collapsed onto the wall boundaries in which the variations of contact angle of liquid/vapour interface can be tracked dynamically. This method as demonstrated will be a powerful tool for quantitatively studying the dynamics of cavitation bubble.

6. The interaction between cavitation bubble and the free surface (i.e. air/liquid interface) also exhibits a variety of interesting behaviours in terms of the surface variation and water jet. By integrating another high speed camera into our experimental setup, these behaviours can be possibly observed and studied simultaneously with cavitation bubble

Bibliography

Abraham, J. P., E. M. Sparrow and J. C. K. Tong (2008). "Breakdown of laminar pipe flow into transitional intermittency and subsequent attainment of fully developed intermittent or turbulent flow." Numerical Heat Transfer Part B-Fundamentals **54**(2): 103-115.

Abraham, J. P., E. M. Sparrow and J. C. K. Tong (2009). "Heat transfer in all pipe flow regimes: laminar, transitional/intermittent, and turbulent." International Journal of Heat and Mass Transfer **52**(3-4): 557-563.

Abraham, J. P., E. M. Sparrow and W. J. Minkowycz (2011). "Internal-flow Nusselt numbers for the low-Reynolds-number end of the laminar-to-turbulent transition regime." International Journal of Heat and Mass Transfer **54**(1-3): 584-588.

Abraham, J. P., E. M. Sparrow, J. C. K. Tong and D. W. Bettenhausen (2010). "Internal flows which transist from turbulent through intermittent to laminar." International Journal of Thermal Sciences **49**(2): 256-263.

Acton, S. T. and N. Ray (2006). "Biomedical Image Analysis: Tracking." Synthesis Lectures on Image, Video, and Multimedia Processing **2**(1): 1-152.

Acton, S. T. and N. Ray (2009). "Biomedical Image Analysis: Segmentation." Synthesis Lectures on Image, Video, and Multimedia Processing **4**(1): 1-108.

Adrian, R. J. (1991). "PARTICLE-IMAGING TECHNIQUES FOR EXPERIMENTAL FLUID-MECHANICS." Annual Review of Fluid Mechanics **23**: 261-304.

Ahlberg, J. H., E. N. Nilson and J. L. Walsh (1972). The Theory of

splines and their applications, Acad. Press.

Anderson, J. D. (1995). Computational fluid dynamics : the basics with applications. New York ; London, McGraw-Hill.

Ashar Sultan, M., C. P. Fonte, M. M. Dias, J. C. B. Lopes and R. J. Santos (2012). "Experimental study of flow regime and mixing in T-jets mixers." Chemical Engineering Science **73**: 388-399.

Bakunin, O. G. (2008). Turbulence and Diffusion. Berlin ; Heidelberg, Springer-Verlag.

Barnaby, S. W. and S. J. Thornycroft (1895). "Torpedo-boat Destroyers." Proc. Inst. Civ Eng. **122**: 51-103.

Batchelor, G. K. (2000). An introduction to fluid dynamics. Cambridge, Cambridge University Press.

Berger, R. L., B. Balko and H. F. Chapman (1968). "High Resolution Mixer for the Study of the Kinetics of Rapid Reactions in Solution." Review of Scientific Instruments **39**(4): 493-498.

Bilsel, O., C. Kayatekin, L. A. Wallace and C. R. Matthews (2005). "A microchannel solution mixer for studying microsecond protein folding reactions." Review of Scientific Instruments **76**(1): 014302-014307.

Bird, R. B., W. E. Stewart and E. N. Lightfoot (2007). Transport phenomena. New York ; Chichester, J. Wiley.

Blake, J. R., P. B. Robinson, A. Shima and Y. Tomita (1993). "Interaction of two cavitation bubbles with a rigid boundary." Journal of Fluid Mechanics **255**: 707-721.

Bockhorn, H., D. Mewes, W. Peukert and H. J. Warnecke (2010). "Micro and Macro Mixing: Analysis, Simulation and Numerical Calculation." Micro and Macro Mixing: Analysis, Simulation and Numerical

Calculation: 1-347.

Bokenkamp, D., A. Desai, X. Yang, Y. C. Tai, E. M. Marzluff and S. L. Mayo (1998). "Microfabricated silicon mixers for submillisecond quench-flow analysis." Anal. Chem. **70**(2): 232-236.

Bothe, D., C. Stemich and H.-J. Warnecke (2008). "Computation of scales and quality of mixing in a T-shaped microreactor." Computers & Chemical Engineering **32**(1-2): 108-114.

Brigger, P., J. Hoeg and M. Unser (2000). "B-spline snakes: a flexible tool for parametric contour detection." Image Processing, IEEE Transactions on **9**(9): 1484-1496.

Britton, C. (1940). "The accelerated flow method for rapid reactions." Journal of the Franklin Institute **229**(6): 737-766.

Bruus, H. (2008). Theoretical microfluidics. Oxford, Oxford University Press.

Carter, A. H. (2001). Classical Statistical Thermodynamics, Prentice Hall.

Chance, B. (1940). "The accelerated flow method for rapid reactions." Journal of the Franklin Institute **229**(4): 455-476.

Chance, B. (1940). "The accelerated flow method for rapid reactions." Journal of the Franklin Institute **229**(6): 737-766.

Chance, B. (1964). Rapid mixing and sampling techniques in biochemistry; proceedings. New York, Academic Press.

Chung, T. J. (2010). Computational fluid dynamics. Cambridge, Cambridge University Press.

Coussios, C. C. and R. A. Roy (2008). "Applications of Acoustics and Cavitation to Noninvasive Therapy and Drug Delivery." Annual Review

of Fluid Mechanics **40**(1): 395-420.

Cussler, E. L. (2009). Diffusion : mass transfer in fluid systems. Cambridge ; New York, Cambridge University Press.

Danckwerts, P. V. (1958). "The effect of incomplete mixing on homogeneous reactions." Chemical Engineering Science **8**(1–2): 93-102.

Dougherty, G. (2009). Digital image processing for medical applications. Cambridge ; New York, Cambridge University Press.

Durbin, P. A. and B. A. P. Reif (2001). Statistical theory and modeling for turbulent flows. Chichester, Wiley.

Elsnab, J. R., D. Maynes, J. C. Klewicki and T. A. Ameel (2010). "Mean flow structure in high aspect ratio microchannel flows." Experimental Thermal and Fluid Science **34**(8): 1077-1088.

Elsnab, J., J. Klewicki, D. Maynes and T. Ameel (2011). "Mean dynamics of transitional channel flow." Journal of Fluid Mechanics **678**: 451-481.

Felix, M. P. and A. T. Ellis (1971). "Laser-Induced Liquid Breakdown-a Step-By-Step Account." Applied Physics Letters **19**(11): 484-486.

Gac, S. L., E. Zwaan, A. v. d. Berg and C.-D. Ohl (2007). "Sonoporation of suspension cells with a single cavitation bubble in a microfluidic confinement." Lab on a Chip **7**(12): 1666-1672.

Gibson, Q. H. and L. Milnes (1964). "Apparatus for rapid and sensitive spectrophotometry." Biochem J **91**(1): 161-171.

Gogate, P. R. and A. M. Kabadi (2009). "A review of applications of cavitation in biochemical engineering/biotechnology." Biochemical Engineering Journal **44**(1).

Guo, Z.-Y. and Z.-X. Li (2003). "Size effect on microscale single-phase

flow and heat transfer." International Journal of Heat and Mass Transfer **46**(1): 149-159.

Haaland, S. E. (1983). "SIMPLE AND EXPLICIT FORMULAS FOR THE FRICTION FACTOR IN TURBULENT PIPE-FLOW." Journal of Fluids Engineering-Transactions of the Asme **105**(1): 89-90.

Hao, P. F., X. W. Zhang, Z. H. Yao and F. He (2007). "Transitional and turbulent flow in a circular microtube." Experimental Thermal and Fluid Science **32**(2): 423-431.

Hao, P. F., Z. H. Yao, F. He and K. Q. Zhu (2006). "Experimental investigation of water flow in smooth and rough silicon microchannels." Journal of Micromechanics and Microengineering **16**(7): 1397-1402.

Hartridge, H. and F. J. W. Roughton (1923a). "A Method of Measuring the Velocity of Very Rapid Chemical Reactions." Proceedings of the Royal Society of London. Series A **104**(726): 376-394.

Hartridge, H. and F. J. W. Roughton (1923b). "The Velocity with which Carbon Monoxide Displaces Oxygen from Combination with Hoemoglobin.--Part I." Proceedings of the Royal Society of London. Series B, Containing Papers of a Biological Character **94**(662): 336-367.

Harvey, S., J. Best and W. Soh (1996). "Vapour bubble measurement using image analysis." Measurement Science & Technology **7**(4): 592-604.

Hellman, A. N., K. R. Rau, H. H. Yoon, S. Bae, J. F. Palmer, K. S. Phillips, N. L. Allbritton and V. Venugopalan (2007). "Laser-Induced Mixing in Microfluidic Channels." Analytical Chemistry **79**(12): 4484-4492.

Hertzog, D. E., X. Michalet, M. Jäger, X. Kong, J. G. Santiago, S. Weiss and O. Bakajin (2004). "Femtomole Mixer for Microsecond Kinetic

Studies of Protein Folding." Analytical Chemistry **76**(24): 7169-7178.

Hessel, V., H. Lowe and F. Schonfeld (2005). "Micromixers - a review on passive and active mixing principles." Chemical Engineering Science **60**(8-9): 2479-2501.

Hetsroni, G., A. Mosyak, E. Pogrebnyak and L. P. Yarin (2005). "Fluid flow in micro-channels." International Journal of Heat and Mass Transfer **48**(10): 1982-1998.

Hetsroni, G., A. Mosyak, E. Pogrebnyak and L. P. Yarin (2011). "Micro-Channels: Reality and Myth." Journal of Fluids Engineering **133**(12): 121202-121214.

Ho, C.-M. P. D. (2010). Micro/nano technology systems for biomedical applications : microfluidics, optics, and surface chemistry. Oxford, Oxford University Press.

Iben, U., A. Morozov, E. Winklhoferb and R. Skodaa (2011). Optical investigations of cavitating flow phenomena in micro channels using a nano second resolution. WIMRC 3rd International Cavitation Forum 2011. University of Warwick.

Jiang, X. and C.-H. Lai (2009). Numerical techniques for direct and large-eddy simulations. Boca Raton, Fla., CRC ; London : Taylor & Francis [distributor].

Judy, J., D. Maynes and B. W. Webb (2002). "Characterization of frictional pressure drop for liquid flows through microchannels." International Journal of Heat and Mass Transfer **45**(17): 3477-3489.

Kass, M., A. Witkin and D. Terzopoulos (1988). "Snakes: Active contour models." (4): 321-331.

Kockmann, N. (2008a). "Convective micromixers - Design and industrial applications." Proceedings of the Institution of Mechanical Engineers Part

C-Journal of Mechanical Engineering Science **222**(5): 807-816.

Kockmann, N. (2008b). Transport phenomena in micro process engineering. Berlin ; New York, Springer.

Kohl, M. J., S. I. Abdel-Khalik, S. M. Jeter and D. L. Sadowski (2005). "An experimental investigation of microchannel flow with internal pressure measurements." International Journal of Heat and Mass Transfer **48**(8): 1518-1533.

Krupa, K., M. Ashar Sultan, C. P. Fonte, M. I. Nunes, M. M. Dias, J. C. B. Lopes and R. J. Santos (2012). "Characterization of mixing in T-jets mixers." Chemical Engineering Journal **207**: 931-937.

Kundu, P. K. and I. M. Cohen (2008). Fluid mechanics, Academic Press.

Langtry, R. B., F. R. Menter, S. R. Likki, Y. B. Suzen, P. G. Huang and S. Volker (2006). "A correlation-based transition model using local variables - Part II: Test cases and industrial applications." Journal of Turbomachinery-Transactions of the Asme **128**(3): 423-434.

Lauterborn, W. (1972). "High-speed photography of laser-induced breakdown in liquids." Applied Physics Letters **21**(1): 27-29.

Lauterborn, W. (1979). Cavitation and Coherent Optics. Cavitation and Inhomogeneities in Underwater Acoustics, Springer-Verlag**:** 3-12.

Lauterborn, W. and H. Bolle (1975). "Experimental investigations of cavitation-bubble collapse in the neighbourhood of a solid boundary." Journal of Fluid Mechanics **72**(02): 391-399.

Lauterborn, W. and W. Hentschel (1985). "Cavitation bubble dynamics studied by high speed photography and holography: part one." Ultrasonics **23**(6): 260-268.

Lautz, J., G. Sankin, F. Yuan and P. Zhong (2010). "Displacement of

particles in microfluidics by laser-generated tandem bubbles." Applied Physics Letters **97**(18).

Leymarie, F. and M. D. Levine (1993). "Tracking deformable objects in the plane using an active contour model." Pattern Analysis and Machine Intelligence, IEEE Transactions on **15**(6): 617-634.

Li, H. and M. G. Olsen (2006a). "Examination of large-scale structures in turbulent microchannel flow." Experiments in Fluids **40**(5): 733-743.

Li, H. and M. G. Olsen (2006b). "MicroPIV measurements of turbulent flow in square microchannels with hydraulic diameters from 200 mu m to 640 mu m." International Journal of Heat and Fluid Flow **27**(1): 123-134.

Li, H., R. H. Ewoldt and M. G. Olsen (2005). "Turbulent and transitional velocity measurements in a rectangular microchannel using microscopic particle image velocimetry." Experimental Thermal and Fluid Science **29**(4): 435-446.

Li, S. and D. Billson (2011). EPSRC WIMRC Final Report, University of Warwick.

Li, S. C. (2000). Cavitation of hydraulic machinery. London, Imperial College Press.

Lim, K. Y., P. A. Quinto-Su, E. Klaseboer, B. C. Khoo, V. Venugopalan and C.-D. Ohl (2010). "Nonspherical laser-induced cavitation bubbles." Physical Review E **81**(1).

Lindau, O. and W. Lauterborn (2003). "Cinematographic observation of the collapse and rebound of a laser-produced cavitation bubble near a wall." Journal of Fluid Mechanics **479**: 327-348.

Majumdar, S. (1988). "ROLE OF UNDERRELAXATION IN MOMENTUM INTERPOLATION FOR CALCULATION OF FLOW

WITH NONSTAGGERED GRIDS." Numerical Heat Transfer **13**(1): 125-132.

Majumdar, Z. K., J. D. B. Sutin and R. M. Clegg (2005). "Microfabricated continuous-flow, turbulent, microsecond mixer." Review of Scientific Instruments **76**(12): 125103-125111.

Masca, S. I., I. R. Rodriguez-Mendieta, C. T. Friel, S. E. Radford and D. A. Smith (2006). "Detailed evaluation of the performance of microfluidic T mixers using fluorescence and ultraviolet resonance Raman spectroscopy." Review of Scientific Instruments **77**(5): 055105-055109.

Matsumoto, S., A. Yane, S. Nakashima, M. Hashida, M. Fujita, Y. Goto and S. Takahashi (2007). "A Rapid Flow Mixer with 11-μs Mixing Time Microfabricated by a Pulsed-Laser Ablation Technique: Observation of a Barrier-Limited Collapse in Cytochrome c Folding." Journal of the American Chemical Society **129**(13): 3840-3841.

Maynes, D. and A. R. Webb (2002). "Velocity profile characterization in sub-millimeter diameter tubes using molecular tagging velocimetry." (1): 3-15.

McNamara, W. B., Y. T. Didenko and K. S. Suslick (1999). "Sonoluminescence temperatures during multi-bubble cavitation." Nature **401**(6755): 772-775.

Meinhart, C. D., S. T. Wereley and J. G. Santiago (1999). "PIV measurements of a microchannel flow." (5): 414-419.

Menet, S., P. Saint-Marc and G. Medioni (1990). Active contour models: overview, implementation and applications. Systems, Man and Cybernetics, 1990. Conference Proceedings., IEEE International Conference on.

Menet, S., S. Marc and G. Medioni (1990). B-Snakes:implementation and

application to stereo. Proceedings DARPA.

Menter, F. R. (1994). "2-EQUATION EDDY-VISCOSITY TURBULENCE MODELS FOR ENGINEERING APPLICATIONS." Aiaa Journal **32**(8): 1598-1605.

Menter, F. R., R. B. Langtry, S. R. Likki, Y. B. Suzen, P. G. Huang and S. Volker (2006a). "A correlation-based transition model using local variables - Part I: Model formulation." Journal of Turbomachinery-Transactions of the Asme **128**(3): 413-422.

Menter, F. R., R. Langtry and S. Voelker (2006b). "Transition modelling for general purpose CFD codes." Flow Turbulence and Combustion **77**(1-4): 277-303.

Minkowycz, W. J., J. P. Abraham and E. M. Sparrow (2009). "Numerical simulation of laminar breakdown and subsequent intermittent and turbulent flow in parallel-plate channels: Effects of inlet velocity profile and turbulence intensity." International Journal of Heat and Mass Transfer **52**(17-18): 4040-4046.

Mishra, C. and Y. Peles (2006). "An experimental investigation of hydrodynamic cavitation in micro-Venturis." Physics of Fluids **18**(10).

Mohiuddin Mala, G. and D. Li (1999). "Flow characteristics of water in microtubes." International Journal of Heat and Fluid Flow **20**(2): 142-148.

Moin, P. and K. Mahesh (1998). "DIRECT NUMERICAL SIMULATION: A Tool in Turbulence Research." Annual Review of Fluid Mechanics **30**(1): 539-578.

Moskowitz, G. W. and R. L. Bowman (1966). "Multicapillary Mixer of Solutions." Science **153**(3734): 428-429.

Mukherjee, D. P. and S. T. Acton (2007). "Affine and projective active

contour models." Pattern Recognition **40**(3): 920-930.

Myers, J. K. and T. G. Oas (2002). "Mechanisms of fast protein folding." Annual Review of Biochemistry **71**: 783-815.

Natrajan, V. and K. Christensen (2010). "The impact of surface roughness on flow through a rectangular microchannel from the laminar to turbulent regimes." (1): 95-121.

Natrajan, V. K. and K. T. Christensen (2007). "Microscopic particle image velocimetry measurements of transition to turbulence in microscale capillaries." Experiments in Fluids **43**(1): 1-16.

Natrajan, V. K. and K. T. Christensen (2010). "The impact of surface roughness on flow through a rectangular microchannel from the laminar to turbulent regimes." Microfluidics and Nanofluidics **9**(1): 95-121.

Natrajan, V. K., E. Yamaguchi and K. T. Christensen (2007). "Statistical and structural similarities between micro- and macroscale wall turbulence." Microfluidics and Nanofluidics **3**(1): 89-100.

Nguyen, N. and Z. Wu (2005). "Micromixers - a review." Journal of Micromechanics and Microengineering **15**(2): R1-R16.

Nguyen, N.-T. (2012). Micromixers : fundamentals, design and fabrication. Oxford ; Waltham, MA, Elsevier/William Andrew.

Ohl, C.-D., M. Arora, R. Dijkink, V. Janve and D. Lohse (2006). "Surface cleaning from laser-induced cavitation bubbles." Applied Physics Letters **89**(7).

Pal, N. R. and S. K. Pal (1993). "A review on image segmentation techniques." Pattern Recognition **26**(9): 1277-1294.

Peng, X. F., G. P. Peterson and B. X. Wang (1994). "FRICTIONAL FLOW CHARACTERISTICS OF WATER FLOWING THROUGH

RECTANGULAR MICROCHANNELS." Experimental Heat Transfer **7**(4): 249-264.

Pham, D. L., C. Xu and J. L. Prince (2000). A Survey of Current Methods in Medical Image Segmentation. Annual Review of Biomedical Engineering. **2:** 315-338.

Philipp, A. and W. Lauterborn (1998). "Cavitation erosion by single laser-produced bubbles." Journal of Fluid Mechanics **361**: 75-116.

Plesset, M. S. and R. B. Chapman (1971). "Collapse of an initially spherical vapour cavity in the neighbourhood of a solid boundary." Journal of Fluid Mechanics **47**(02): 283-290.

Pope, S. B. (2000). Turbulent flows. Cambridge, Cambridge University Press.

Quinto-Su, P. A. and C.-D. Ohl (2009). "Interaction between two laser-induced cavitation bubbles in a quasi-two-dimensional geometry." Journal of Fluid Mechanics **633**.

Quinto-Su, P. A., H.-H. Lai, H. H. Yoon, C. E. Sims, N. L. Allbritton and V. Venugopalan (2008). "Examination of laser microbeam cell lysis in a PDMS microfluidic channel using time-resolved imaging." Lab on a Chip **8**(3).

Quinto-Su, P. A., K. Y. Lim and C.-D. Ohl (2009). "Cavitation bubble dynamics in microfluidic gaps of variable height." Physical Review E **80**(4).

Quinto-Su, P. A., V. Venugopalan and C. D. Ohl (2008). "Generation of laser-induced cavitation bubbles with a digital hologram." Optics Express **16**(23).

Rands, C., B. W. Webb and D. Maynes (2006). "Characterization of

transition to turbulence in microchannels." International Journal of Heat and Mass Transfer **49**(17–18): 2924-2930.

Ray, N., A. Ahmetovic, S. Das, K. Scott, A. Gerlich and P. Mendez (2010). Active contour (snake) methodology for minimally user-interactive visual tracking of high speed videos of free-flight metal transfer. Fabtech/AWS Welding and Metal Fabrication. Atlanta, Georgia United States.

Ray, N., S. T. Acton and K. Ley (2002). "Tracking leukocytes in vivo with shape and size constrained active contours." Ieee Transactions on Medical Imaging **21**(10).

Rayleight, L. (1917). "VIII. On the pressure developed in a liquid during the collapse of a spherical cavity." Philosophical Magazine Series 6 **34**(200): 94.

Regenfuss, P., R. M. Clegg, M. J. Fulwyler, F. J. Barrantes and T. M. Jovin (1985). "Mixing liquids in microseconds." Review of Scientific Instruments **56**(2): 283-290.

Rhie, C. M. and W. L. Chow (1983). "Numerical study of the turbulent flow past an airfoil with trailing edge separation." AIAA Journal **21**: 1525-1532.

Sagaut, P., S. Deck and M. Terracol (2006). Multiscale and multiresolution approaches in turbulence. London, Imperial College Press.

Santiago, J. G., S. T. Wereley, C. D. Meinhart, D. J. Beebe and R. J. Adrian (1998). "A particle image velocimetry system for microfluidics." Experiments in Fluids **V25**(4): 316-319.

Sharp, K. V. and R. J. Adrian (2004). "Transition from laminar to turbulent flow in liquid filled microtubes." Experiments in Fluids **36**(5): 741-747.

Shastry, M. C. R., S. D. Luck and H. Roder (1998). "A Continuous-Flow Capillary Mixing Method to Monitor Reactions on the Microsecond Time Scale." Biophysical journal **74**(5): 2714-2721.

Sinton, D. (2004). "Microscale flow visualization." Microfluidics and Nanofluidics **1**(1): 2-21.

Skoda, R., U. Iben, A. Morozov, M. Mihatsch, S. J. Schmidt and N. A. Adams (2011). Numerical simulation of collapse induced shock dynamics for the prediction of the geometry, pressure and temperature impact on the cavitation erosion in micro channels. WIMRC 3rd International Cavitation Forum 2011. University of Warwick.

Soleymani, A., E. Kolehmainen and I. Turunen (2008). "Numerical and experimental investigations of liquid mixing in T-type micromixers." Chemical Engineering Journal 135: S219-S228.

Sparrow, E. M., J. P. Abraham and W. J. Minkowycz (2009). "Flow separation in a diverging conical duct: Effect of Reynolds number and divergence angle." International Journal of Heat and Mass Transfer **52**(13-14): 3079-3083.

Steinke, M. E. and S. G. Kandlikar (2006). "Single-phase liquid friction factors in microchannels." International Journal of Thermal Sciences **45**(11): 1073-1083.

Sturman, R., J. M. Ottino and S. Wiggins (2006). The mathematical foundations of mixing : the linked twist map as a paradigm in applications : micro to macro, fluids to solids. Cambridge ; New York, Cambridge University Press.

Takahashi, S., S.-R. Yeh, T. K. Das, C.-K. Chan, D. S. Gottfried and D. L. Rousseau (1997). "Folding of cytochrome c initiated by submillisecond mixing." Nat Struct Mol Biol **4**(1): 44-50.

Taylor, G. I. (1921). "Diffusion by continuous movements." Proceedings of the London Mathematical Society **20**: pp. 196-211.

Tu, J., G. H. Yeoh and C. Liu (2008). Computational fluid dynamics : a practical approach. Amsterdam ; Boston, Butterworth-Heinemann.

Versteeg, H. K. and W. Malalasekera (2007). An introduction to computational fluid dynamics : the finite volume method. Harlow, Prentice Hall.

Vogel, A., J. Noack, K. Nahen, D. Theisen, S. Busch, U. Parlitz, D. X. Hammer, G. D. Noojin, B. A. Rockwell and R. Birngruber (1999). "Energy balance of optical breakdown in water at nanosecond to femtosecond time scales." Applied Physics B-Lasers and Optics **68**(2).

Vogel, A., W. Lauterborn and R. Timm (1989). "Optical and acoustic investigations of the dynamics of laser-produced cavitation bubbles near a solid boundary." Journal of Fluid Mechanics **206**: 299-338.

Weilin Q., Mohiuddin Mala G. and Dongqing L. (2000). "Pressure-driven water flows in trapezoidal silicon microchannels." International Journal of Heat and Mass Transfer **43**(3): 353-364.

Werner Lauterborn and Thomas, K. (2010). "Physics of bubble oscillations." Reports on Progress in Physics **73**(10): 106501.

White, F. M. (2008). Fluid mechanics. Boston [u.a.], McGraw-Hill Higher Education.

Wong, M. M. and Z. A. Schelly (1973). "CAVITATION AS ARTIFACT IN STOPPED FLOW EXPERIMENTS." Review of Scientific Instruments **44**(9).

Wu, T.-H., L. Gao, Y. Chen, K. Wei and P.-Y. Chiou (2008). "Pulsed laser triggered high speed microfluidic switch." Applied Physics Letters **93**(14): 144102-144102-144103.

Xu, C. and J. L. Prince (1998). "Generalized gradient vector flow external forces for active contours." Signal Processing **71**(2): 131-139.

Xu, C. and J. L. Prince (1998). "Snakes, shapes, and gradient vector flow." Image Processing, IEEE Transactions on **7**(3): 359-369.

Yarin, L. P., A. Mosyak and G. Hetsroni (2009). Fluid flow, heat transfer and boiling in micro-channels. Berlin, Springer.

Zuo, Z. (2008). Experimental and Numerical Study of Laser-induced Cavitaiton Bubbles on Warwick Cavitation Rig. Ph.D., University of Warwick.

Zwaan, E., S. Le Gac, K. Tsuji and C.-D. Ohl (2007). "Controlled cavitation in microfluidic systems." Physical Review Letters **98**(25).